Karlsruhe Institute of Technology

Lightning characteristics along radar-detected hail tracks

Master's Thesis of

Marie Lange

At the KIT Department of Physics
Institute of Meteorology and Climate Research

First examiner: Prof. Dr. Michael Kunz
Second examiner: Prof. Dr. Andreas Fink
Advisor: Dr. Jannick Fischer von zur Gathen

18. December 2024 – 17. December 2025

Abstract

This thesis investigates lightning characteristics along radar-detected potential hail tracks in Germany and neighboring regions for the period April to September, 2005-2023. Potential hail tracks were derived using radar data and the TRACE3D algorithm, and lightning strikes were assigned within a fixed spatial radius of 15 km and a temporal window of 15 min around each track timestep.

The analysis examines lightning activity throughout the lifecycles of potential hail tracks of different duration, variations in the occurrence of lightning throughout the years, and differences between clustered and non-clustered potential hail tracks. Additional perspectives include extreme precipitation intensity and pre-convective environmental conditions, based on convective parameters and aerosols.

The results demonstrate that lightning activity varies substantially throughout the lifetime of potential hail tracks and increases systematically with potential hail track duration. Longer potential hail tracks consistently exhibit higher lightning activity, indicating that these storms are intrinsically more electrically active, rather than simply accumulating more strikes over time. In contrast, extreme precipitation intensity shows little variation across track duration.

A pronounced decline in lightning activity along potential hail tracks is observed over the study period. This decrease persists after normalizing for interannual variability in track numbers, and is evident across the entire study domain. Conversely, extreme precipitation intensity shows a tendency towards intensification, suggesting that storm precipitation characteristics and lightning occurrence do not necessarily evolve in parallel.

Environmental parameters help to explain the observed temporal changes. Higher lightning intensity is associated with greater instability (greater Convective Available Potential Energy, lower Lifted Index), stronger updrafts and higher low-level relative humidity. Aerosol variables, particularly sulphate aerosol optical depth, show trends that are consistent with the observed decline in lightning, which suggests that changes in aerosol concentrations and the associated cloud microphysical processes may play a key role. Thermodynamic and kinematic parameters exhibit no comparable long-term temporal trend.

Zusammenfassung

In dieser Arbeit werden die Charakteristiken von Blitzen entlang von potentielle Hagelzugbahnen untersucht, die in Deutschland und benachbarten Regionen im Zeitraum von April bis September der Jahre 2005 bis 2023 mittels Radar erfasst wurden. Die potentiellen Hagelzugbahnen wurden mit dem TRACE3D-Algorithmus abgeleitet, und die Blitze innerhalb eines festen räumlichen Radius von 15 km und eines zeitlichen Fensters von 15 min um jeden Zeitschritt der Zugbahnen herum zugeordnet.
Die Arbeit untersucht die Blitzaktivität während des gesamten Lebenszyklus von hagelproduzierenden Gewittern unterschiedlicher Dauer, Schwankungen im Auftreten von Blitzen im Laufe der Jahre sowie Unterschiede zwischen gruppierten und nicht gruppierten hagelproduzierenden Gewittern. Weitere Perspektiven umfassen die extreme Niederschlagsintensität und präkonvektive Umgebungsbedingungen, die auf Konvektionsparametern und Aerosolen basieren.
Die Ergebnisse zeigen, dass die Blitzaktivität während der gesamten Lebensdauer der hagelproduzierenden Gewittern erheblich variiert und mit deren Dauer systematisch zunimmt. Längere hagelproduzierende Gewitter weisen durchweg eine höhere Blitzaktivität auf. Dies deutet darauf hin, dass diese Stürme von Natur aus elektrisch aktiver sind und nicht lediglich im Laufe der Zeit mehr Blitzeinschläge aufweisen. Im Gegensatz dazu zeigt die maximale Niederschlagsintensität nur geringe Schwankungen über die Dauer der Gewitter hinweg.
Im Untersuchungszeitraum ist ein deutlicher Rückgang der Blitzaktivität entlang der hagelproduzierenden Gewittern zu beobachten. Dieser Rückgang bleibt auch nach Normierung mit der jährlichen Variabilität der Gewitterhäufigkeit bestehen. Er ist im gesamten Untersuchungsgebiet erkennbar. Umgekehrt zeigt die extreme Niederschlagsintensität eine Tendenz zur Intensivierung, was darauf hindeutet, dass sich die Niederschlagseigenschaften von Gewittern und das Auftreten von Blitzen nicht unbedingt proportional ist.
Die Parameter der konvektiven Umgebungsbedingungen helfen dabei, die beobachteten zeitlichen Veränderungen zu erklären. Eine höhere Blitzintensität ist mit einer höheren Instabilität (höhere Convective Available Potential Energy, niedrigerer Lifted Index), stärkeren

Aufwinden und einer höheren relativen Luftfeuchtigkeit in den unteren Schichten verbunden. Die Konzentration von Aerosolen, insbesondere die optische Dicke von Sulfataerosolen, zeigen Trends, die mit dem beobachteten Rückgang der Blitzaktivität übereinstimmen. Dies deutet darauf hin, dass Veränderungen der Aerosolkonzentrationen und die damit verbundenen mikrophysikalischen Prozesse in Wolken eine wichtige Rolle spielen könnten. Thermodynamische und kinematische Parameter zeigen jedoch keinen vergleichbaren langfristigen zeitlichen Trend.

Preface

ChatGPT (`https://www.chatgpt.com`), Microsoft Copilot (`https://www.copilot.microsoft.com`), and DeepL ((`https://www.deepl.com`)) were used for translations and writing improvements.

Generated using Copernicus Atmosphere Monitoring Service information [2025] for the analysis of atmospheric aerosol data. Neither the European Commission nor ECMWF is responsible for any use that may be made of the Copernicus information or data it contains.

Contents

1. Introduction

Severe convective storms (SCS) are among the most spectacular yet hazardous weather phenomena, with hail and lightning being two of their most prominent characteristics. Both are intrinsically linked through microphysical processes of deep convection, where charge separation among liquid and ice particles enables lightning generation while simultaneously contributing to hail formation. Understanding this interplay is crucial for improving severe weather prediction, particularly in the context of a changing climate, where shifts in storm environments and aerosol concentrations may alter storm frequency and intensity. Despite extensive research on each phenomenon individually, their combined occurrence and the environmental factors influencing their interaction remain insufficiently explored.

Thunderstorms typically evolve through distinct phases (initiation, mature stage, and dissipation), each characterized by different levels of convective intensity (see section 2.1.3). These phases influence storm dynamics and microphysical processes, which in turn affect lightning occurrence. Wapler (2017) and Wilhelm (2022) have shown that the spatial extent of thunderstorms in Germany often follows a parabolic pattern over time, reflecting growth and decay processes.
Furthermore, Wapler (2017) investigated lightning activity during the lifecycle of hail tracks and identified two local maxima: one prior to hail onset and another during hail.
Such findings indicate that electrical activity is closely linked to the temporal evolution of convective systems.

Past studies have shown that lightning and hail activity depend on two factors: convective ingredients (Taszarek et al., 2020), which characterize the atmospheric state, and aerosols (Fan et al., 2025).

The first approach involves thermodynamic and kinematic parameters derived from numerical weather prediction models or atmospheric in-situ soundings. These enable the quantification of thunderstorm probability based on the underlying atmospheric conditions (Kunz, 2007). Several measures have been proposed for different severe thunderstorm

phenomena, such as large hail, severe wind gusts, and tornadoes (Taszarek et al., 2017). However, the limited temporal and spatial resolution of soundings constrains the analysis of convective parameters.
To address this, Taszarek et al. (2020) quantified a large number of convective parameters based on ERA5 reanalysis data by considering different atmospheric layers and processes, providing a more comprehensive approach.

The second approach considers aerosol-related parameters. Several studies have demonstrated an increase in cloud condensation nuclei (CCN) and cloud droplet numbers near anthropogenic sources, particularly over shipping lanes (Twomey, 1974; Radke and Hobbs, 1976; Radke et al., 1989). CCN and cloud droplets play a crucial role in the formation of hail and lightning (Fan et al., 2025; see chapter 2). For instance, the probability of lightning at a ship location compared to a site 2 or 25 km away is 15 or 66 times higher, respectively (Peterson, 2023).
Wright et al. (2025) reported a decrease in lightning occurrence over shipping lanes in the Indian Ocean and the South China Sea following the implementation of sulphur regulations in marine fuels in 2020. They also observed an enhancement in lightning strikes over these shipping lanes both before and after the regulation. The authors attribute the decrease to reduced sulphur emissions, as shipping traffic remained unchanged. To investigate this, they employed CAPE (Convective Available Potential Energy) and precipitation rates to construct various occurrence schemes based on their combinations, and found a decrease across almost all combinations.

Augenstein et al. (2024) reported a decrease in lightning density and in the number of days with at least five lightning strikes per grid box across most parts of France and Germany from 2001 to 2021. Furthermore, spatio-temporally intense lightning clusters were found to be smaller in spatial extent and more widely separated. The authors suggest that the North Atlantic Oscillation (NAO) teleconnection pattern may be a contributing factor for these changes.

This thesis seeks to offer further insights into the relationship between lightning and hail and to address open questions raised by previous studies. It aims to provide a combined perspective by analyzing lightning activity along radar-detected hail tracks and linking these patterns to environmental and aerosol conditions. A key aspect lies in its long-term approach, which enables the examination of trends in lightning activity over nearly two decades. These insights reveal how severe storm characteristics evolve under changing atmospheric and aerosol influences.

To this end, radar-detected hail tracks based on the TRACE3D algorithm (Handwerker, 2002; Schmidberger, 2018) and lightning data from EUCLID (European Cooperation for Lightning Detection) are analyzed to identify lightning characteristics along individual hail tracks in Germany and surrounding areas from 2005 to 2023. As radar-based hail estimation involves a certain degree of uncertainty, these tracks are referred to as potential hail tracks (PHTs) throughout this study. The investigation of environmental conditions prior to the onset of PHTs seeks to provide insights into the factors influencing lightning activity.

Based on this background, the following three hypotheses are formulated:

- Lightning activity varies during the lifecycle of a PHT and across different hail track durations.
- Lightning activity along PHT decreases over the period 2005–2023.
- These variations in lightning activity can be explained by convective and atmospheric aerosol parameters.

This thesis is organized as follows: Chapter 2 outlines the theoretical background of deep convection, hail, and lightning, and examines the influence of aerosols. Chapter 3 introduces the data sources, including radar-detected PHTs, lightning strikes, convective parameters, and variables describing atmospheric aerosols under the prevailing environmental conditions. Subsequently, the algorithms used to identify lightning strikes and assign environmental conditions along PHTs, as well as cluster PHTs, are described. Chapter 4 presents the temporal and spatial characteristics of lightning strikes along PHTs, followed by an analysis of pre-convective environmental conditions and their relationship to lightning intensity. Finally, chapter 5 summarizes and discusses the findings of this thesis and provides an outlook for future research.

2. Theoretical background and physical principles

This chapter presents the key meteorological concepts relevant to hailstorms and their electrical characteristics. It covers the physical processes of convection, lightning, and hail, and discusses radar-based hailstorm detection, the link between lightning activity and hail formation, and approaches to combining radar and lightning data in joint analyses.

2.1. Deep moist convection

This thesis focuses on severe thunderstorms that produce hail. For both lightning and hail formation, deep moist convection (DMC) is a prerequisite. In meteorology, convection refers to the vertical movement of air caused by differences in temperature and density, which is accompanied by an exchange of energy and enthalpy.
According to Johns and Doswell (1992), DMC requires three key factors: sufficient moisture in the boundary layer, conditional instability within the atmosphere, and a lifting mechanism to trigger convection. Convection initiation can be driven by either natural buoyancy (free) or external forcing mechanisms (forced) (Markowski and Richardson, 2010). Free convective initiation is a thermally direct circulation. When incoming solar radiation warms the Earth's surface, the adjacent air layer is heated as well. The resulting decrease in air density causes an air parcel to rise relative to the surrounding atmosphere. Buoyancy represents a vertical pressure gradient force arising from density differences within an atmospheric column, which is not fully counteracted by gravity (Markowski and Richardson, 2010). Forced convection, on the other hand, is triggered by external forces, resulting from effects such as flow deviations and resulting convergence zones around mountains, cross-circulation at fronts, or large-scale pressure gradients (Markowski and Richardson, 2010). The type of convection relevant here is that in which the lifting and the resulting cooling of the air parcel

leads to saturation, followed by condensation and cloud formation. When an air parcel rises dry adiabatically, it cools until it reaches the point of saturation. This altitude is referred to as the Lifting Condensation Level (LCL) (Markowski and Richardson, 2010). From that level onward, condensation occurs, releasing latent heat that increases the parcel's buoyancy and enables further ascent. Similarly, the Level of Free Convection (LFC) denotes the height at which the air parcel becomes warmer than its surrounding environment (Markowski and Richardson, 2010). Associated with the LFC is the Equilibrium Level (EL), the altitude at which the rising parcel attains the same temperature as its environment and becomes neutrally buoyant (Markowski and Richardson, 2010).

2.1.1. Atmospheric stability

To assess whether rising air parcels can continue to ascend and potentially form thunderstorms, the stability (or stratification) of the atmosphere is crucial. Key measures like the lapse rate and the (equivalent) potential temperature help describe this stratification and determine the likelihood of convective development. In general, the temperature and density of the troposphere decreases with height. Assuming an air parcel experiences no phase change (condensation of water vapor), no heat exchange with the environment, but has the same pressure as the environment, its cooling rate during ascent (due to expansion) and its warming rate during descent (due to compression) can be described by the dry adiabatic lapse rate, $\Gamma_d \simeq 9.8\,\mathrm{K\,km^{-1}}$.

$$\Gamma_d \equiv -\frac{dT}{dz} = \frac{g}{c_p}, \tag{2.1}$$

with g as the gravitational acceleration and c_p as the specific heat for a constant-pressure process. Starting from this context, one can derive via integration from the current pressure level p of the air parcel to an reference level p_0 (in general ground level of 1000 hPa) the potential temperature θ :

$$\theta = T \cdot \left(\frac{p_0}{p}\right)^{\frac{R_l}{c_p}}, \tag{2.2}$$

with R_l the gas constant for dry air. θ describes the temperature of an air parcel that undergoes adiabatic compression without phase changes from pressure level p to p_0 (Trapp, 2013). As the water vapor within air parcels plays an important role in meteorology in general, and in this thesis in particular, it must be taken into account. Once the air parcel

reaches the saturation point, the water vapor condenses and latent heat is released. The assumptions for a dry adiabatic process are therefore violated. Thus, similarly to the potential temperature θ, the equivalent potential temperature θ_e can be introduced from Bolton (1980) in Equation 2.3. It is defined as the temperature an air parcel would reach if all the water vapor it contains were to condense at constant pressure and the resulting latent heat were fully converted into sensible heat (Trapp, 2013). Therefore, the resulting equivalent potential temperature θ_e considers the complete latent heat of condensation of water vapor during ascent and subsequent dry adiabatic descent from level p to p_0 (here 1000 hPa).

$$\theta_e = T \cdot \left(\frac{1000}{p}\right)^{0.2854\left(1-0.28\cdot 10^{-3} r\right)} \exp\left[\left(\frac{3.376}{T_{\mathrm{LCL}}} - 0.00254\right) \cdot r \cdot \left(1 + 0.81 \cdot 10^{-3} \cdot r\right)\right], \quad (2.3)$$

with p as the pressure in hPa, r as the mixing ration in $\mathrm{g\,kg^{-1}}$, and the T_{LCL} as the temperature at LCL. When water vapor condenses during ascent, latent heat is released, causing a saturated air parcel to cool more slowly than a dry one. As a result, the temperature change during vertical motion depends on the air parcel's temperature and its moisture content, due to the temperature-dependent ability of air to hold water vapor as described by the Clausius-Clapeyron equation (IPCC, 2023a). This influences the amount of latent heat released during condensation. Therefore, the exact value of the moist adiabatic lapse rate, Γ_m, is closely tied to the water vapor content of the air. In general, the dry adiabatic lapse rate Γ_d is greater than the moist adiabatic lapse rate, which typically ranges between 5–9.8 $\mathrm{K\,km^{-1}}$.

Thermal stratification, represented by the environmental lapse rate $\gamma_e = -\frac{\partial T}{\partial z}$, is a key indicator of atmospheric stability. A distinction is made between three stability regimes: absolutely stable, absolutely unstable, and conditionally unstable atmospheres. The following conditions apply:

- $\gamma_e < \Gamma_m < \Gamma_d$ and $\frac{\partial \theta}{\partial z} > 0$: absolutely stable
- $\Gamma_m < \gamma_e < \Gamma_d$ and $\frac{\partial \theta}{\partial z} = 0$: conditionally unstable
- $\Gamma_m < \Gamma_d < \gamma_e$ and $\frac{\partial \theta}{\partial z} < 0$: absolutely unstable

In the middle case, the atmosphere is unstable with respect to saturated vertical motion, but remains stably stratified for unsaturated (dry) motion. These three regimes can be illustrated using a common thought experiment: a moist air parcel is displaced vertically from its

equilibrium position. In absolutely stable conditions, a moist adiabatically ascending air parcel cools more rapidly than the surrounding environment (since $\gamma_e < \Gamma_m$). As a result, it becomes colder and denser than its surroundings, sinks back, and warms more quickly than the environment as it descends, eventually returning to its original position. In contrast, under absolutely unstable conditions, the parcel cools more slowly than the environment (as $\gamma_e > \Gamma_d$), remains warmer than the surrounding air, and thus continues to rise. It becomes positively buoyant. Under conditional instability, the temperature change and buoyancy of an air parcel depends on its saturation. If an air parcel reaches saturation during its ascent, the atmosphere becomes unstable, whereas unsaturated air parcels experience stable conditions.
It should be noted that this assessment of atmospheric stability relies on simplified assumptions. For one, the air parcel is treated as a closed system, with no exchange of momentum, moisture, or heat with the surrounding environment. In reality, this is not the case. Entrainment, the mixing of environmental air into the parcel, plays a significant role. If the entrained air is cooler and drier than the parcel, it can inhibit the parcel's ascent by reducing its buoyancy. Additionally, the ascent of an air parcel typically induces compensating subsidence in the surrounding air, which can alter the environmental conditions and affect the stability analysis (Markowski and Richardson, 2010). Finally, the effects of hydrometeors on the parcel's buoyancy are usually neglected in this framework, even though they can have a notable impact (Markowski and Richardson, 2010). These assumptions are summarized under the term parcel theory.

2.1.2. Convective measures

The concepts of atmospheric stability and convective initiation form the basis for understanding and quantifying the potential for convective development. However, convectively favorable stratification only indicates the possibility of convection. Actual initiation requires a triggering mechanism, that is as lifting mechanism. To evaluate the convective potential more precisely, including the amount of energy available for vertical motion and the strength of possible inhibiting layers, various diagnostic parameters have been introduced based on parcel theory. The selection here provides a short overview of the conditions in the atmosphere.

The convective potential available energy (CAPE) can be expressed as the vertical integral over height z of the buoyancy B from the LFC to EL:

$$B = \frac{dw}{dt} \ , \tag{2.4}$$

$$CAPE = \int_{LFC}^{EL} B \, dz \approx g \cdot \int_{LFC}^{EL} \frac{T_{vp} - T_{ve}}{T_{ve}} \, dz \ . \tag{2.5}$$

B can be expressed in terms of the difference between the virtual temperature of the air parcel T_{vp} and that of the surrounding environment T_{ve}. The virtual temperature T_v is defined as the temperature that dry air would need to have to match the density of moist air at the same pressure. Since water vapor is less dense than dry air, increasing moisture content leads to a higher virtual temperature. When an air parcel rises from the LFC to EL, it experiences positive buoyancy. As the pressure decreases with height, the parcel expands during ascent, performing work on its volume and reducing its internal energy, in accordance with the first law of thermodynamics. This work can, in theory, be converted into kinetic energy, which is why CAPE is often used as an indicator of potential updraft strength. Multiplying the vertical velocity $\frac{dz}{dt}$ on both sides of Equation 2.4 and integrating over the ascent from LFC to EL yields (Markowski and Richardson, 2010):

$$w \cdot \frac{dw}{dt} = B \cdot \frac{dz}{dt} \tag{2.6}$$

$$\Leftrightarrow \frac{d}{dt}\left(\frac{w^2}{2}\right) = B \cdot \frac{dz}{dt} \tag{2.7}$$

$$\Leftrightarrow \int_{LFC}^{EL} dw^2 = 2 \int_{LFC}^{EL} B \, dz \tag{2.8}$$

$$\Leftrightarrow \underbrace{w_{EL}^2 - w_{LFC}^2}_{w_{max}^2} = 2 \underbrace{\int_{LFC}^{EL} B \, dz}_{CAPE} \tag{2.9}$$

$$\Leftrightarrow w_{max}^2 = \sqrt{2 \cdot CAPE} \ . \tag{2.10}$$

Assuming $w_{LFC} = 0$, complete conversion of buoyant energy into vertical motion, no energy losses, and that the maximum vertical velocity w_{max} is reached at EL ($w_{max} = w_{EL}$).
In reality, not all of the available potential energy is converted into kinetic energy, as parts are dissipated through entrainment and other processes. Therefore, the evaluation of convective parameters is based on parcel theory (see subsection 2.1.1). Moreover, CAPE represents an upper limit for the kinetic energy and vertical velocity that a rising parcel

can theoretically reach. High CAPE values represent high possible updraft wind speeds and high potential for deep convection. (American Meteorological Society, 2024)
In addition to the potential of convective initiation there are also hindering factors for the free ascent, expressed by the convective inhibition (CIN). It quantifies the amount of energy required to lift an air parcel from the surface to its LFC against the stratification in the lower atmosphere (Markowski and Richardson, 2010). The calculation is done analogously to that of CAPE (see Equation 2.5 from Markowski and Richardson (2010)).

$$CIN = \int_{sfc}^{LFC} B\,dz \approx g \cdot \int_{sfc}^{LFC} \frac{T_{vp} - T_{ve}}{T_{ve}}\,dz \ . \tag{2.11}$$

The main difference is the integration from the surface to the LFC. Thus, the promoting and restriction characteristics of each measure become apparent. Similarly to the maximum vertical updraft velocity w_{max}, a threshold vertical velocity w_{CIN} can be defined as the minimum speed required to overcome the CIN barrier (Markowski and Richardson, 2010):

$$w_{CIN} = \sqrt{2 \cdot CIN} \ . \tag{2.12}$$

Deep convection requires not only high CAPE values but also sufficiently low CIN to overcome inhibition. Variations in lapse rates can significantly influence both CAPE and CIN (Markowski and Richardson, 2010). However, even with constant lapse rates, substantial changes in low-level moisture can produce similar effects. In general, large-scale ascent tends to reduce CIN, thereby increasing the likelihood of convective initiation.
In conclusion, Figure 2.1 illustrates the concepts discussed above. It shows a thermodynamic diagram (skew T - log p) based on a representative atmospheric sounding. The black line indicates the observed temperature profile from the surface up to the EL. The LFC is identified where the temperature profile intersects the moist adiabat (dashed orange line), marking the point of saturation. The equilibrium level (EL) is reached where these two lines intersect again higher in the troposphere, indicating the end of positive buoyancy. Prior to saturation, the air parcel follows a dry adiabat (orange line) up to the LCL. The differing lapse rates under dry and moist conditions are clearly visible by comparing the respective adiabats. Additionally, the diagram highlights areas of temperature difference between the parcel and the environment, shaded to represent CAPE and CIN across the relevant vertical layers.

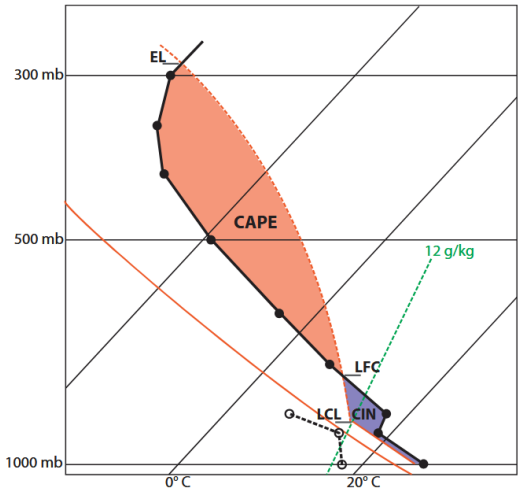

Figure 2.1: Exemplary thermodynamic diagram (skew T - log p) showing a sounding (black line). CAPE is represented by the positive area (orange) between the LFC and the EL, while CIN corresponds to the negative area (blue) between the surface and the LFC. The solid orange line is a dry adiabat, the dashed orange line is a relevant moist adiabat. Shown in Trapp (2013).

As shown in Equation 2.13, the Lifted Index (LI) represents the temperature difference between an adiabatically lifted air parcel and its surrounding environment at a pressure level of 500 hPa:

$$LI = T_{500hPa} - T_{parcel} \ . \tag{2.13}$$

The LI therefore indicates how rapidly an air parcel cools relative to its environment. As discussed in subsection 2.1.1, thunderstorms develop under unstable conditions, when the air parcel cools less than the surrounding air and continues to rise to higher altitudes. Consequently, negative LI values are associated with conditions favorable for thunderstorm development (Galway, 1956).
One other variable that plays a decisive role in the development of deep moist convective systems is vertical wind shear S. It describes the change of the horizontal wind component v_h with height z:

$$\vec{S} = \frac{\partial \vec{v_h}}{\partial z} \ . \tag{2.14}$$

Often the so called $0 - 6$ km bulk wind shear, the difference of the wind vector in 0 km and 6 km height, is used as measure for the shear. In general, vertical wind shear (S) supports storm organization and longevity. However, excessively strong shear can have the opposite effect by enhancing entrainment and disrupting updrafts.

Since the development of DMC depends on multiple factors, using a combination of convective parameters is a plausible approach. One example is *wmaxshear*, which combines the maximum vertical velocity and wind shear, which are both important ingredients for the development of DMC (see Equation 2.15).

$$WMAXSHEAR = w_{max} \cdot S = \sqrt{2 \cdot CAPE} \cdot S \ . \tag{2.15}$$

Taszarek et al. (2017) have shown, that *wmaxshear* is very well suited for distinguishing between severe and non-severe thunderstorms.
Another parameter related to shear to describe convective conditions is the storm-relative helicity (SRH). Helicity is the scalar product of the velocity and vorticity and describes therefore the alignment of the fluid motion to the vorticity of the fluid (Markowski and Richardson, 2010). For the development of the rotation of a storm, only horizontal wind components relative to the storm are relevant. Therefore the SRH is (Pucik et al., 2021):

$$SRH = -\int_0^h \hat{k} \cdot (\vec{v} - \vec{v}_{storm}) \times \frac{d\vec{v}}{dz} \, dz \ , \tag{2.16}$$

with $(\vec{v} - \vec{v}_{storm})$ as the storm-relative wind, and $\hat{k}$ as the unit vector in z-direction. The integration is done usually over the lowest 3 km, as this is the region of the inflow of the storm. SRH values greater than 150 $m^2\ s^{-2}$ indicate high probabilities for supercells. When supercells split and two independent cells develop, one moves to the left (left mover, LM) relative to the direction of the mean wind shear, the other to the right (right mover, RM) (Markowski and Richardson, 2010).

Precipitable water *PRCP_WATER* refers to the total amount of water vapor contained within a vertical atmospheric column of unit cross-sectional area, typically expressed as the height of liquid water if all vapor were condensed (American Meteorological Society, 2025). When considering the entire troposphere, this column extends from the Earth's surface to the top of troposphere. *PRCP_WATER* in a layer bounded by two pressure levels is calculated using the mixing ratio at each pressure level $r(p)$, accounting for water density ρ_w (see Equation 2.17).

$$PRCP\_WATER = \frac{1}{g \cdot \rho_w} \int_{p_1}^{p_2} r \ dp \ . \tag{2.17}$$

Rainfall amounts during storms often exceed the *PRCP_WATER* integrated over the whole troposphere because convergence transports additional moisture from surrounding areas.

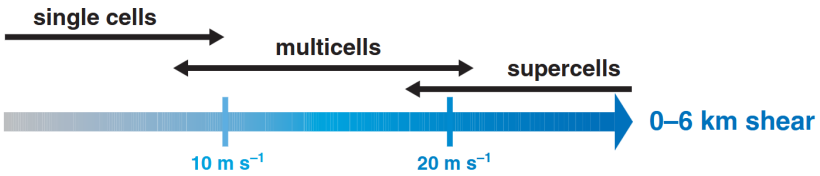

Figure 2.2: Occurring storm types depending on 0 – 6 km shear. Shown in Markowski and Richardson (2010).

Nevertheless, there is generally a positive correlation between precipitation in storms and the precipitable water content of the associated air masses. (American Meteorological Society, 2025)

As thunderstorms do not originate from a single air parcel, no unique value can be assigned to the convective parameters. It is therefore essential to specify which air parcel is used for the calculations. In the following analysis, three options are considered: the surface-based (SB), mixed-layer (ML), and most unstable (MU) air parcel, allowing for different initial conditions to be taken into account. The SB parcel is defined as the air parcel initialized at the surface (Czernecki et al., 2025). The ML parcel is obtained by mixing properties within the layer from the surface to 500 m above ground level. The MU parcel corresponds to the parcel with the highest θ_e within the layer extending from the surface to 3 km above ground level (Czernecki et al., 2025).

2.1.3. Convective cells and their organization

So far, the focus has been on the conditions necessary for convection to develop, as well as the parameters that influence its initiation. Once triggered, convection can organize into different types of convective system, ranging from isolated, short-lived single-cells to highly structured systems, such as multicells or supercells, depending on the surrounding atmospheric environment. Unless otherwise stated, the following section is based on Trapp (2013) and Markowski and Richardson (2010).

Figure 2.2 illustrates the spectrum of convective systems as a function of the 0 – 6 km shear (see subsection 2.1.2). The influence of shear on storm longevity becomes evident. Supercells typically form in environments with strong vertical wind shear, whereas single-cell storms develop under weak shear conditions. The overlap between different storm types can be attributed to additional factors, such as the vertical distribution of moisture and buoyancy.

The basic structure of a convective cell is defined by the co-existence of updrafts and downdrafts, which are localized vertical air motions that drive the storm's evolution. These currents are a key element of convection, and their development is influenced by buoyancy, and in more organized systems, by vertical pressure gradients.
The updraft corresponds to the theoretical concept of rising air parcels discussed in the previous sections. In contrast, downdrafts can develop for several reasons. One common cause is precipitation loading. As hydrometeors grow within the updraft, their increasing weight eventually exceeds the upward force, causing them to fall. This descent initiates a precipitation-driven downdraft, further enhanced by drag and evaporative cooling. It is worth noting that large frozen hydrometeors, such as graupel and hail, are more efficient than their liquid counterparts, not only because of the larger drag, but also because of cooling by melting or sublimation. On the other hand, dynamically driven downdrafts can develop as a direct response to the updraft. They can arise from the induced vertical pressure disturbances and induce negative vertical velocities.
As soon as the downdraft reaches the surface, it spreads out horizontally, referred to as the outflow. The outflow's leading edge marks a boundary with ascent ahead and subsidence behind, typically bringing gusty winds near the surface. It is therefore also called the gust front.

Single-cells are deep moist convective systems that consist of only one updraft and one downdraft. In general, these systems are short-living systems with a lifetime of about 30-60 min. This time can be estimated by adding together the time it takes for an air parcel to rise from the surface to the EL, based on the mean updraft velocity, and the time it takes for the resulting precipitation to descend to the surface. Based on this, the life cycle of a single-cell thunderstorm can be divided into three distinct stages: the towering cumulus stage, the mature stage, and the dissipating stage (see Figure 2.3). During the initial stage, only an updraft is present, leading to cloud formation and the vertical growth of the cumulus cloud. The mature stage begins once precipitation particles become large enough to fall through the updraft. This stage is also characterized by the development of an anvil cloud. As precipitation-induced downdrafts intensify and evaporation of hydrometeors occurs, buoyancy within the updraft decreases. The final dissipating stage begins when the downdraft dominates the system, effectively cutting off the updraft and preventing further convective development.

Conversely, multi-cells continuously generate new updrafts along the gust front, where forced lifting can raise air parcels to the LFC. They are composed of short-lived individual cells in different stages (see Figure 2.4), but the repeated initiation of new ones enables

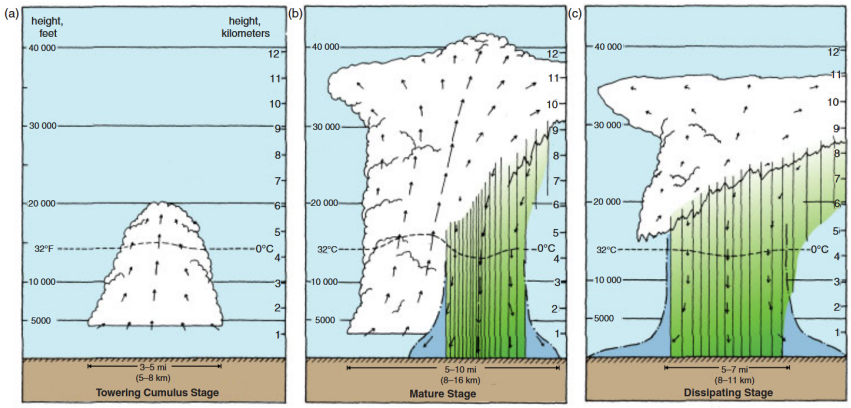

Figure 2.3: Three stages of an convective single-cell. Shown in Markowski and Richardson (2010).

the overall system to persist for several hours. In intense cases, such systems can produce widespread damaging winds and large hail. The preferred flank of the storm for the development of new cells is where the strongest lift occurs at the gust front downshear. At this position, the vorticity from the cold pool and of the environment have a different rotation direction, leading to increased ascent in combination. The moderate vertical wind shear leads to the spatial separation of up- and downdraft, which helps to prevent the cut-off of the cell complex from the inflow of warm and moist air. The single-cells move with the same velocity as the mean wind. However, the ongoing formation of new cells on a preferred flank causes the system's overall motion to differ from the mean wind, often moving at a different speed and direction, either faster or slower than the average flow.

Supercells are the least common form of convection, but at the same time related to the most severe weather, such as large hail (Blair et al., 2017), heavy rainfall, severe wind gusts, and strong tornadoes (Fischer et al., 2024). As mentioned above, the related strong vertical wind shear leads to longevity with typical lifetimes of about $3 - 8$ hours.
These convective systems consist of isolated cells featuring a rotating updraft region with strong vertical velocities, known as mesocyclones with a typical diameter of about $3 - 10$ km. Vertical pressure gradients can form dynamically through interactions between the updraft and the vertical wind shear. Together with mesocyclone-related processes, these gradients can significantly enhance the strength of the updraft. This distinguishes supercells from ordinary convective cells, which rely primarily on buoyant forces. While supercell environments typically feature moderate to high CAPE values (e.g., $>1000\,\mathrm{J\,kg^{-1}}$), extremely large CAPE is not a prerequisite for their development. As in other convective storms, precipitation in supercells forms within rising air and is transported to upper levels of the storm. Strong storm-relative winds at mid and upper levels help remove these hydrometeors

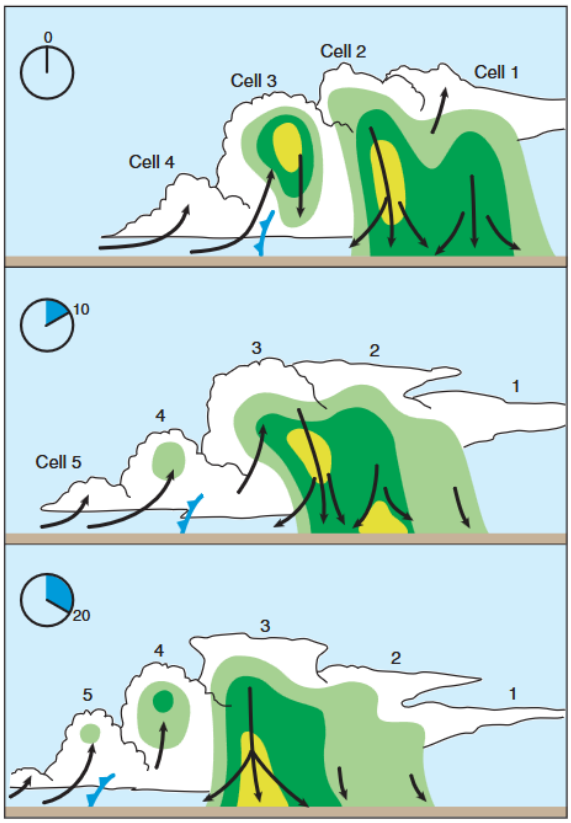

Figure 2.4: Temporal evolution of a multi-cell. Shown in Markowski and Richardson, 2010.

from the updraft, causing them to fall outside of it rather than through it (see Figure 2.5). As a result, the updraft region appears as an area of weak radar reflectivity. The descending precipitation contributes to the development of downdrafts, especially ahead and behind the updraft. These are referred to as the forward-flank downdraft (FFD) and rear-flank downdraft (RFD), both of which are intensified by the entrainment of cool, dry mid-level air that promotes evaporation and sublimation. Furthermore, the development of gust fronts at the surface is observed once more.

Although supercells do not exhibit new cell formation along a flank, as seen in multi-cell systems, their propagation still deviates from the mean wind. Depending on the sense of storm rotation (cyclonic or anticyclonic), their motion includes a right- or leftward component relative to the mean wind shear. Vertical pressure gradient forces due to vertical pressure perturbations ans therefore storm rotation result in right-moving (RM) and left-moving (LM) individual storms (see also subsection 2.1.2) (Trapp, 2013). Therefore, the rotation of the updraft and the cell propagation are linked to each other (Markowski and Richardson, 2010).

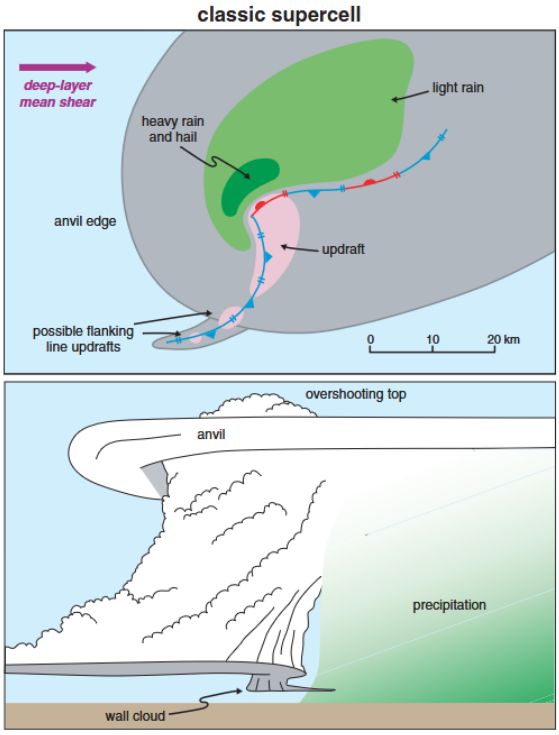

Figure 2.5: Schematic representation of a classic supercell, with the top panel illustrating the low-level radar structure in horizontal cross section and the bottom panel showing the visual appearance from a southern observer's perspective. Shown in Markowski and Richardson, 2010.

Mesoscale convective systems (MCS) form when multiple single cells merge into a continuous precipitation area spanning at least 100 km, or develop along or ahead of a synoptic-scale cold front or trough (Trapp, 2013). At this scale, the Coriolis force becomes significant (Markowski and Richardson, 2010). The continuous nature of the precipitation differentiates MCSs from clusters or lines of discrete cells. Furthermore, MCSs generally have a much longer lifetime than the roughly one-hour duration typical of individual cumulonimbus clouds within the system. Like multicell storms, MCSs comprise multiple individual cells at varying stages of development.

A specific type of MCS is the squall line, which consists of thunderstorm cells arranged in a linear pattern (Trapp, 2013). Typically, a broader area of stratiform precipitation follows the convective precipitation within a squall line, although convective precipitation can also occur in separate regions. According to Houze (1993), stratiform precipitation develops due to large-scale, weak upward vertical motions compared to the fall speeds of ice crystals and snow.

2.2. Hail

Hail is defined as falling ice-phase hydrometeors with a diameter of at least 5 mm (Allen et al., 2020). Smaller ice spheres are referred to as graupel. Hailstones can take on various shapes, including spherical, conical, or irregular forms (Allen et al., 2020).

2.2.1. Formation

Hail formation begins with a process known as nucleation. In the atmosphere, heterogeneous nucleation is the more common mechanism, although homogeneous nucleation can occur under extreme conditions. In both cases, the air must be supersaturated with respect to ice. Homogeneous nucleation refers to the spontaneous freezing of pure supercooled water droplets at temperatures around −40 °C and less, without the presence of a solid surface or aerosol (Lamb and Verlinde, 2011). At this temperature, the thermal energy of the water molecules is low enough for them to arrange into the crystalline lattice of ice without needing a nucleating surface (Lamb and Verlinde, 2011).
For heterogeneous freezing specific aerosols, referred to as ice nucleating particles (INPs) serve as nucleation germs. INPs are in usually insoluble to water (Lamb and Verlinde, 2011) and include natural aerosols such as pollen, mineral dust, sea salt, or bacteria and anthropogenic aerosols such as soot or sulfate. On the one hand, water vapor can deposit on solid, hydrophilic aerosols. On the other hand, aerosols can also be soluble in water. Due to the reaction of water vapor and those aerosols the saturation vapor pressure is reduced and therefore less oversaturation is necessary (Lamb and Verlinde, 2011). Thus, the occurring temperatures do not have to be as low as for homogeneous freezing (see Figure 2.6). Usually, soluble aerosols serve as cloud condensation nuclei (CCN) (Lamb and Verlinde, 2011).

In general, nucleation processes are faster the greater the surface area of an aerosol, as more water vapor can be included (Lamb and Verlinde, 2011).
Once initial ice particles are formed, they grow through a process called riming, in which supercooled water droplets collide with and freeze onto the ice particle (Lamb and Verlinde, 2011).
To form graupel and hailstones, these particles must remain in a growth-favorable environment for an extended period. Strong updrafts in convective systems enable this by keeping the particles suspended in regions of supercooled water (Lamb and Verlinde, 2011). For

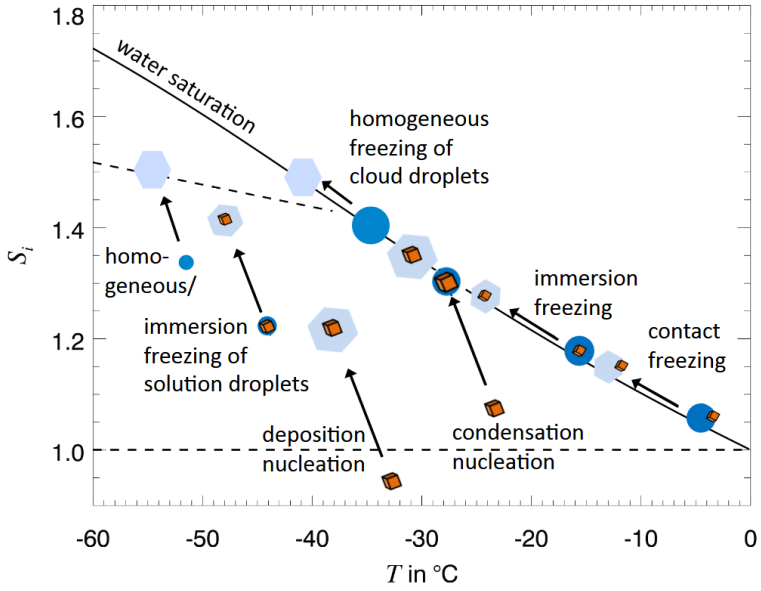

Figure 2.6: Schematic depiction of the different nucleation processes. From Hoose and Möhler, 2012.

this reason, hail is typically not associated with short-lived single-cell storms, but rather with multi-cell and supercell systems. In multi-cell storms, it is possible for hailstones to be transported between cells, extending their time in favorable growth conditions and allowing them to reach larger sizes. As the ice particle becomes larger, it starts to descend relative to the surrounding cloud droplets. During its descent, the particle continues to collect supercooled water and cloud droplets, increasing in both size and fall velocity due to its growing surface area. However, if the ice particles enter regions where the temperature exceeds 0 °C, melting begin. Consequently, smaller hailstones and graupel often vanish before reaching the ground, whereas larger hailstones can survive the descent. Due to the high kinetic energy of falling hailstones, hail poses a threat to humans, animals, crops and property. It can cause serious injuries, damage infrastructure and destroy vegetation, resulting in substantial economic losses. Munich Re (2025) estimates that the total insured damage caused by severe thunderstorms between 1980 and 2024 amounts to approximately US$1,000 billion. Notably, the report states that in 2024, the damage caused by regional thunderstorms in the U.S. was comparable to that of the year's costliest natural disaster, Hurricane Helene (Munich Re, 2025).

2.2.2. Radar detection for characterizing hailstorms

Since the analysis in this thesis is based on PHT identified in Radar (RAdio Detection and Ranging) data, the basics of weather Radar are briefly explained below.
Weather Radars emit radio waves into the atmosphere, which are scattered, reflected, and absorbed by hydrometeors along their path. A portion of the backscattered energy returns to the Radar system. From the time delay between the transmitted and received signal, the distance to the scatterer can be determined. Additionally, the intensity of the returned signal can be used to infer the size and type of the scattering particle. Radar systems are therefore widely used in meteorology, especially for weather observation and forecasting. The Radar equation (see Equation 2.18) describes the received power P_r, which depends on several system-specific parameters, such as transmitted power P_t, antenna gain G, beamwidth θ_b, pulse duration τ, and wavelength λ, as well as the speed of light c, the distance to the target r, and the dielectric properties of the target medium (summarized in K) (Trapp, 2013):

$$P_r = \left[\frac{\pi^3 \cdot P_t \cdot G^2 \cdot \theta_b^2 \cdot c \cdot \tau \cdot |K|^2}{1024 \cdot \ln(2) \cdot \lambda^2} \right] \frac{Z}{r^2} \ . \tag{2.18}$$

Here, the radar reflectivity factor Z represents the total backscatter cross-section per unit volume and is defined as:

$$Z = \frac{1}{V} \sum_{i=1}^{n} D_i^6 \tag{2.19}$$

where V is the sampled volume and D_i are the diameters of the n considered (spherical) hydrometeors (Trapp, 2013). The unit of Z is $\mathrm{mm}^6\,\mathrm{m}^{-3}$, but it is commonly expressed in logarithmic form as reflectivity in decibels: $\mathrm{dBZ} = 10 \cdot \log_{10}(Z)$. Generally, larger hydrometeors result in higher reflectivity values. According to Mason (1971), a threshold of 55 dBZ is often used to distinguish rain from hail. Although the distinction is not always clear-cut, this value remains a common benchmark in several studies. However, other quantities are also used, such as Maximum Estimated Size of Hail (MESH) or Probability Of Severe Hail (POSH) from Witt et al. (1998) (Kunz and Kugel, 2015; Murillo et al., 2021; Schmid et al., 2025).

2.2.3. Effect of climate change on hailstorms

Understanding hail in the context of climate change is relevant, as even subtle changes in atmospheric conditions can affect the frequency, intensity, and impact of hailstorms. In a warming climate, the Clausius–Clapeyron relation suggests an increase in moisture content, particularly in the lower troposphere. As described in section 2.1, an increase in low-level moisture generally results in more favorable conditions for DMC, leading to enhanced CAPE, stronger updrafts, and thus the potential for larger hailstones. Consequently, both the likelihood and severity of hailstorms may increase (Rädler et al., 2019; Battaglioli et al., 2023) .
However, warming mainly affects the lower layers leading to increase instability, increasing CIN and potentially suppressing convective development. Additionally, a warmer atmosphere raises the melting level height (MLH) (see Figure 2.7), resulting in different effects depending on hailstone size: Small hailstones are more likely to melt completely before reaching the ground, while larger hailstones, due to faster fall speeds and longer residence times in growth regions, are less affected by melting and may still reach the surface. (Allen, 2018; Mahoney, 2020)
Moreover, changes in vertical wind shear are expected, possibly showing a decreasing trend, though the magnitude and implications remain uncertain (Brooks, 2013). Nevertheless, the projected increase in convective available potential energy is expected to outweigh potential reductions in shear.
In summary, while the overall frequency of hail events may decrease, those that do occur are likely to be more intense and damaging. (Raupach et al., 2021)

The Intergovernmental Panel on Climate Change (IPCC, IPCC, 2023b) states that the confidence in projections of future changes in hail occurrence is low, for example due to low model resolution and inadequate parameterization. However, this does not mean that climate change will have no impact. Climate models generally indicate environmental changes conducive to more frequent and intense hail-producing thunderstorms, although there remains low confidence in the magnitude and regional details of these projected increases. (IPCC, 2023b)

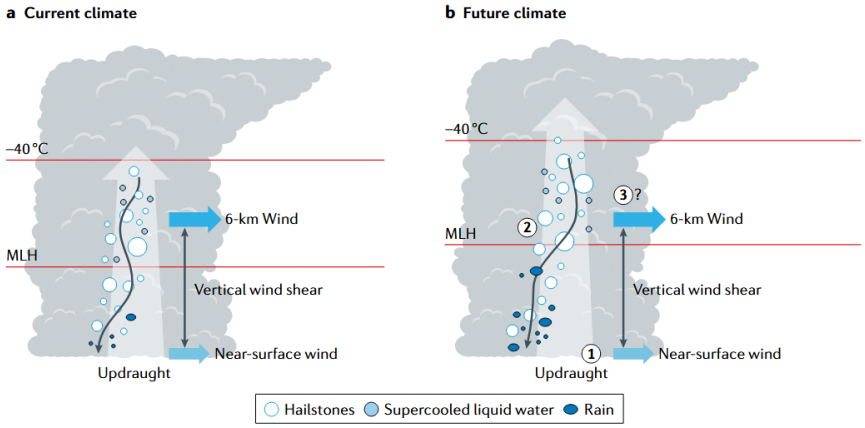

Figure 2.7: Projected differences in atmospheric conditions relevant to hail formation between present-day (panel a) and future (panel b) climate scenarios. With melting level height (MLH). From Raupach et al. (2021).

2.3. Lightning

Lightning is defined as a transient, high-current electric discharge in the atmosphere, with path lengths that can span several kilometers. It occurs either within a cloud, between clouds, or between a cloud and the ground, as a result of charge separation in cumulonimbus clouds, also known as thunderclouds. (American Meteorological Society, 2022)
Lightning is a defining feature of thunderstorms, with thunder being a direct result of the heating of the air due to charge separation (Lamb and Verlinde, 2011). Cumulonimbus clouds are the main source of lightning. However, volcanic eruptions, sandstorms and nuclear explosions can also lead to electrical discharges resulting in lightning (Rakov, 2021).

2.3.1. Thunderstorm electrification and charge separation

The electric chargers of a thunderstorm are mainly placed on liquid and frozen hydrometeors with some free ions (Krehbiel, 1986). The exact distribution changes rapidly over space and time. But in general, an idealized thundercloud can be divided in three parts:
Positive at the top (anvil), negative in the middle, and weak positive at the bottom (see Figure 2.8). In most thunderstorms, the main negative charge center is located in the mixed-phase region, typically between −10 and −25 °C, where graupel-ice collisions most efficiently generate negative charge (Krehbiel, 1986). However, the exact altitude and structure depend on storm type, stage of development, and environmental conditions. Unless otherwise stated, the following section is based on Lamb and Verlinde (2011) and Rakov, 2021.

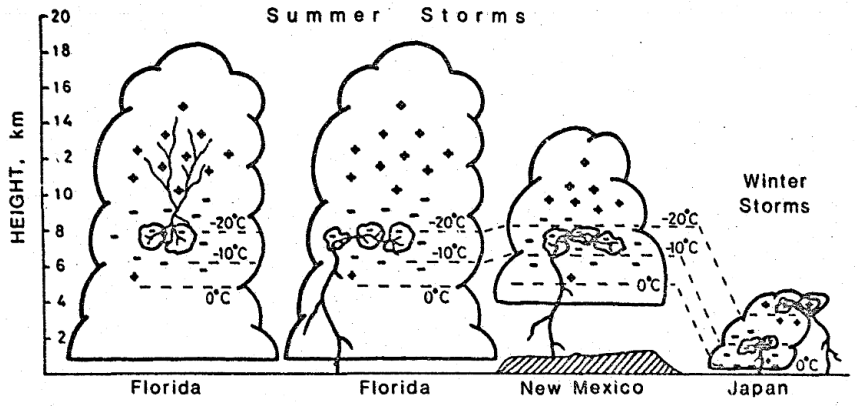

Figure 2.8: Schematic depiction of vertical thunderstorm structure and charge source regions in summer storms over Florida and New Mexico, and in winter storms over Japan. From Krehbiel (1986).

The theory behind the thunderstorm electrification is not yet fully understood and therefore there exist several explanations. The development of electric charge within thunderstorms requires two essential processes:
First, a microscopic interaction that separates electric charges on hydrometeors; and second, a vertical motion differences that distribute and separate these charged particles throughout the cloud system.
Particularly during the early phases of cloud electrification the graupel-ice mechanism is dominating. Thereby the electric charge separation in clouds arises from collisions between falling graupel particles and smaller ice crystals in the presence of supercooled water droplets. For charge exchange to occur, particles must collide and rebound, rather than coalesce. Laboratory experiments show that the direction of charge transfer depends on temperature: below a certain threshold (the reversal temperature, typically between -10 and $-20\,^{\circ}\mathrm{C}$), graupel becomes negatively charged; above it, positively charged. Gravity causes a vertical separation of charges, contributing to the typical charge structure observed in thunderclouds, including the development of a lower positive charge region.
Another possible mechanism is the convective charging. The charged particles are transported upward by strong updrafts within a pre-existing electric field. Initially, ions are generated by cosmic radiation and later enhanced by corona discharges near sharp objects. These ions attach to aerosols and cloud particles, which are then lifted through the cloud base into higher altitudes. This results in a positive charge buildup inside the cloud, which in turn attracts negative ions from the surrounding air, especially near the cloud edges, forming a negative screening layer. This redistribution enhances the internal electric field and can further increase ion production, making the process self-reinforcing. Although the

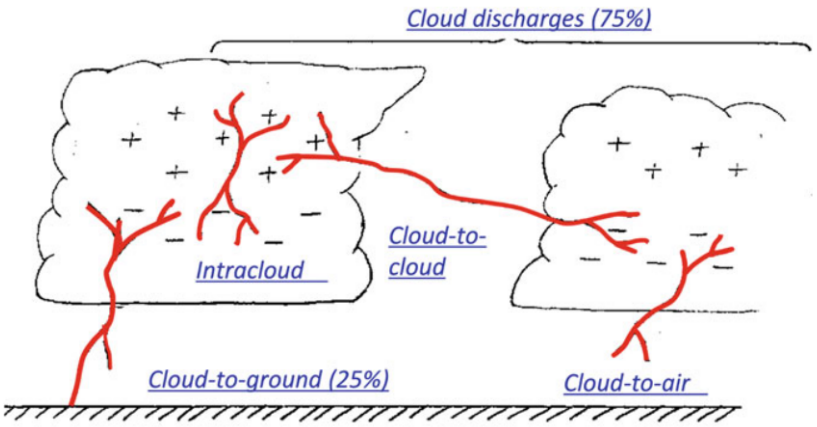

Figure 2.9: General classification of lightning discharges from cumulonimbus (thunderstorm clouds). From Rakov (2021).

available space charge may be limited, convection clearly plays a major role in moving and separating charge within storms.

It is important to note that this theoretical concept of thunderstorm electrification and charge separation, and thus the fundamental basis of lightning formation, is closely linked to the presence of ice particles. This relationship motivates the joint analysis of lightning activity and radar-detected PHTs in this thesis.

2.3.2. Discharge events

Unless otherwise stated, the following section is based on Lamb and Verlinde (2011), Rakov (2021) and American Meteorological Society (2022)) The overall discharge of electrically charged hydrometeors is commonly referred to as a lightning flash or bolt. When such a discharge reaches the ground, it is specifically termed a lightning strike. Discharges between cloud and ground are known as cloud-to-ground (CG) lightning. Only about 25 % of global lightning activity involves the ground; the remaining 75 % consists of intra-cloud, inter-cloud (also cloud-to-cloud CC), and cloud-to-air discharges (collectively abbreviated as IC). An schematic overview is given in Figure 2.9. Approximately 90 % of CG lightning strikes are negative and downward, meaning that negative charge is transferred from higher regions within the cloud toward the Earth's surface. Other types of CG lightning, such as positive, upward-directed, or even bipolar discharges (featuring both positive and negative channels), are theoretically possible but occur much more rarely. Lightning acts as a natural

mechanism to balance the electrical charge differences that accumulate in thunderstorms over time. Through induction, it releases the stored electrical energy of the charged cloud by channeling it into electrical currents that flow through ionized, highly conductive lightning channels. The majority of this energy is converted into heat, which causes atmospheric gases to dissociate, become excited, and then recombine, resulting in intense light emissions at specific spectral lines. Simultaneously, the rapid heating and expansion of air around the lightning channel creates a shock wave, which can be heard as thunder. Since sound travels more slowly than light, the thunder is heard with a noticeable delay after the lightning flash. This time lag can be used to estimate the distance to the lightning strike. It is important to note that lightning channels transport charge in steps and may trigger the formation of secondary branches. As a result, charge is not transported directly to the ground in a single movement but rather gradually, through a series of steps that begin with the initial lightning strike known as the stepped leader.
According to the GDV (*Gesamtverband Deutscher Versicherer*; German Insurance Association) lightning statistics, around 220,000 lightning and surge damage claims were reported in 2024 and 2023, respectively, resulting in significant financial losses. Household contents and residential building insurers paid out approximately €350 million in compensation in 2024 (Gesamtverband Deutscher Versicherer, 2025).

2.3.3. Lightning detection

Lightning detection are important observational data for analyzing thunderstorm processes, validating atmospheric models, and assessing severe weather hazards. There are three frequency ranges in which measurement systems operate (Guha et al., 2021):
Very high frequencies (VHF; 30-300 MHz), low frequencies (LF; 30-300 kHz), and very low frequencies (VLF; 3-30 kHz). A distinction can be drawn between ground- and space-based systems.
The latter are placed on satellites and usually determine the optical transient of lightning. The spatial coverage is high, but at the same time the resolution is low. Therefore, the total lightning is determined, rather a distinction between ICs and CGs (Guha et al., 2021).
Lightning detection systems on the ground operate by measuring electromagnetic emissions across various frequency ranges, with the choice of range affecting accuracy and coverage. High-resolution detection (on the order of meters) is possible using VHF signals, though it requires a dense network of sensors. In contrast, using LF or VLF frequencies allows for broader coverage with fewer sensors, but at the cost of reduced spatial precision—typically

with localization errors of one to several kilometers.
Lightning location systems commonly rely on three techniques (Guha et al., 2021). The magnetic direction finding (MDF) technique estimates the direction to a lightning discharge by measuring the magnetic field with orthogonally arranged loop antennas. Each sensor determines the azimuth angle between its location and the lightning strike. By intersecting the directional vectors from at least two sensors, the strike location can be triangulated. Using more sensors improves positional accuracy and reduces directional ambiguity. Time-of-arrival (TOA) calculates the location based on the time differences of signal arrivals at multiple sensors, with different baselines and frequency ranges enabling both high-resolution mapping and wide-area coverage (Guha et al., 2021). Interferometry estimates the direction of radiation sources by analyzing phase differences of narrow band signals received at closely spaced antennas, allowing for precise three-dimensional reconstruction of lightning channels (Guha et al., 2021).

2.3.4. Climate Change impact on lightning

Lightning has an impact on climate, but it is also influenced by climate change. Lightning initiates chemical reactions in the atmosphere that produce the ozone precursor NOx (Franzblau and Popp, 1989), and it is a major cause of wildfires (Veraverbeke et al., 2017), which in turn release large amounts of greenhouse gases. As a result, lightning contributes to climate change. On the other hand, climate change and the associated warming of the atmosphere also alter lightning activity. However, current studies show differing results when projecting future lightning trends. These discrepancies primarily arise from differences in model parameterization and uncertainties in microphysical processes.
Romps et al. (2014) proposed that lightning flash rates are proportional to both precipitation rates and CAPE. Based on this relationship, an increase in lightning activity in the USA is expected due to climate change.
Clark et al. (2017) found that simulations using different lightning parameterization schemes in the Community Atmospheric Model (CAM5), such as those based on cloud-top height and cold-cloud depth, produced varying results in lightning flash density under the Representative Concentration Pathway 8.5 (RCP8.5) scenario. Depending on the parameterization scheme, lightning activity either increased strongly, increased moderately, or even decreased. The authors argue that results showing a decrease in lightning flash density are less reliable, as the corresponding parameterizations perform poorly when compared with current observations. The increase in lightning activity may be related to a shift in the 0 °C isotherm

due to warming tropospheric temperatures (Clark et al., 2017).
In contrast, Finney et al. (2018) employed a different approach by incorporating cloud-ice fluxes rather than cloud-top height into their lightning parameterizations. Their simulations showed a decrease of approximately 15 % in total lightning flash rate by the end of the century under strong global warming conditions. They argue that this method is more closely related to the physical processes of cloud electrification and is therefore more reliable than approaches based on cloud-top height, which tend to project an increase in global lightning activity.
Similarly, Whaley et al. (2024) implemented a lightning parameterization scheme into the Canadian Atmospheric Model (CanAM5.1) and found little change in the global mean lightning flash rate, but notable regional variations: A decrease in the tropics and an increase in the northern mid-latitudes. Additionally, in the northern mid-latitudes, simulations with interactive, evolving lightning produced three times more burned area than runs with unchanging, climatological lightning, demonstrating that the choice of lightning parameterization strongly influences projections of future fire activity.
Despite advances in lightning parameterization and observational datasets, there are still significant uncertainties in modeling schemes and lightning detection. This makes it difficult to identify reliable trends in future lightning activity. Therefore, one of the objectives of this thesis is to improve our understanding of the relationship between environmental conditions and lightning activity, with the aim of providing a more accurate explanation of trends in lightning activity.

2.4. Aerosol effects

Aerosols can influence thunderstorm development through both microphysical and radiative effects, affecting cloud formation, precipitation processes, and storm electrification.
The radiative effect refers to the direct influence of aerosols on radiation. Aerosols can stabilize the boundary layer by warming the aerosol layer aloft while reducing surface heating through scattering and absorption of solar radiation. This shading effect weakens convection and suppresses boundary layer cloud formation (Koren et al., 2004). Microphysical effects describe processes on smaller scales that directly affect cloud and lightning formation. Increasing aerosol concentrations generally lead to more cloud droplets, but this relationship is not linear. At moderate aerosol loadings, droplet concentrations rise until a saturation point is reached. At very high concentrations, large particles may limit supersaturation and inhibit the activation of smaller droplets, or intense competition for

water vapor can cause evaporation of the smallest droplets. Additionally, droplet activation strongly depends on aerosol size, composition, and local supersaturation, so aerosol optical depth (AOD) alone is not always a reliable indicator of the indirect effect (Feingold et al., 2001). The AOD quantifies the total extinction of incoming solar radiation due to aerosol scattering and absorption within the atmospheric column. It is a dimensionless quantity, expressed on a logarithmic attenuation scale. Since this effect depends on the wavelength, AOD is typically reported for specific spectral bands rather than as a broadband quantity. High concentrations of CCN tend to delay precipitation and glaciation to higher altitudes in convective clouds (Rosenfeld et al., 2014). Smaller cloud droplets collide and coalesced less efficiently, slowing the development of large drops and delaying downdrafts and warm-rain processes (Koren et al., 2005).

These effects prolong cloud lifetime and allows lighter droplets to rise higher, potentially enhancing conditions favorable for lightning (Dayeh et al., 2021). Accordingly, Westcott (1995) observed a 40-85% increase in lightning frequency near urban areas in the USA. Consistent with Feingold et al. (2001), Wang et al. (2018) reported a non-linear relationship between lightning flash rate and AOD, showing an initial increase with rising AOD, followed by saturation and a subsequent leveling off or slight decrease at higher values. Under low aerosol loading, microphysical effects dominate, enhancing deep convection, whereas at high aerosol loading, radiative effects become more pronounced and can suppress cloud development (Wang et al., 2018). However, Jiang et al. (2018) found convection to be enhanced (polluted continental aerosol) or suppressed (smoke) depending on the aerosol amount and type and the region (dust). Moreover, according to them, the aerosol-induced inhibition or enhancement effects do not change monotonically with AOD and are strongly dependent on aerosol type.

Atmospheric aerosols can be described using several observational variables, with the AOD being a key one. Additionally, Particulate Matter (PM) provides a complementary description of the aerosol composition, classified according to particle aerodynamic diameter. PM_{10} includes particles up to 10 µm, while $PM_{2.5}$ and PM_1 include particles up to 2.5 µm and 1 µm, respectively Finally, the total column represents the vertically integrated mass of a specific aerosol species within an atmospheric column. Together, these variables allow for a detailed description of the atmospheric aerosol load relevant to convective and electrification processes.

However, the overall influence of aerosols on storm electrification remains uncertain, with reported effects varying according to type, concentration and region. The aim of this study is therefore to investigate these interactions by examining the relationship between lightning activity and atmospheric aerosols along PHT.

3. Data and methods

This chapter outlines the data sources and methods used to analyze lightning characteristics along radar-detected PHTs. First, the lightning data from EUCLID are presented, followed by a description of the radar-based PHTs derived with the TRACE3D algorithm and other related variables. To improve the understanding of the environmental conditions influencing lightning activity, the convective parameters from Taszarek et al. (2020) and the atmospheric aerosol variables (Copernicus Atmosphere Monitoring Service, 2020, Inness et al., 2019) are introduced. Subsequently, the methods used to combine lightning data with PHTs are described, including an additional analysis of spatially clustered tracks. Finally, the methodology for linking these datasets to the environmental conditions is described.

3.1. Data

The analysis in this thesis covers the months from April to September for the years 2005 to 2023, representing the main thunderstorm season in the mid-latitudes. The radar-derived PHTs are available only for Germany and adjacent regions. Therefore, the spatial domain is restricted to the following coordinate limits: 53.8° N; 16° E; 47° N; 3° E (see Figure 3.1).
Although the original dataset extends further north to approximately 54.9°N, this northernmost band was excluded from the analysis because it contained an unrealistically high number of PHTs without any corresponding lightning activity. This discrepancy was identified during quality control and discussed before removing the affected region.
To provide an overview of the datasets, Figure 3.1 displays all detected lightning strikes and radar-detected PHTs for 13 July 2016. It shows that lightning occurs in the vicinity of PHTs, but also independently of them.

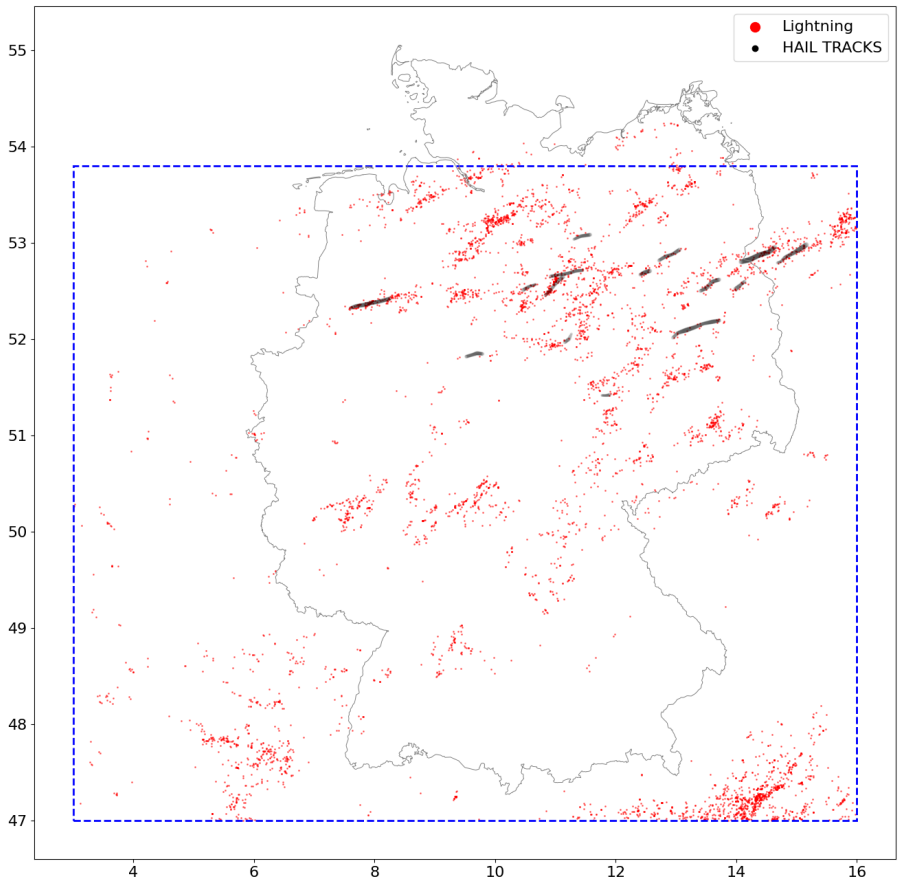

Figure 3.1: Example of lightning strikes (red) and radar-detected PHTs (black) combined for one day (13 July 2016). The blue box marks the study region.

3.1.1. Lightning

The ground-based European Cooperation for Lightning Detection (EUCLID) is a network formed in 2001 through the integration of several national lightning detection systems across Europe (Schulz et al., 2016; Poelman et al., 2016; Poelman and Schulz, 2020). The aim of this cooperation is to provide a homogeneous and consistent lightning dataset. EUCLID benefits from greater redundancy, since lightning strokes are detected by sensors both within and beyond national borders (Schulz et al., 2016).
EUCLID detects and locates CG and IC discharges using a combination of TOA and direction-finding (DF) methods in the LF range (see subsection 2.3.3; Poelman and Schulz, 2020).
In recent years, the performance of the EUCLID network has continuously improved as a result of various software and hardware upgrades (Schulz et al., 2016). A validation study based on ground-truth data from direct lightning current measurements at the Gaisberg Tower, as well as E-field and video recordings from Austria, Belgium, and France, con-

firmed significant progress in location accuracy and detection efficiency (Schulz et al., 2016). Currently, the median location accuracy reaches about 100 m in the network's center and remains below 500 m across most regions. Detection efficiency is comparable in Austria and Belgium, while slightly lower values were observed in parts of France due to temporary sensor issues. The estimation of peak current for subsequent strokes was found to be reasonable, considering that it is derived from radiated electromagnetic fields under the assumption of a constant return stroke speed (Schulz et al., 2016).
From this dataset, the geographical coordinates, timestamp with an millisecond resolution, type, peak current, and polarity of each lightning stroke are available. In this thesis, the analysis primarily focuses on the spatial and temporal characteristics of the lightning data in order to combine them with the PHTs. Unless stated otherwise, only CG lightning strikes are considered. While total lightning strike counts are available, the CG-only dataset is homogeneous in both time and space, allowing consistent assessment of trends (Augenstein et al., 2024, Augenstein, 2025).

3.1.2. Radar-detected PHTs

The PHTs were derived from radar data and identified using the TRACE3D algorithm, originally developed by Handwerker (2002) and later adapted by Schmidberger (2018), which is applied in this study.

Data basis
The cell tracking algorithm is applied to the data from the radar network of the German Weather Service (*Deutscher Wetterdienst*, DWD). In total, there are 17 radar devices in Germany (Memmingen since 2015, before 16 devices), each covering a radius of 125 km at the beginning of the study period, increasing to 150 km from 2015 onward. The radars are operated in two different modes: with a volume scan and one precipitation scan (see Figure 3.2).

The first mode is the basis for the cell tracking algorithm, whereas the second is used to derive reflectivity core-related variables, which are described later in this section. During the volume scan, the antenna covers 18 elevation angles between 0.5° and 37° every 15 minutes, reaching altitudes of up to 12 km (Bartels et al., 2005). This scan includes an intensive mode for lower elevations (0.5° - 4°, range up to 230 km) and a Doppler mode for higher elevations (range up to 120 km). A single-elevation precipitation scan is performed every five minutes between two volume scans to quantify the precipitation that reaches the

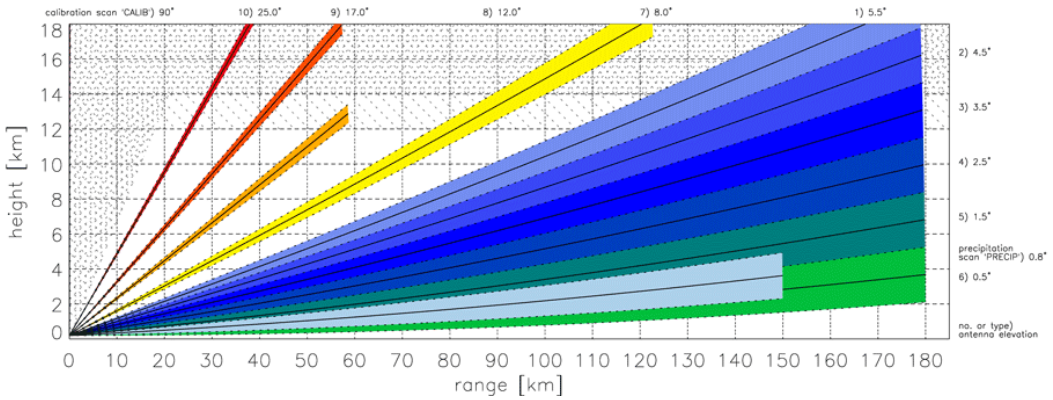

Figure 3.2: Schematic illustration of the scanning strategy of the weather radar systems of the DWD radar network. It shows the individual elevation angles, each representing a full azimuthal antenna rotation (indicated by color shading). Light blue shading indicates the precipitation scan, while other colors indicate the volume scan. The radar system is located at the origin of the coordinate system. From Helmert et al., 2014.

ground (see also: Intensity variables). After the radar network upgrade to dual-polarization systems between 2011 and 2015, the scanning strategy has been revised (Helmert et al., 2014). It now begins with the precipitation scan, followed by the multi-elevation volume scan, with horizontal range decreasing as elevation increases.

During the study period, several radar outages occurred, due to maintenance, system modernization, and partly as a result of technical malfunctions. However, the spatial configuration of the network ensures that most regions are covered by at least two radar stations, with the exception of the southern and southeastern edges of Germany, where coverage, especially before the Memmingen station became operational, was comparatively weaker (Schmidberger, 2018). Overlapping scan areas and the use of fail-safe radars help to minimize data gaps in these regions.

The data is provided in polar stereographic projection (φ, λ; RADOLAN format) and must be converted to a common Cartesian grid (x,y) using the following equations:

$$x = R \cdot M(\varphi) \cdot \cos(\varphi) \cdot \sin(\lambda - \lambda_0) \ , \tag{3.1}$$

$$y = -R \cdot M(\varphi) \cdot \cos(\varphi) \cdot \cos(\lambda - \lambda_0) \tag{3.2}$$

with the stereographic scaling factor $M(\varphi) = \frac{1+\sin(\varphi_0)}{1+\sin(\varphi}$, $\varphi_0 = 60°$ N, the latitude where the projection plane intersects the Earth's surface, and $\lambda_0 = 10°$ E, the meridian to which the Cartesian coordinate system is aligned. (Bartels et al., 2005; Helmert et al., 2014; DWD, 2025)

TRACE3D algorithm

Unless otherwise stated, the following description of the algorithm is based on Handwerker (2002).

The TRACE3D algorithm identifies and tracks convective cells in space and time in spherical coordinates from the radar data of the C-band Doppler radar from the Institute of Meteorology and Climate Research Troposphere Research (IMKTRO) of Karlsruhe Institute of Technology (KIT)(former: *Forschungszentrum Karlsruhe*). It is important to note that the identified regions do not represent actual convective cells but are rather approximations. Therefore, the term reflectivity core (RC) is used in the following, since the only input is radar reflectivity data. Although TRACE3D assumes that the radar data have already been corrected for major artifacts, it still applies several simple adjustments to reduce typical radar errors. These include removing ground clutter by excluding data below a certain height and compensating for attenuation effects by slightly increasing reflectivity with distance from the radar. Furthermore, nearby small RCs are merged into larger ones, while very small RCs likely caused by noise or non-meteorological echoes are discarded. Finally, the algorithm minimizes false detections of bright bands as convective cells by requiring that RCs appear across multiple elevation angles. A bright band is a narrow zone of enhanced radar reflectivity near the melting layer, caused by partially melted snowflakes with water coatings that strongly reflect microwave energy (Markowski and Richardson, 2010). These wet flakes often clump together into large aggregates, further increasing reflectivity. Below the melting layer, as the flakes fully melt into smaller raindrops, reflectivity decreases.

To identify RCs correctly, TRACE3D combines several simplified approaches, shown in Figure 3.3. The first approach identifies each radar volume element exceeding a given reflectivity threshold (dBZ_{LIMIT}) as part of a RC. However, this often results in unrealistically large RCs that may actually consist of multiple smaller cells. A second approach identifies relative maxima in the reflectivity field and defines a RC as all surrounding elements whose reflectivity values are no more than dBZ_{DIFF} below the local maximum. While this method better distinguishes individual cells, it can still create artifacts when adjacent maxima merge incorrectly. Therefore, TRACE3D applies a combined method. In a first step, Regions of Intense Precipitation (ROIPs) are identified where reflectivity exceeds dBZ_{LIMIT}. For each ROIP, the maximum reflectivity value is determined. Within this region, a RC is then defined as the contiguous area where reflectivity values exceed this maximum minus dBZ_{DIFF}. In contrast to the second approach, the lower threshold is thus determined by the ROIP maximum rather than by individual local maxima.

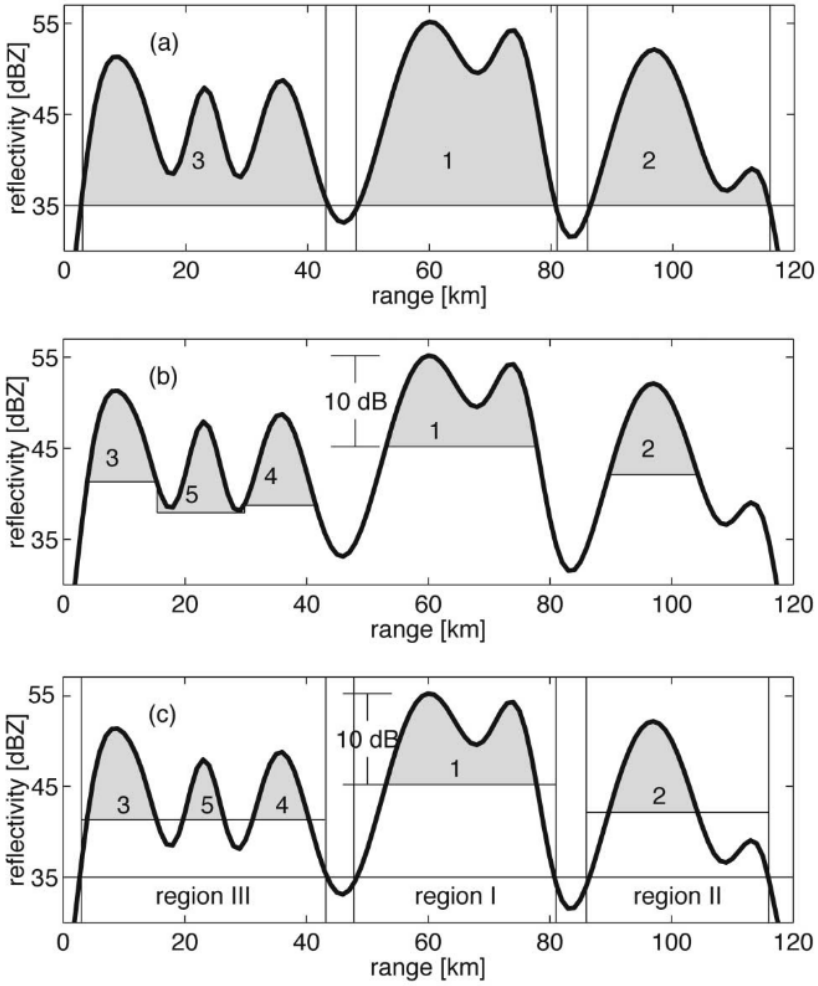

Figure 3.3: Illustration of different approaches to identify reflectivity cores (RCs): (a) All radar volume elements exceeding a fixed reflectivity threshold (35 dBZ) are grouped into RCs. (b) RCs are defined as the upper 10 dBZ (dBZ_{DIFF}) around local maxima. (c) TRACE3D first identifies contiguous regions above 35 dBZ and then defines RCs within each region as areas where the reflectivity remains within 10 dBZ of the local maximum. From Handwerker, 2002.

The basic principle of cell tracking is based on estimating the movement of an identified RC between two time steps. Given the position $s - \Delta s$ of a RC at the previous scan $t - \Delta t$ ("parent RC") and the time interval Δt between radar scans, the expected new position s can be predicted using the estimated advection velocity. TRACE3D then checks whether a RC detected near this predicted location ("child RC") corresponds to the parent RC and, if so, establishes a linkage between them. If no suitable match is found, this may indicate a merger of multiple cells into one. Or conversely, a split of the parent RC into several child RCs with different or similar structures may lead to several matches.
For the tracking four scenarios are possible:

(1) When the RC existed already for one timestep, the velocity from $t - 2\Delta t$ to $t - \Delta t$ can be used to estimate its position s at t.
(2) When the RC existed longer than one timestep, the previous velocities can be used for the next estimation as weighted by their distance of time.
(3) When the RC exists for the first time, its velocity is assumed to be the average velocities of its nearby, longer existing RCs. In case of no other RCs, the velocity is estimated by the Volume Velocity Processing (VVP) algorithm from Waldteufel and Corbin (1979).
(4) When even the VVP algorithm is not available, the RC of the next timestep closest to the RC is assumed to be the child RC, as long as the velocity is smaller than $15\,\mathrm{m\,s^{-1}}$.
Based on this estimated advection velocity, a new position of each RC can be predicted. All RCs located within a defined search radius around this estimated position are considered as potential child RCs. The size of the search radius depends on the estimated displacement distance of the RC and the distance to the nearest neighboring RC in the previous volume scan.
Not only the position of a RC evolves over time, but also the spatial extent. The cases where the area of a RC changes drastically are splitting of cells in two or more smaller ones and the opposite, a merging of cells. As this changes the trajectory of RC in relevant way, TRACE3D has to consider this feature. In order to identify splitting, the whole parent RC from timestep $t - \Delta t$ is moved to the position of the found child RC at timestep t. When the area of the child RC is significantly smaller than the area from its parent RC, splitting is very likely, otherwise not. TRACE3D identifies regions of the parent RC that are not covered by the child RC and evaluates whether additional RCs are present nearby. Only RCs whose centers lie within a defined distance relative to these uncovered regions and the parent displacement are considered. These RCs are then treated as additional child RCs, representing a potential splitting of the parent RC. An example is shown in Figure 3.4. The merging of RCs in consecutive timesteps is determined in the same way, but in reverse.

The assignment procedure between parent and child RCs is initially permissive, allowing multiple potential matches. To identify unlikely assignments, TRACE3D calculates which connections would result in a crossing of RC trajectories, assuming linear motion within a timestep. All RCs involved in potential crossings are grouped, and the average velocity for the group is determined. Assignments that best match this average velocity are accepted, while conflicting connections causing crossings are rejected. This process is repeated iteratively until all remaining assignments are consistent and no trajectory crossings remain.
In most cases, the assignments between parent and child RCs are reliable. However, tracking becomes difficult when multiple RCs are in close proximity, such as within a squall line,

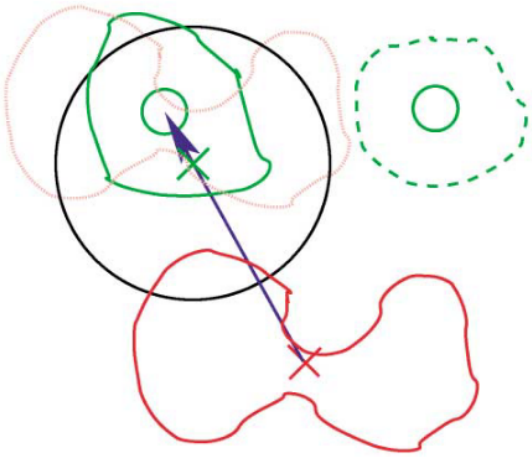

Figure 3.4: Schematic illustration of RC splitting in TRACE3D. The *parent RC* at timestep $t - \Delta t$ (solid red line) is shifted to the estimated position of the identified *child RC* at timestep t (solid green line; parent position indicated by dashed red line). The areas of the parent and child RCs are compared. If parts of the parent RC are not covered by the child, additional nearby RCs (dashed green line) are considered as potential child cores. From Handwerker (2002).

because rapid growth, decay, splitting, and merging can occur between scans. TRACE3D identifies these situations by grouping interconnected RCs and designating any group with three or more parent and child RCs as a "heap of RCs". Within a heap, each parent is assigned to only one child and vice versa, and splitting or merging is not allowed. The average velocity of all assignments within the heap is calculated, and assignments are accepted according to their consistency with this velocity, while preserving information to reconstruct the heap if needed.

Adjustment of TRACE3D

Since TRACE3D was originally developed for the KIT radar system, Schmidberger (2018) implemented several modifications to enable its application to multi-radar networks and radar data in cartesian coordinates. The following description is therefore, unless otherwise stated, based on Schmidberger (2018).

The *PZ* product of each radar station from the DWD network covers an area of $400 \times 400\,\mathrm{km}^2$ with a horizontal resolution of $2 \times 2\,\mathrm{km}^2$ and 12 vertical levels spaced 1 km apart, starting 1 km above ground. Radar reflectivity is classified into six discrete categories ((7, 19]; (19, 28]; (28,37]; (37, 46]; (46, 55]; and (55, ∞) dBZ), which introduces some uncertainty in hail detection, but still provides advantages over 2D projections. This discretization limits precise adjustment of the thresholds dBZ_{LIMIT} and dBZ_{DIFF} for distinguishing neighboring cells. Since only the two highest reflectivity classes are relevant for identifying convective

events, RCs must be defined based on the highest reflectivity class, corresponding to a threshold of 55 dBZ. The next lower class serves as the lower boundary; otherwise, dBZ_{DIFF} would become too large, merging individual convective cells, and including areas without convection. This is in alignment with the Mason criterion from Mason (1971) (see also subsection 2.2.2). To create a composite, the individual radar datasets are merged into the $900 \times 900\,\mathrm{km}^2$ DWD grid with 1 km resolution, where overlapping areas are resolved by assigning the maximum reflectivity value at each grid point. To ensure reliable detection, a RC must exceed the highest class $(55, \infty)$ at least at two elevation levels, while also including the second-highest class $(49, 55]$. Additionally, the threshold exceedance must occur across at least four contiguous radar pixels to exclude artificial values. In practice, this defines a potential hail cell as a RC with reflectivities above 55 dBZ extending over at least 1 km vertically, surrounded by reflectivities above 46 dBZ. Using this approach, TRACE3D is able to robustly identify strong convective events and track their signatures across consecutive timesteps, allowing successful cell tracking even with the coarse resolution of the DWD radar composite

The projected 2D horizontal area of each identified RC is referred to as its footprint. For every RC, two footprints are considered: one representing the area with reflectivity values of at least 55 dBZ, and one for values of at least 46 dBZ. In the following, variables associated with each footprint are labeled with *55* or *46* to indicate the corresponding threshold.
From the resulting TRACE3D dataset, both the start and end times of every PHT, as well as the geographical coordinates of the RC center with reflectivity of 55 dBZ at each timestep, are available. The latter describe the center of the RC_{55} at every timestep, determined as the midpoint between the northernmost and southernmost points (y-coordinate) and the westernmost and easternmost points (x-coordinate) of its footprint. Given the 15 min temporal resolution of the DWD radar data, the timestamp of each RC throughout the lifetime of a PHT is therefore known.

Reflectivity core attribution

The PHTs generated by the TRACE3D algorithm, based on the volume scan of the DWD radar system, contain only basic spatial and temporal information. To obtain additional details and descriptive variables regarding the precipitation intensity of thunderstorms, radar data from the precipitation scan are used (RX; Bartels et al. (2004)). As shown in Figure 3.2, this scan is near-surface and approximately follows the orography, with a range of about 150 km. It should be noted that the procedure used by the DWD to derive precipitation intensity (RX) changed in 2012. Prior to this, the reflectivity value was taken from the

closest grid point. Afterwards, it is calculated as the mean of the surrounding grid points. The temporal resolution is 5 min. To match the resolution of the PHTs, the nearest rounded time step is selected.
The variables are based on the RC footprints introduced above, represented by RC_{46} and RC_{55}, respectively. The variable $RXMax3$ represents the mean of the three highest reflectivities within the footprint of RC_{46} at a given time step. The variable $LSinA46$ denotes the number of lightning strikes within the footprint of RC_{46} at that time step, and analogously, $LSinA55$ refers to the strikes within RC_{55}. The data source for the lightning strikes is the same as described in subsection 3.1.1. However, the temporal window for selecting lightning strikes is set to 2.5 min before and after the timestamp of the respective RC, due to the temporal resolution of the precipitation scan. It should be noted that these two variables are conceptually similar to those used elsewhere in this thesis. But the approach presented here applies a constant selection area A for assigning lightning to PHTs (see section 3.2), whereas $A46$ and $A55$ vary not only between each other but also from one time step and RC to another. Lightning strikes occurring outside hail storms are also captured by this approach due to the use of a constant selection radius. The intensity variables are derived for each RC and are available in the same temporal and spatial resolution as the radar-detected PHTs. The geographical coordinates describe the center of RC_{55} at each time step, analogous to the definition used for the PHTs. The processing of radar data and the derivation of intensity variables were carried out by M. Augenstein. In this thesis, only the resulting data are used for further analysis (M. Augenstein, personal communication, 17.09.2025).

3.1.3. Environmental conditions associated with PHTs

As discussed in chapter 2, the initiation of convection, and thus the occurrence of lightning and hail, is strongly influenced by the prevailing atmospheric conditions. To better understand the relationship between lightning and hail, it is therefore essential to further investigate the environmental parameters that favor convective development.

Convective parameters
A common approach to characterize convective environments is through the use of thermodynamic and kinematic parameters, as described by Taszarek et al. (2020). In their study, the fifth-generation ECMWF reanalysis (ERA5) dataset (Hersbach et al., 2020) was employed, featuring a horizontal resolution of 0.25°, hourly temporal resolution, and 137 terrain-following hybrid-sigma levels. For the derivation of convective parameters, ERA5

profiles were generated by vertically interpolating key meteorological variables, including temperature, humidity, pressure, geopotential, and horizontal wind components. In parcel-based calculations, virtual temperature corrections were applied to account for moisture effects, and the mixed layer (ML) was defined as the layer extending from the surface up to 500 m above ground level. The CAPE and CIN parameters are derived from the integration of positive and negative buoyancy, respectively, for each parcel: between the LFC and EL for CAPE, and between the parcel's initialization height and the LFC for CIN.
The convective parameters used in this study were derived by Mateusz Taszarek using the R package *thunder* for the computation and visualization of atmospheric convective parameters (Czernecki et al., 2025). The theoretical background of these convective parameters is presented in subsection 2.1.2.
In addition to the convective parameters described by Taszarek et al. (2020), convective precipitation data from ERA5 (Copernicus Climate Change Service, 2023; Hersbach et al., 2023) are used here to better assess whether convection has already occurred. This variable represents the accumulated amount of precipitation generated by the convective scheme of the ECMWF Integrated Forecasting System (IFS) within a single grid cell over one hour. It is expressed as the water depth (in meters) that would result if the accumulated precipitation were evenly distributed across the grid cell. The temporal and spatial resolution is identical to that of the convective parameters described above.

Reanalysis of aerosols

In addition to thermodynamic and kinematic parameters, aerosols also plays an important role in thunderstorm development. They can serve as nuclei for cloud and ice particle formation, increasing the number of INPs and CCNs and thereby influencing thunderstorm electrification (see section 2.4). In general, soluble aerosols serve as CCNs and insoluble as INPs (Ross and Lasher-Trapp, 2025), combinations are also possible.
To investigate these effects, the fourth-generation ECMWF Atmospheric Composition Reanalysis (EAC4) is used, providing data with a spatial resolution of 0.75° and a temporal resolution of 3 h (Copernicus Atmosphere Monitoring Service, 2020). The variables considered in this study and their corresponding units are summarized in Table 3.1 and defined in section 2.4. The parameters were selected to provide a broad overview of different aerosol types in terms of sources and particle sizes.
AOD describes the column-integrated effect of aerosols on the attenuation of incoming solar radiation through scattering and absorption. In addition, PM offers a complementary perspective on aerosol properties by categorizing particles according to their aerodynamic diameter. The total column quantity describes the vertically integrated mass of a given

aerosol species across the entire atmospheric column. Black carbon (BC) can serve as INP (Hoose and Möhler, 2012) and is a directly emitted aerosol originating from incomplete combustion of fossil fuels, biofuels, and biomass. Its typical lifetime in the troposphere is about seven to ten days (Seinfeld and Pandis, 2016). Mineral dust is released naturally through wind erosion of soil particles and anthropogenically through traffic and industrial activities. Due to its typical lifetime of about two weeks, it can be transported over thousands of kilometers (Seinfeld and Pandis, 2016). It can also serve as INP (Hoose and Möhler, 2012). Combustion of fossil fuels and biomass also produces a complex aerosol mixture known as organic matter, which spans a wide range of particle sizes. Sulfate aerosols originate from both natural and anthropogenic sources. They can be emitted directly through marine and volcanic activity or form secondarily via oxidation of sulfur compounds released by industrial processes, fossil fuel combustion, biomass burning, and other biogenic sources (Seinfeld and Pandis, 2016; Bozzo et al., 2017). Sulfur dioxide (SO_2), which is oxidized to form sulfate, originates predominantly from anthropogenic processes and volcanic eruptions. Sea salt aerosols are mainly produced by wind-driven processes at the ocean surface. When waves break, bubbles burst and release particles into the atmosphere, and at higher wind speeds spume generation adds larger droplets. Their typical lifetime ranges from one day to one week (Seinfeld and Pandis, 2016).

Table 3.1: Overview of variables from the fourth-generation ECMWF Atmospheric Composition Reanalysis (EAC4) describing atmospheric aerosols, including Aerosol Optical Depth (AOD), Particulate Matter (PM), and total column amount for various aerosol species (Copernicus Atmosphere Monitoring Service, 2020, Inness et al., 2019).

variable	description	unit
bcaod550	black carbon AOD at 550 nm	[ ]
duaod550	dust AOD at 550 nm	[ ]
omaod550	organic matter AOD at 550 nm	[ ]
PM_1	PM with diameter < 1 µm	$kg\,m^{-3}$
$PM_{2.5}$	PM with diameter < 2.5 µm	$kg\,m^{-3}$
PM_{10}	PM with diameter < 10 µm	$kg\,m^{-3}$
ssaod550	sea salt AOD at 550 nm	[ ]
suaod550	sulfate AOD at 550 nm	[ ]
aod550	total AOD at 550 nm	[ ]
tcso2	total column sulfur dioxide	$kg\,m^{-2}$

3.2. Methods

3.2.1. Assignment of lightning strikes to PHTs

To investigate the relationship between hail occurrence, lightning activity, and the surrounding environmental conditions, the datasets described above were combined through a spatial and temporal assignment procedure.
Because the PHTs have a temporal resolution of 15 min, while the lightning data provide timestamps in milliseconds, the lightning selection was based on 15 min intervals. To account for the fact that, due to the radar scanning process, individual track points do not occur exactly 15 min apart and that the RC moves within a single time step, all lightning strikes occurring within 7.5 min before and after the timestamp of each track point were included. Subsequently, a spatial filtering was applied by selecting all lightning strikes within a 15 km radius around each track point.
In Figure 3.5, the small colored dots represent all lightning strikes occurring in temporal proximity to the PHT, based on the applied time filter of 7.5 min before and after the timestamp of each track point. The green dots indicate the strikes selected after the additional spatial filtering within a 15 km radius, forming the final sample for the subsequent analysis. As illustrated by the different highlighted selection radii in the panels of Figure 3.5, these steps are repeated for each track point.
This specific selection radius is chosen to ensure that lightning strikes associated with PHTs are captured comprehensively. It accounts for the mean PHT width of 5.8 km (Schmidberger, 2018) and the average distance between consecutive track points of 9.3 km. Furthermore, previous studies (e.g., Changnon, 1992) have shown that lightning often occurs outside the immediate hailstreak, in adjacent regions of the storm. The same radius has also been applied in other studies (Wapler, 2017). A radius of 15 km therefore provides a balance between including relevant lightning activity and avoiding excessive spatial overlap with unrelated convective systems.
The resulting dataset contains, for each track point, the number of associated lightning strikes as well as detailed parameters from the original lightning dataset described above.

3.2.2. Clustering of PHTs

The analysis in this thesis focuses on the consideration of radar-detected PHTs as individual entities. However, lightning characteristics are also determined for categorized PHTs. For

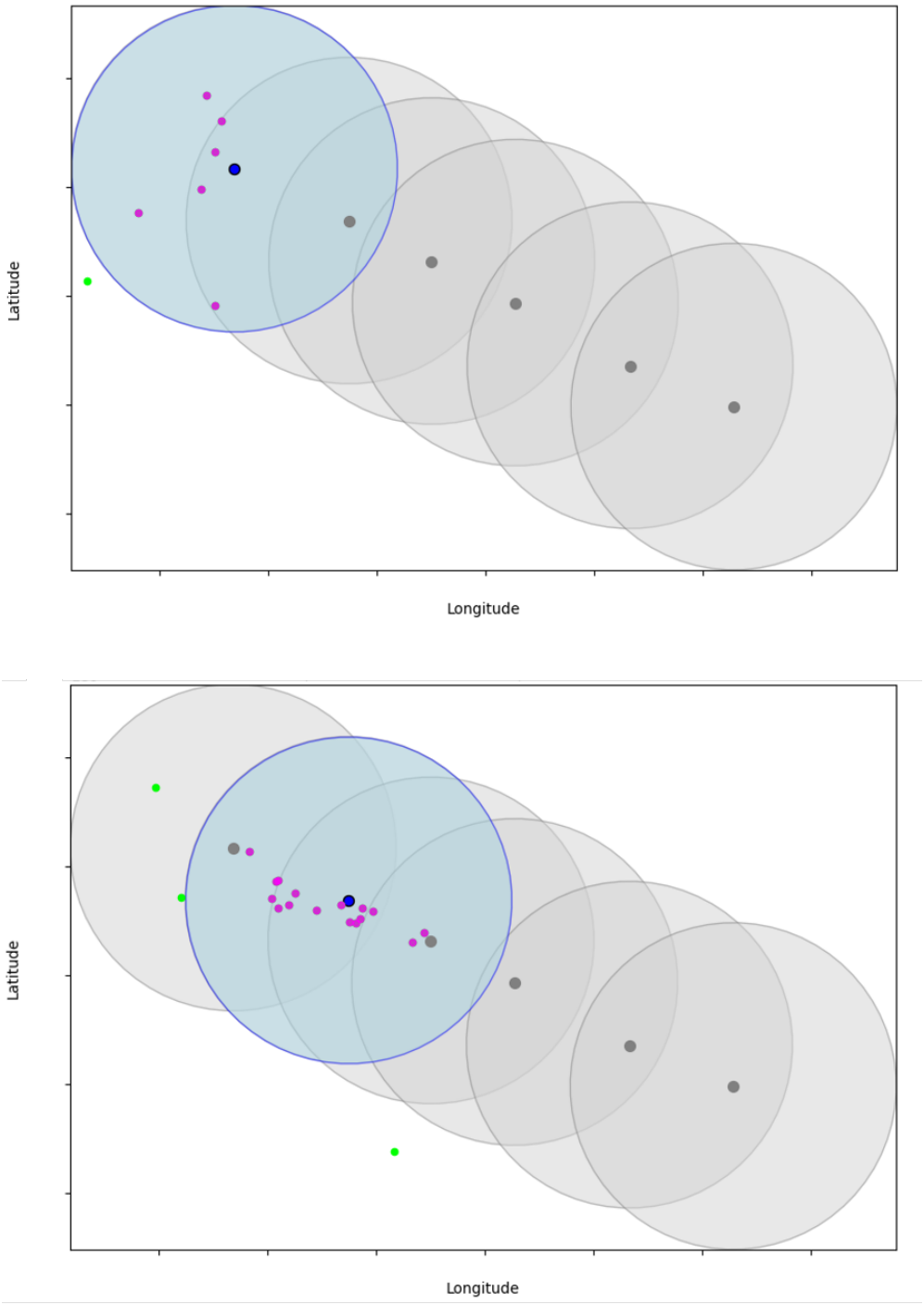

Figure 3.5: Example of the assignment of lightning strokes to radar-detected PHTs. (a) shows the first time step of the track, (b) the second. The bold dots (blue and gray) represent the consecutive track points forming the PHT. Circles (blue and gray) indicate the selection areas with a radius of 15 km. The currently considered track point and its selection area are highlighted in blue. The smaller colored dots denote lightning strokes detected in the spatial and temporal vicinity of the respective track point. Green dots mark lightning strikes that occur within the 15 min interval around the track point timestamp (7.5 min before and after) but at distances greater than 15 km. Pink dots represent the lightning strikes actually assigned to the track. This procedure is applied analogously to each track point.

this purpose, individual PHTs are classified into *single*, *clustered*, and *long* PHTs using the ST-DBSCAN algorithm from Birant and Kut (2007).

The ST-DBSCAN algorithm is a modification of the DBSCAN (Density-Based Spatial Clustering of Applications with Noise) algorithm from Ester et al. (1996), specifically designed for spatio-temporal data. Clustering is a common data mining technique used to identify patterns and relationships within large datasets by grouping similar data points. While traditional clustering methods are designed for non-spatial and non-temporal data, spatio-temporal clustering must additionally consider both the spatial and temporal neighborhood of objects, making the process considerably more complex. Density-based clustering algorithms detect clusters by identifying regions of high data point density within a dataset, while areas of lower density act as boundaries between clusters.

This algorithm is also commonly used for convection analysis (Augenstein et al., 2024, Kopp et al., 2024, Augenstein, 2025, Schmid et al., 2025)

The ST-DBSCAN algorithm is based on three input parameters (Birant and Kut, 2007). The first, ϵ_{space}, describes the maximum spatial distance that points can have to still belong to the same cluster. Analogously, the parameter ϵ_{time} defines the maximum temporal distance allowed for points to be clustered together. The last parameter, $MinPts$, specifies the minimum number of points required for a region to be considered dense.

The classification of the PHTs starts with the distinction between *long* and *short* tracks. *Long* tracks are tracks with more than seven time steps, which is about 1 h45 min. All the other tracks are preliminary classified as *short*. For the clustering of the *short* PHTs the following parameter values are chosen: $\epsilon_{space} = 40\,\text{km}$; $\epsilon_{time} = 25\,\text{min}$; $MinPts = 3$. This means that if more than three PHTs occur within 40 km in 25 min, they are classified as *clustered*, otherwise as *single*. A sensitivity analysis was conducted by testing several parameter configurations and combinations, which yielded consistent and robust results, indicating that the chosen values provide a stable representation of clustering behavior. The final chosen values are similar to those from Augenstein et al. (2024). A cluster is defined here as a group of at least three PHTs. An example of PHTs representing the three categories *single*, *clustered*, and *long* is shown in Figure 3.6 for the period 22-29 July 2016. It illustrates that *single* PHTs are the most frequent category, while *long* PHTs occur least often, consistent with the results presented in subsection 4.1.4.

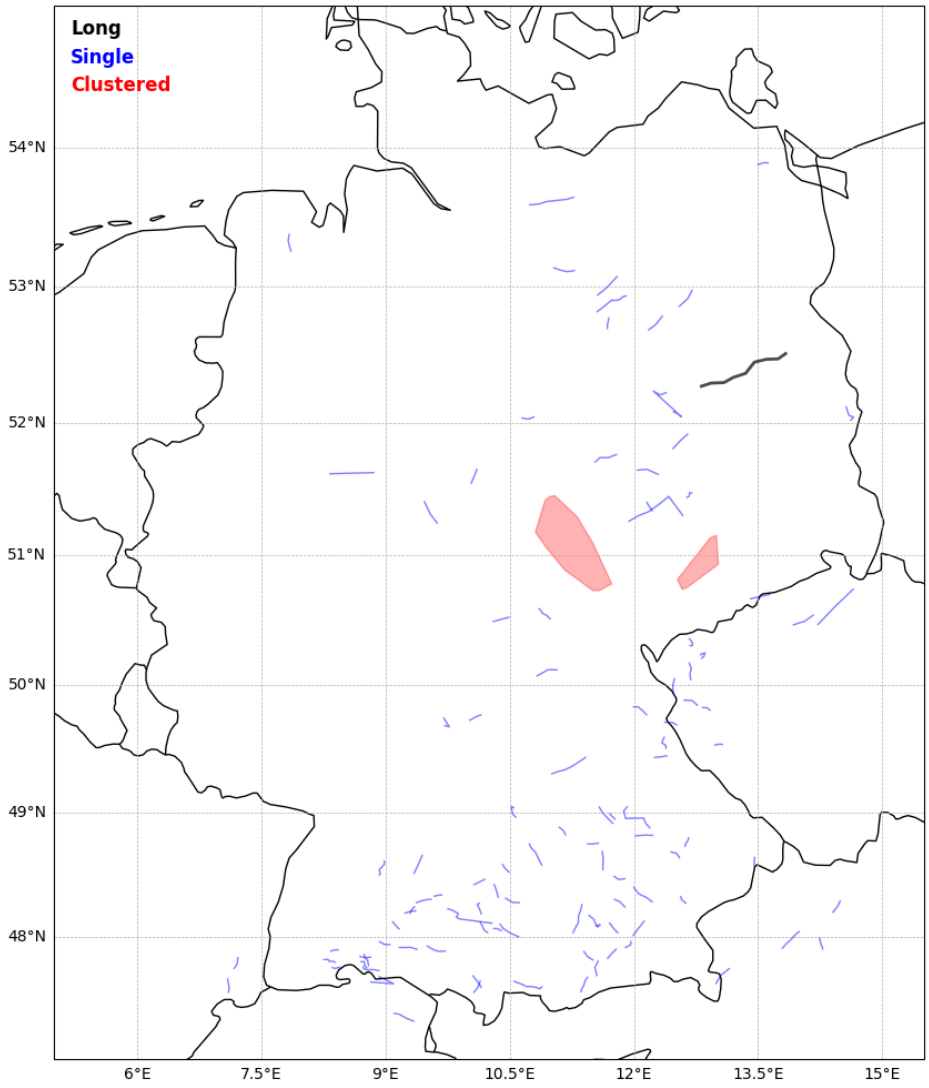

Figure 3.6: Example of a *single* PHT (blue), a *clustered* PHT (red; more than three PHTs), and a *long* PHT (black; longer than seven time steps), categorized using ST-DBSCAN, for the period 22–29 July 2016.

3.2.3. Assignment of environmental conditions to PHTs

The analysis focuses on the pre-convective environment to assess the environmental conditions associated with radar-detected PHTs, as this stage strongly influences storm initiation and intensity. For each PHT, the timestamp and coordinates of the first track point are used to identify the nearest grid point in the ERA5 dataset and the corresponding model timestep. To avoid contamination by conditions during active convection, two additional steps are performed: the timestep is rounded down to the previous full hour, and convective precipitation is checked for. If more than 1 mm of convective precipitation had already occurred

within the preceding hour, the previous timestep is selected instead. These adjustments ensure that the chosen parameters represent the environment prior to storm development rather than during its mature phase. A similar procedure is applied to the atmospheric aerosol data, which has a coarser temporal resolution of three hours. In this case, the rounded-down timestep is used in all instances because it provides the best approximation of pre-convective conditions given the available data. The resulting datasets contain one representative value for each parameter group (convective conditions and aerosols) for each PHT. These values serve as proxies for the thermodynamic and microphysical environments that influence hail and lightning formation.

To determine if the differences between the lightning intensity classes are statistically significant, two hypothesis tests are performed at a significance level of $\alpha = 0.05$. The first test compares the low- and high-intensity classes. Hypothesis testing provides a formal framework for determining whether observed differences are likely due to random variation or represent a true effect. First, Student's t-test (see Student, 1908) is employed; this test assumes a Gaussian sampling distribution. Second, the Mann–Whitney U test (Mann and Whitney, 1947), which makes no assumptions about the underlying distribution, is used. Since the exact distribution of the dataset is unknown, variables are selected such that both tests consistently indicate statistical significance.

4. Results

This chapter presents the results of the analysis of lightning characteristics along radar-detected PHTs over Germany and adjacent regions. In the first part, the spatial and temporal distribution of lightning occurrences along PHTs is examined, with a focus on differences related to track lifetime, year, and region, as well as the clustering behavior of the tracks. The second part explores the environmental conditions associated with these PHTs, described by convective and atmospheric aerosol parameters, to identify potential explanations for the patterns observed in the first part.
In the following analysis, all lightning-related results refer exclusively to lightning strikes associated with radar-detected PHTs.

4.1. Spatial and temporal distribution of lightning along PHTs

In total, 17,099 PHTs were identified using the TRACE3D algorithm (see section 3.1.2). Between 2005 and 2023, the number of PHTs within the study area ranged from 605 to 1224 per year (Figure 4.1). Despite interannual variability, there is no trend in the occurrence of PHTs. Related to the PHTs 2,357,789 lightning strikes are detected. As expected from the theoretical considerations in section 2.3.2, the majority of lightning strikes are negatively charged (92.7%), with the remainder being positively charged (not shown).
Figure 4.2 shows the monthly distribution of lightning related to PHTs for the different years in the study period. The monthly sum in 4.2(a) generally shows maximums of different magnitudes of lightning strikes in June and July, which aligns with the results of Punge and Kunz (2016). Later years in the study period tend to have fewer total lightning per month, with less pronounced peaks and a more even seasonal distribution. The seasonal spread is defined as the difference between the months with the highest and lowest lightning strike counts. In this context, 2022 shows the smallest seasonal spread with 17,408 strikes, whereas 2015 exhibits the largest with 100,565 strikes. Overall, the years 2022, 2023, 2019, and 2018 display the least variability, while 2015, 2006, 2007, and 2009 show the greatest

seasonal spread. The following sections discuss possible reasons for the decrease in detail. Figure 4.2(b) shows the monthly mean of the average lightning strike amount per PHT. This average is calculated by dividing the total lightning some of the track by the track duration (see also subsection 4.1.2). Similar patterns are evident again, and the low seasonal variability at the end of the study period is clearer. The high lightning strike amounts in April and September may be due to the averaging over a low overall number of PHTs, in which individual extreme events may strongly influence the results.

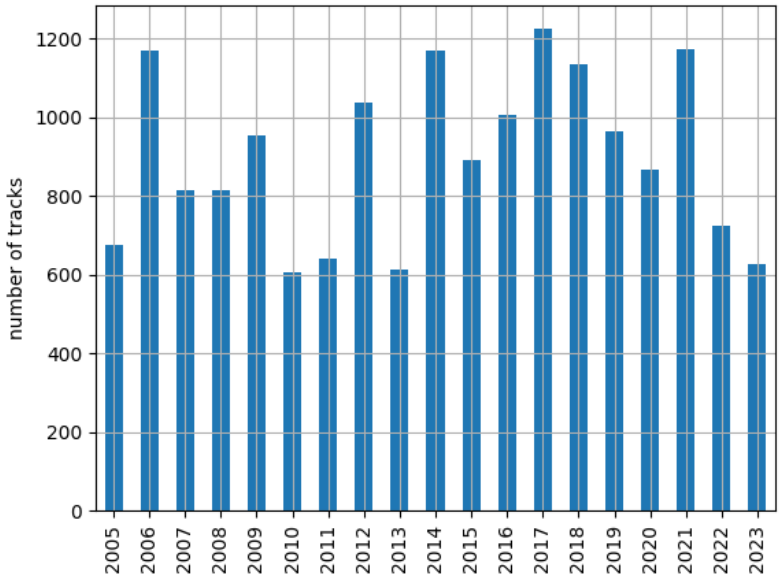

Figure 4.1: Annual number of radar-detected PHTs.

4.1.1. Lightning during lifecycle of PHTs

Based on the design of the TRACE3D algorithm, the minimum PHT duration is three time steps, corresponding to approximately 45 min. There is no upper limit for track duration, the longest track comprises 36 time steps. Tracks comprising three time steps are most frequent (8091 cases), while the number of longer tracks decreases exponentially as duration increases (Figure 4.3).

To analyze lightning occurrence in relation to PHT lifetimes, the tracks are grouped by their duration. For each group, the average number of lightning strikes per time step is calculated. The number of lightning strikes in each of the time steps is averaged across all tracks of a specific group.

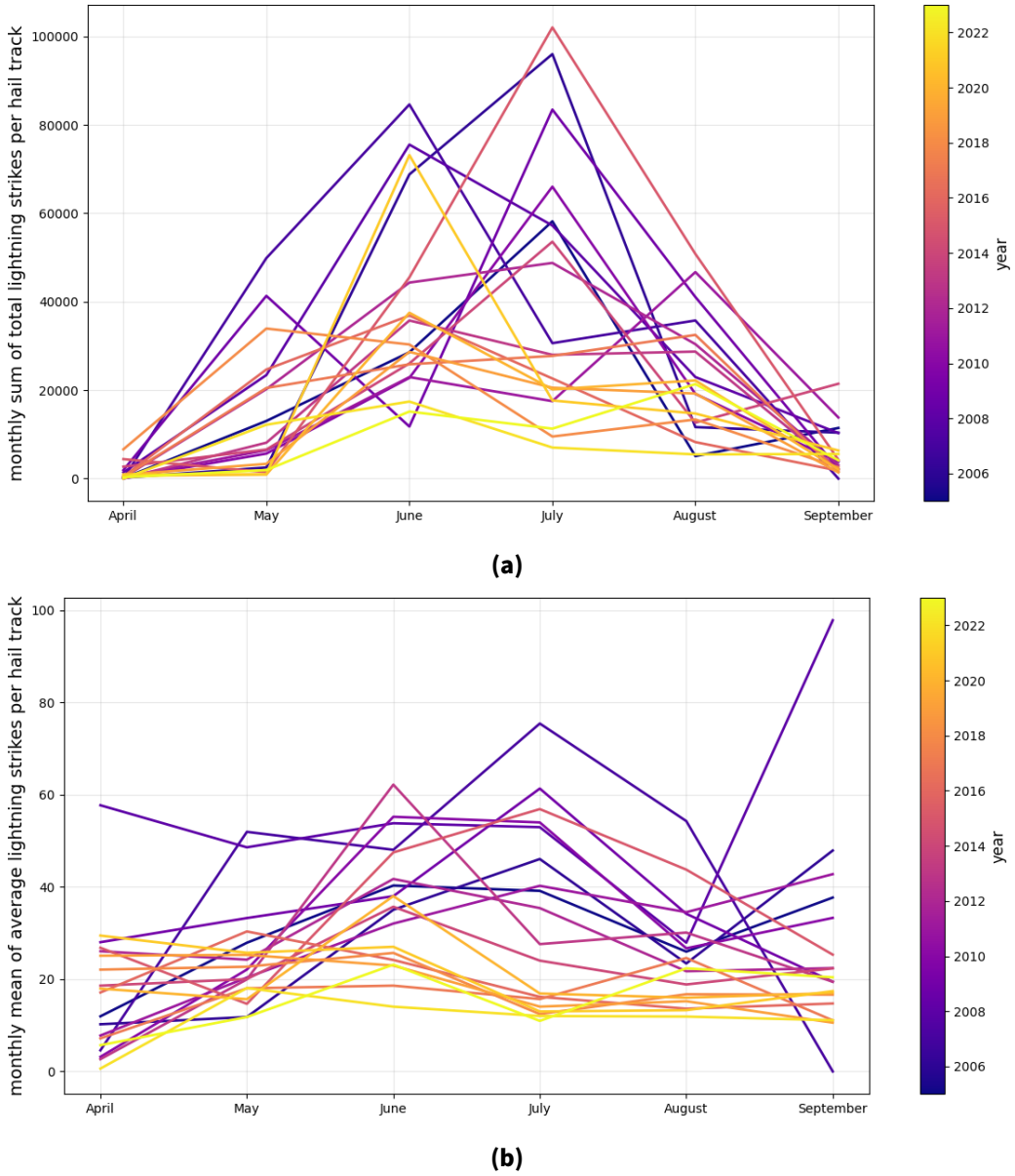

Figure 4.2: Monthly distribution of lightning related to PHTs per year. (a) Monthly sum and (b) monthly mean of average lightning strike amounts per PHT (total amount of lightning strikes divided by track duration; see also subsection 4.1.2).

Selected results are shown in Figure 4.4, while the full distribution of PHT lifetimes and their corresponding lightning occurrence is presented in the Appendix A Figure A.1. The left panel shows results for PHTs with a duration of five time steps, which are representative of shorter PHTs. Conversely, the right panel displays results for tracks with a duration of ten time steps, illustrating the behavior of longer-lived PHTs. However, as track duration increases, such events become less frequent, and the corresponding statistical analyses become less reliable.

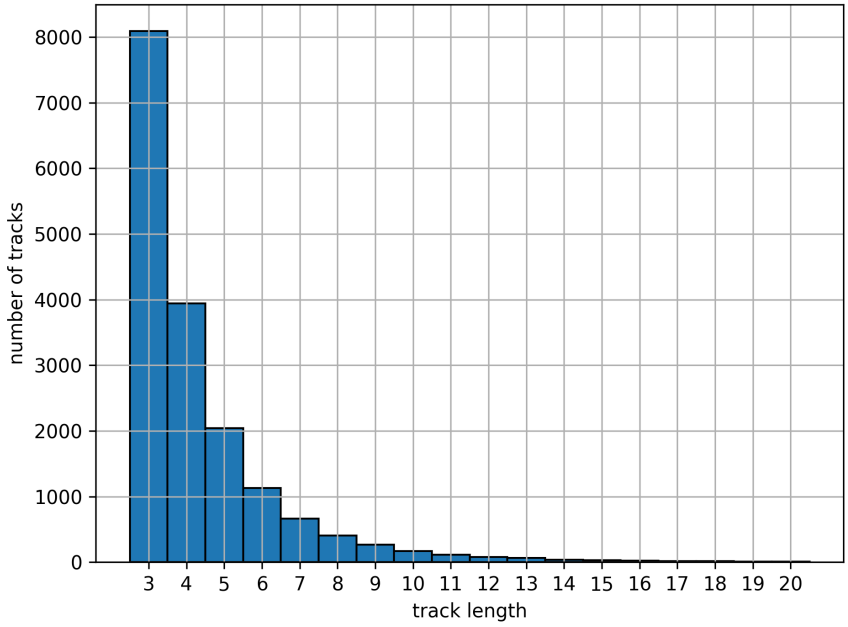

Figure 4.3: Distribution of PHTs by duration for the analyzed dataset. The minimum duration is three time steps (45 min), and the longest PHT comprises 36 time steps. The right end of the distribution (tracks longer than 20 time steps) was omitted for clarity.

In general, the number of lightning strikes increases during the lifetime of PHTs, reaching a peak before decreasing again towards the end. Shorter PHTs, as represented on the left, exhibit a single peak in lightning activity, whereas longer tracks tend to show two distinct peaks. Although the uncertainties, expressed as the 16th–84th percentile range (this corresponds to the standard deviation in case of a normal distribution), are relatively large, they generally follow the same pattern as the median values. Additionally, longer PHTs are associated with higher average lightning counts per time step.

4.1.2. Annual behavior of lightning along PHTs

Despite interannual variability, a negative trend in lightning activity is apparent, with generally higher strike counts in the early years compared to later years (Figure 4.5). This trend is quantified using a linear regression (see Figure 4.5):

$$f(t) = -6260.55 \cdot t + 12{,}732{,}850.69 \ , \tag{4.1}$$

where the slope indicates an average decrease of 6,260.55 lightning strikes per year t. The intercept has no physical meaning, as it corresponds to a mathematical extrapolation to

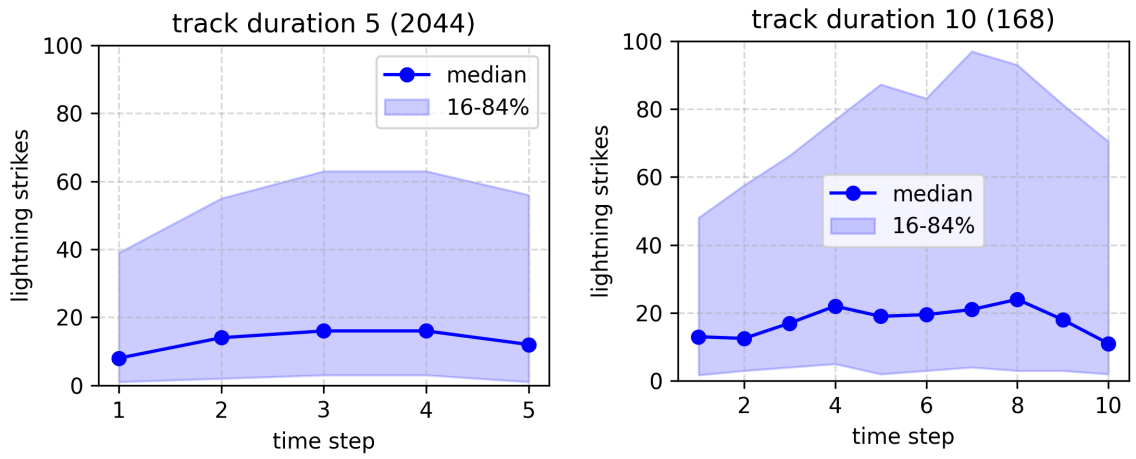

Figure 4.4: Average number of lightning strikes per time step along radar-detected PHTs of different lifetimes. Shown are two representative examples for shorter and longer tracks. The solid lines indicate the median number of lightning strikes per time step, while the shaded areas represent the 16th-84th percentile range across all tracks within each group. Numbers in parentheses denote the total number of PHTs within this specific group.

year $t = 0$, which lies far outside the observational period. The 95% confidence interval (CI) quantifies the uncertainty of the estimated trend and indicates the range within which the true underlying trend would be expected to fall in 95% of repeated samples.
A pronounced peak occurred in 2015 with 208,422 lightning strikes, whereas 2022 recorded the lowest total with only 47,629 strikes. The years with the fewest strikes are 2022, 2023, 2019, and 2020, while 2006, 2008, 2007, and 2015 represent the years with the highest strike counts.
This raises the question of whether this trend is caused by a decrease in the number of convective storms, or by a reduced number of lightning strikes per PHT.

To further analyze this trend, the average number of lightning strikes per PHT is calculated. For this, the total amount of lightning strikes during the whole lifetime of the PHT is divided by the number of time steps of this PHT. PHTs are then grouped into categories based on their average lightning activity, ranging from no lightning to extreme lightning intensity. The grouping is performed using percentile intervals of 15. To ensure that the first category includes all PHTs with an average lightning strike amount below 1, it covers percentiles below 5. A constant percentile step of 15 is applied to facilitate comparison across categories. To align with the lowest category, the highest lightning intensity class includes all PHTs with a percentile of 95 or above. The corresponding percentile groups, their associated lightning strike counts, and the number of PHTs within each group are presented in Table 4.1.

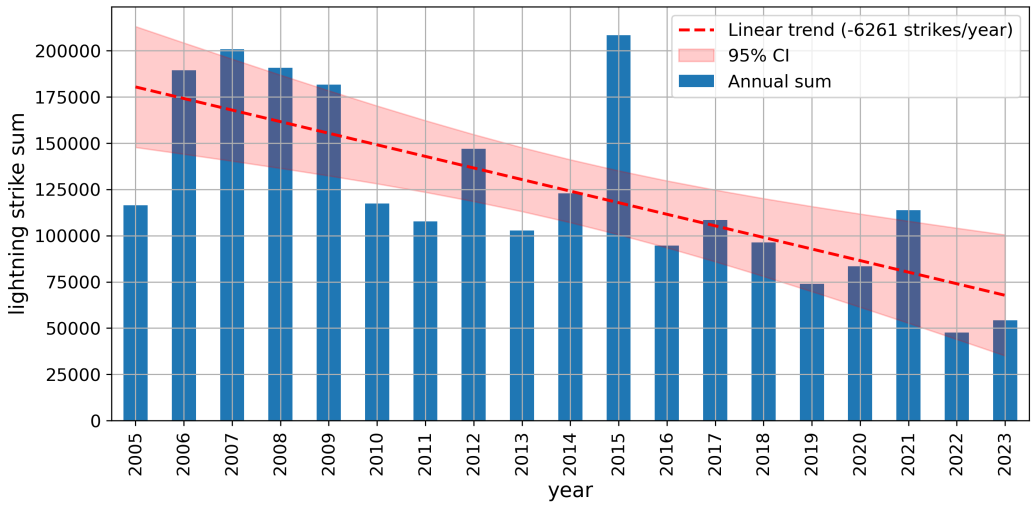

Figure 4.5: Annual total number of lightning strikes associated with radar-detected PHTs. The red dashed line shows a linear regression over the period 2005-2023 The dashed line indicates the linear trend, shading denotes the 95% confidence interval (CI), indicating an average decrease of 6,261 lightning strikes per year.

For example, a PHT that recorded a total of 21 lightning strikes over three time steps would be classified in the 20–35% percentile group, corresponding to an average of 7 strikes per timestep (see Table 4.1).

Table 4.1: Overview of identified percentile groups of the average number of lightning strikes per PHT.

percentile group	lightning strikes	number of PHTs
<5%	0 - 0.65	795
5-20%	0.66 - 3.60	2567
20-35%	3.66 - 7.73	2603
35-50%	7.75 - 13.60	2533
50-65%	13.67 - 23.63	2598
65-80%	23.66 - 43.25	2570
80-95%	43.33 - 111.08	2576
≥95%	111.25 - 882.33	857

For each year, the number of PHTs within each lightning intensity group is determined and then normalized by the total number of PHTs that year. Figure 4.6 shows the resulting distribution of PHTs by average lightning number per track, with the (a) cumulative plot and (b) the line plot highlighting different aspects of the data. The percentile colorbar in this plot is applied throughout the thesis to maintain consistency. By definition, each lightning intensity category should have a frequency of 15%, with the extreme categories (<5% and >95%) having a frequency of 5%, respectively.

Figure 4.6 indicate, despite some interannual variability, different trend directions over the study period. The proportion of lightning-intense PHTs (high percentile groups) has decreased, while the fraction of tracks with low lightning activity has increased. PHTs of medium lightning intensity show no distinct trend. Additionally, the extreme categories of both low and high lightning intensities, show a opposite behavior, an increase in one results in a decrease of the other. This trend is quantified using linear regression for the 5–20% and 80–95% percentile groups (see Figure 4.6):

$$f(t)_{5-20\%} = 0.0069 \cdot t - 13.69 \ , \tag{4.2}$$

$$f(t)_{80-95\%} = -0.0095 \cdot t + 19.32 \ , \tag{4.3}$$

where the slope indicates an average increase in frequency of 0.0069 per year t for the 5–20% percentile group and an average decrease of -0.0095 per year for the 80–95% percentile group. The intercept has no physical meaning, as it corresponds to a mathematical extrapolation to year $t = 0$, which lies far outside the observational period.
The peak in the >95% percentile for 2015 is clearly visible in both plots.
One possible reason for this trend may be the reduction in storm intensity due to less favorable environmental conditions for convection at the end of the study period.

4.1.3. Spatial differences

This section focuses on the spatial analysis of lightning occurrence with the aim of detecting potential differences. Therefore, the study area is divided into a grid of 36×36 points ($0.19° \times 0.33°$) to enable a more detailed analysis of the spatial distribution of lightning occurrence. For each grid point the total number of tracks are calculated and shown in Figure 4.7. At first glance, the maximum in the southern part of Germany in the pre-alpine region and the Swabian Alb is visible.

The proportion of PHTs within specific lightning intensity categories (percentile groups) is calculated for each grid point. This analysis reveals whether certain grid points tend to feature, for example, predominantly lightning-intensive PHTs. Overall, the proportional distribution appears relatively homogeneous across the study period for all lightning intensity categories, except in peripheral regions (Figure 4.8). In these areas, radar coverage is less comprehensive compared to the core region over Germany. Consequently, only a few PHTs are detected there, which leads to disproportionately high shares of individual lightning intensity categories.

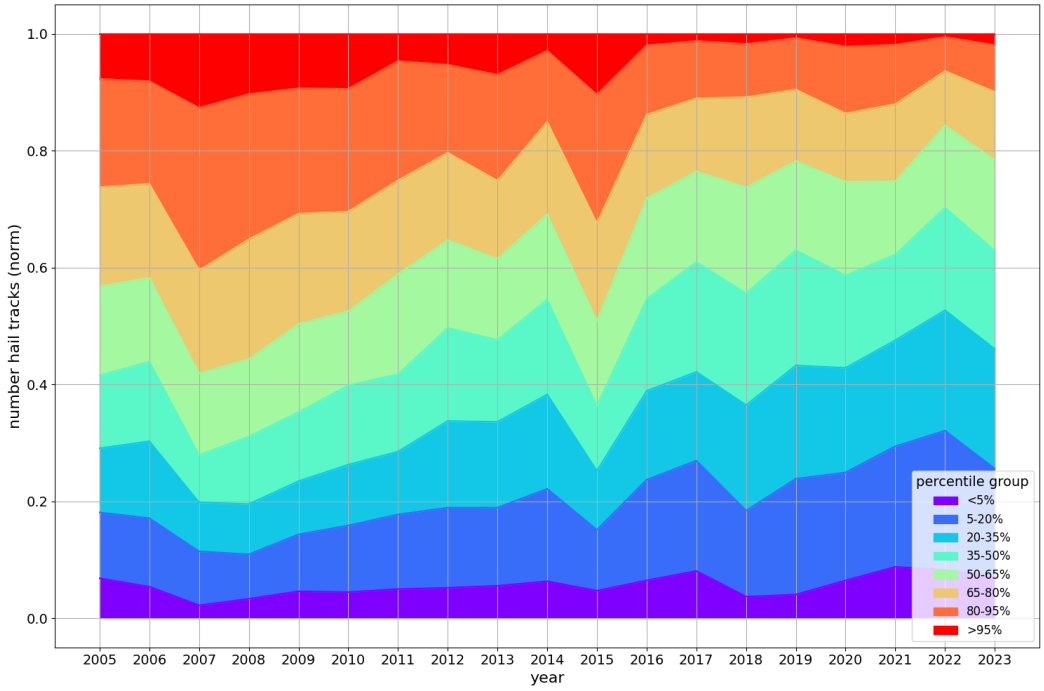

(a)

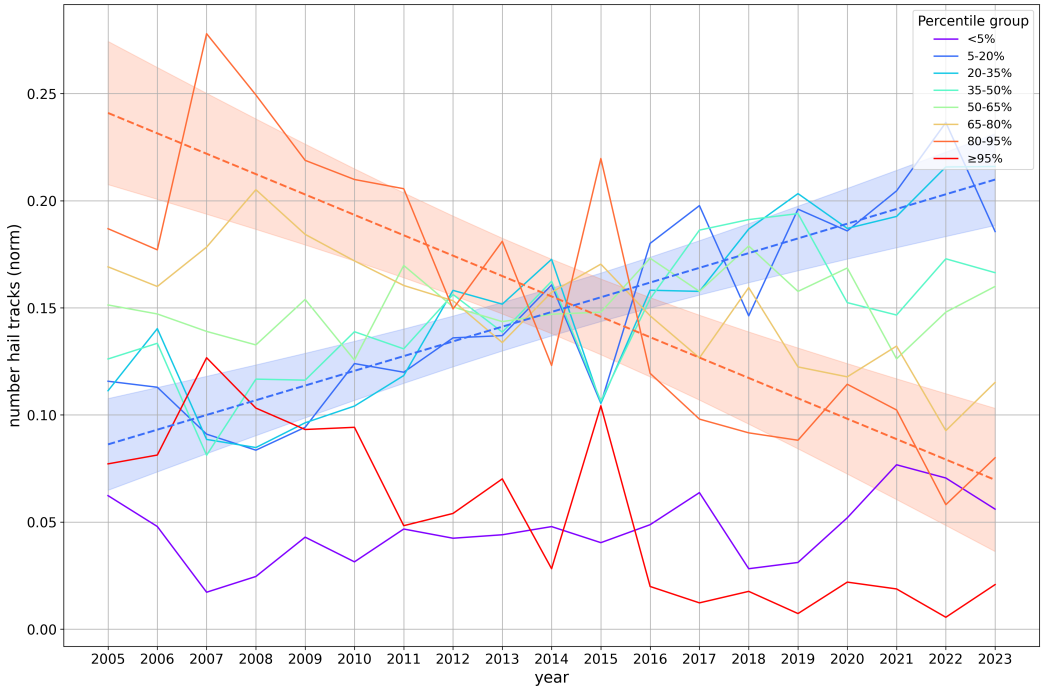

(b)

Figure 4.6: Normalized distribution of radar-detected PHTs by their average number of lightning strikes per track per year. Tracks are grouped into percentile categories based on their average lightning activity and counted per year within each group. Percentile categories use 15% intervals, with the extremes (<5% and >95%) set to 5%. Results are normalized by the total number of tracks per year. (a) Cumulative plot; (b) line plot. The colorbar indicates the percentile groups, applied consistently throughout the analysis. Dashed lines show linear regressions over 2005–2023 for the 5–20% and 80–95% percentile groups. Shaded areas denote the corresponding 95% confidence intervals (CIs). The estimated trends indicate an average increase of 0.0069 per year for the 5–20% group and a decrease of 0.0095 per year for the 80–95% group.

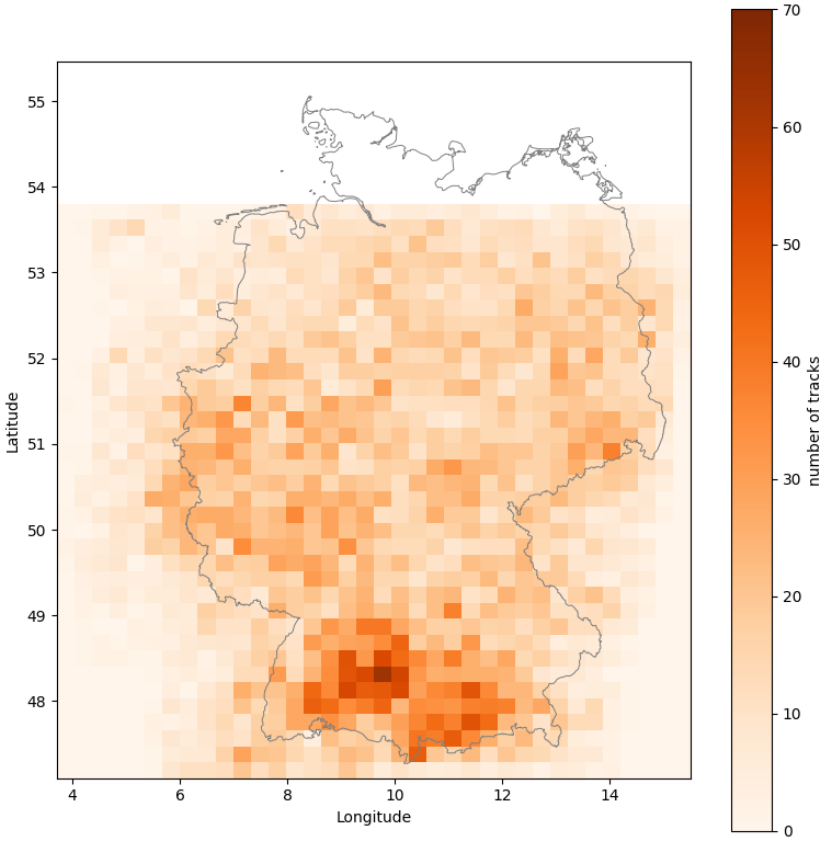

Figure 4.7: Spatial distribution of radar-detected PHTs per grid point accumulated over the 18-year period.

To further investigate potential trends and spatial variations in lightning frequency associated with PHTs, the study area was divided into four equally sized regions, while maintaining a statistically reliable sample size for each region. The regions are defined by their geographical position: North-West (NW), North-East (NE), South-East (SE), and South-West (SW). For each region, the annual number of PHTs within each percentile group (based on the average number of lightning strikes per track) is determined. The distribution of PHTs across regions is uneven (NE: 3764 tracks; NW: 2448; SE: 5894; SW: 4993). At first glance, the southern part of the study area appears considerably more convectively active than the northern part (Figure 4.9). These findings align with those from other studies, such as (Puskeiler et al., 2016). Years with a generally high number of tracks are indicated by reddish colors across all percentile groups. Moreover, the regions show a clear shift over time: from more lightning-intense PHTs at the beginning of the study period (upper right corner) toward less lightning-active tracks toward the end (lower left corner).

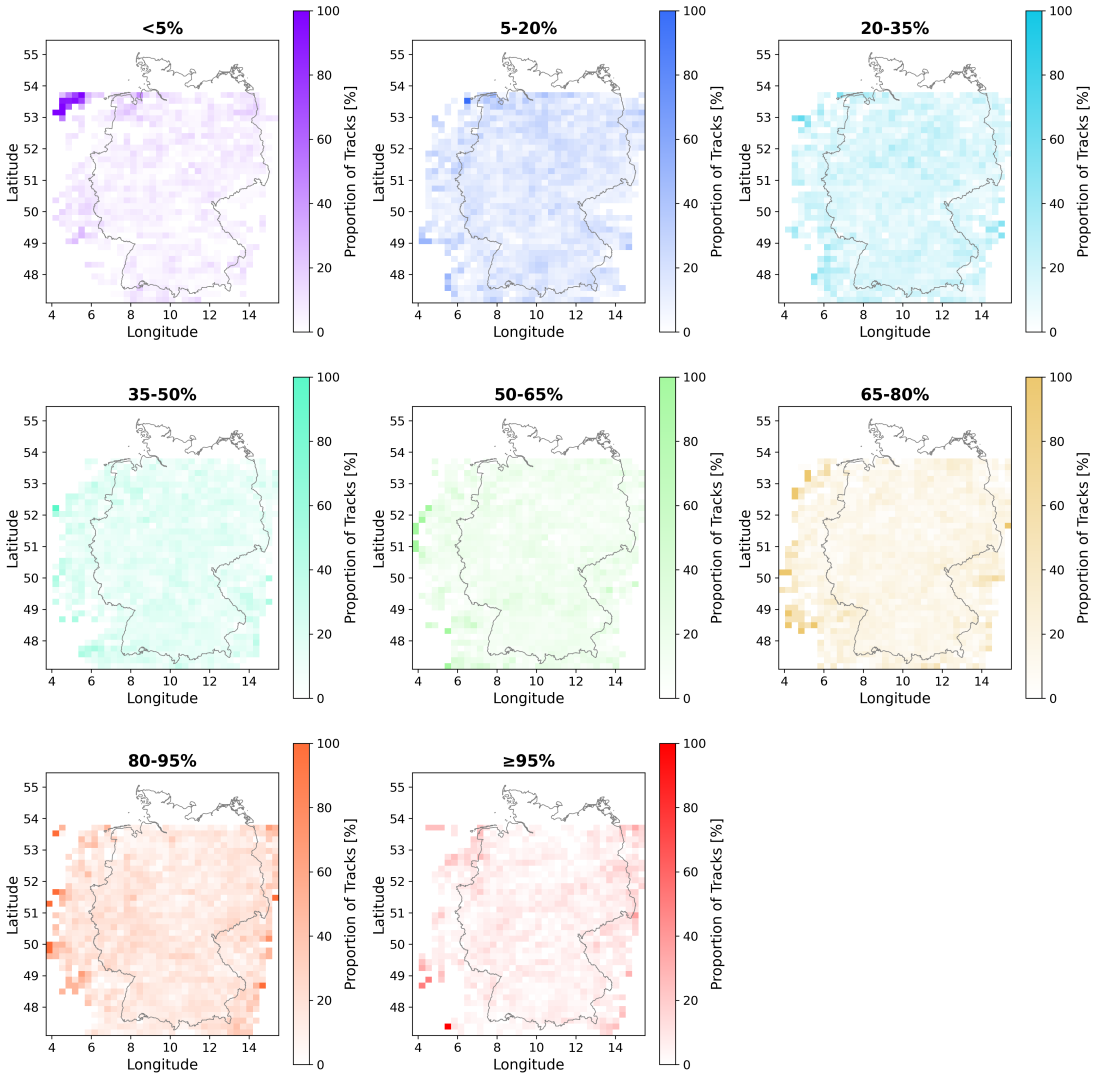

Figure 4.8: Spatial distribution of radar-detected PHTs by average lightning activity per grid point. PHTs are classified into lightning intensity categories based on their average number of lightning strikes per track. For each grid point, the proportion of PHTs within each lightning intensity category is shown. The colorbar indicates the percentile groups, which are applied consistently throughout the analysis.

4.1.4. Clustered PHTs

Previous analyses considered each PHT individually. Here, classifying PHTs as clustered, individual, and long enables the identification of spatial and temporal patterns in severe convective storms. This reveals differences in the organization, lifecycle, and intensity of storms that cannot be captured by analyzing individual PHTs. To enable a comparison between *short* and *long* tracks, as well as between *single* and *clustered* PHTs, the ST-

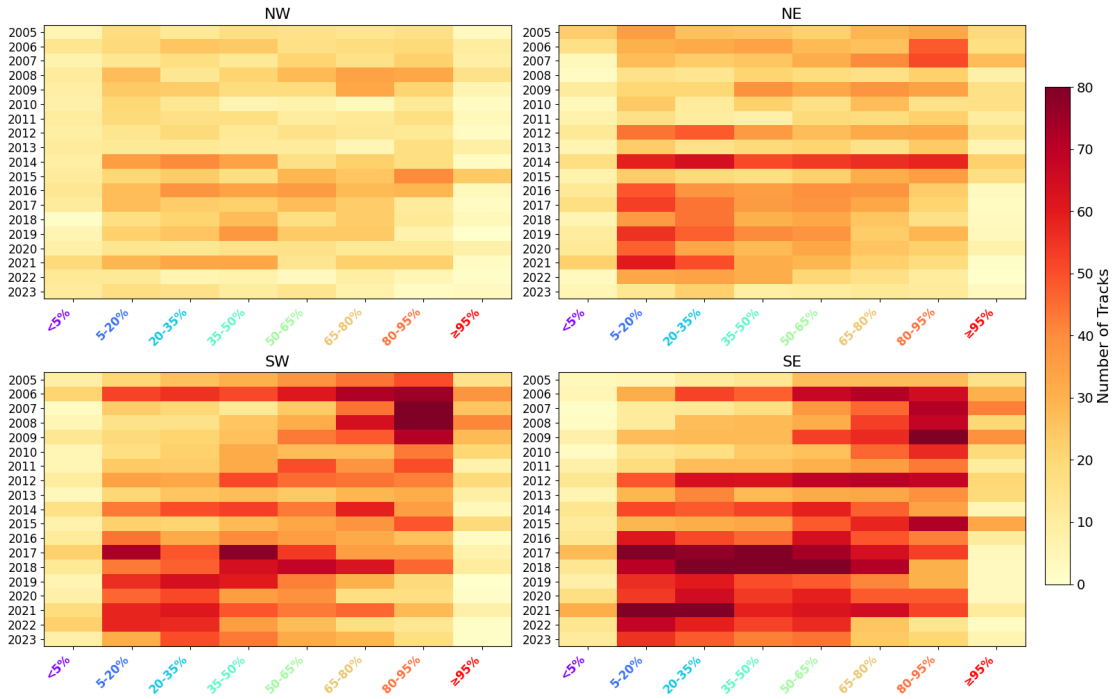

Figure 4.9: Annual distribution of radar-detected PHTs by average lightning activity, separated into four equally sized geographical regions (NW, NE, SE, SW). Tracks are grouped into lightning intensity categories based on their average number of lightning strikes per track. The colorbar of the x-axis indicates the percentile groups, which are applied consistently throughout the analysis.

DBSCAN algorithm was applied to the dataset. In total, 1227 PHTs were classified as *long*, 2347 as *clustered*, and 13525 as *single*. Figure 4.10 (a) shows the average number of lightning strikes per PHT for these three categories. The median values are 12.75 for the *single* category, 16.0 for the *clustered* category, and 22.4 for *long* PHTs. A clear difference between *short* (*single* and *clustered*) and *long* PHTs is evident. Differences between *single* and *clustered* PHTs are less pronounced, although *clustered* tracks tend to exhibit slightly higher lightning activity. Figure 4.10 (b) illustrates the differences of percentiles between *single* and *clustered* PHTs compared to *long* PHTs. For example, a value of seven average lightning strikes per PHT corresponds to the 35th percentile in the *single* category, but to the 16.3rd percentile in the *long* category, resulting in a percentile difference of −18.7. Similar to the previous observation, the difference between *short* and *long* tracks becomes evident, particularly in the medium percentile ranges. Extreme values show smaller differences. Differences between *single* and *clustered* tracks are also apparent, although they are less pronounced than those between *short* and *long* PHTs.

These results indicate that *long* PHTs are associated with higher lightning intensities, regardless of their duration, and that *clustered* PHTs tend to be more intense than *single* PHTs. Consequently, extensive regions with convectively favorable conditions appear to

promote not only a spatial increase in lightning occurrence but also an increase in its intensity.

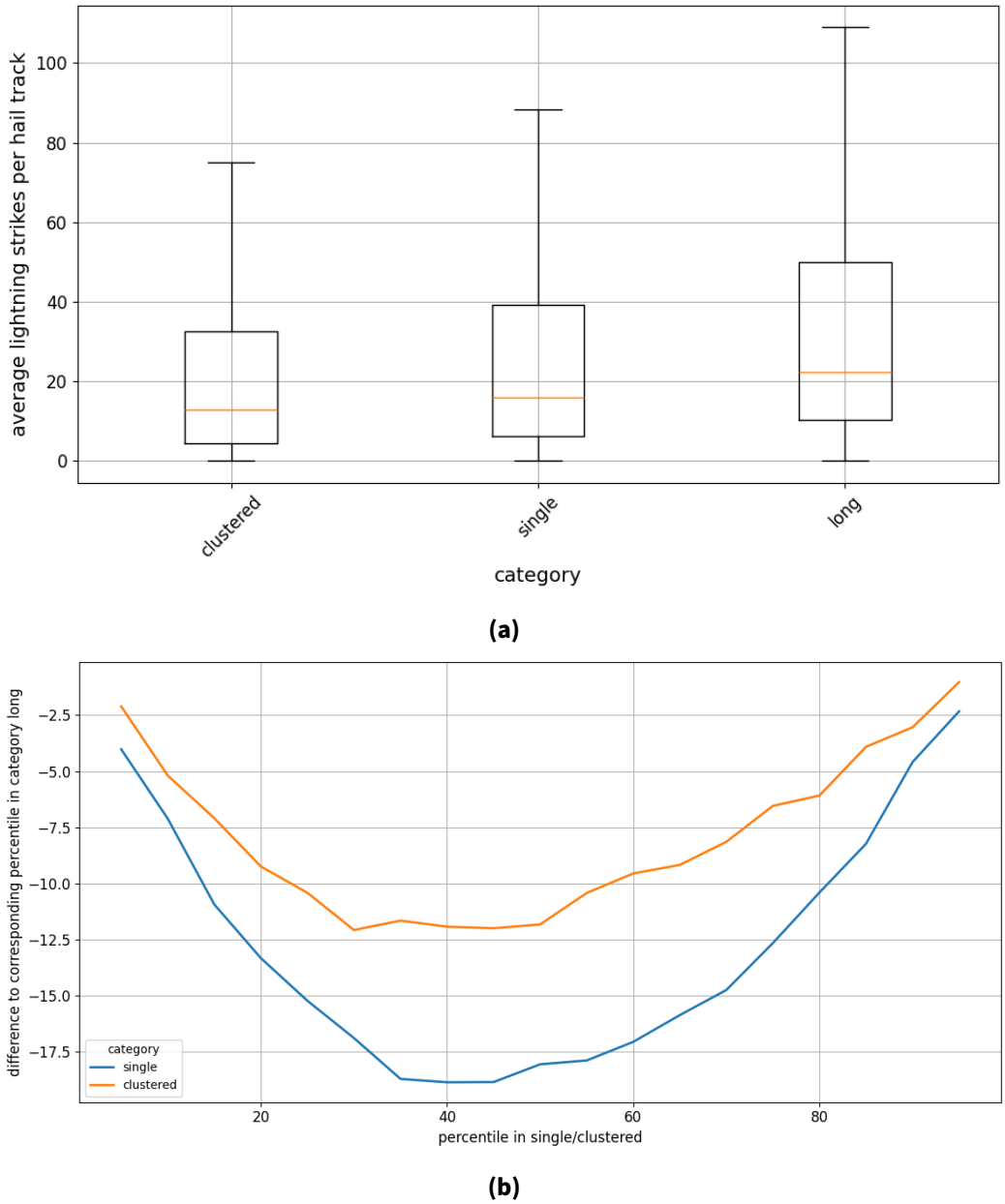

Figure 4.10: a) Distribution of average number of lightning strikes per PHT categorized into *single*, *clustered* and *long* PHTs with ST-DBSCAN. b) Differences of lightning strike percentiles between *single* and *clustered* PHTs compared to *long* PHTs.

4.1.5. Reflectivity core attribution

To gain additional insights into the characteristics of individual PHTs, particularly their intensity, rather than focusing solely on their temporal and spatial occurrence, this analysis considers variables related to the reflectivity cores of the PHTs.
Therefore, a similar analysis to that conducted for the PHTs is applied to the reflectivity core variables, which are related to the intensity of the hailstorm (Figure 4.11). The full distribution of RC lifetimes and their corresponding *RXMax*3 occurrence is presented in the Appendix A Figure A.2. In contrast to lightning activity, *RXMax*3 remains nearly constant over the course of the track lifecycle. This pattern is observed across all analyzed track durations, with no substantial variation between shorter and longer tracks. The relatively sharp uncertainty range of the 16th and 84th percentiles is in stark contrast to the wide uncertainty range of the average lightning strikes per time step (see Figure 4.4).

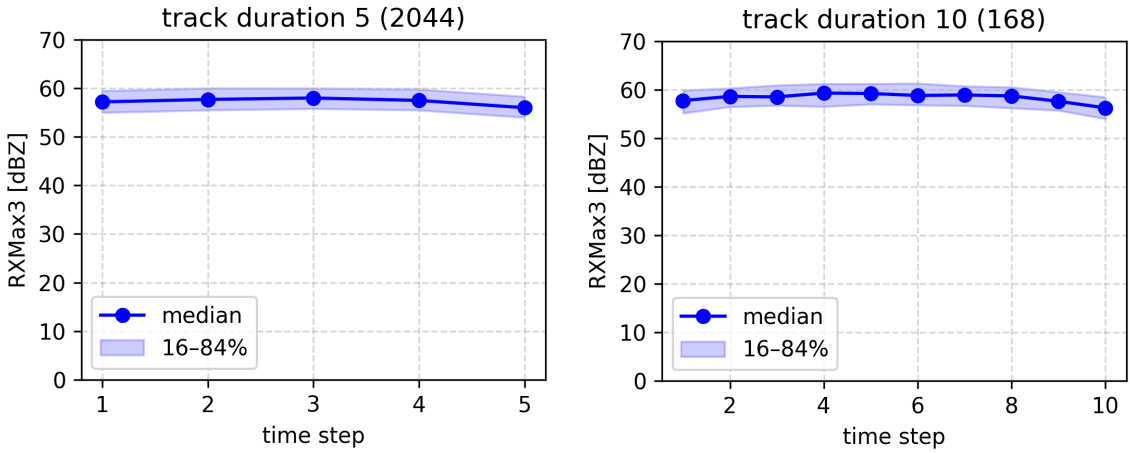

Figure 4.11: Average amount of *RXMax*3 per time step along radar-detected reflectivity cores (RCs) of different lifetimes. Shown are two representative examples for shorter and longer tracks. The solid lines indicate the median of *RXMax*3 per time step, while the shaded areas represent the 16th–84th percentile range across all RCs within each group. Numbers in parentheses denote the total number of RCs within each group.

Analogous to the normalized distribution of annual PHTs by lightning intensity class, Figure 4.12 presents the corresponding distribution for the *RXMax*3 intensity categories. The figure reveals alternating periods characterized by a high proportion of PHTs with strong *RXMax*3 intensity and a low proportion of weak intensity, and vice versa. In recent years, PHTs with high *RXMax*3 intensity have been particularly dominant, despite overall

interannual variability. This trend is quantified using linear regression for the 5–20% and 80–95% percentile groups (see Figure 4.6):

$$f(t)_{5-20\%} = -0.0078 \cdot t + 15.94 \,, \tag{4.4}$$

$$f(t)_{80-95\%} = 0.0111 \cdot t - 22.23 \,, \tag{4.5}$$

where the slope indicates an average decrease in frequency of -0.0078 per year t for the 5–20% percentile group and an average increase of 0.0111 per year for the 80–95% percentile group. The intercept has no physical meaning, as it corresponds to a mathematical extrapolation to year $t = 0$, which lies far outside the observational period.

To describe the relationship between the lightning intensity categories and the $RXMax3$ intensity classes further, Figure 4.13 shows the number of PHTs corresponding to each combined percentile group. The highest frequencies occur in the 5–20% lightning intensity class combined with precipitation intensities of 5–20% and 20–35%, with counts of 447 and 471 tracks, respectively. Enhanced counts are also observed for moderate precipitation intensities (20–65%) paired with low to moderate lightning intensities (5–35%). In contrast, combinations involving extreme percentiles (>95%) for either variable are rare, as indicated by the lighter shading and lower counts in these bins.

Additionally, lightning strikes are not only considered within a fixed selection radius of 15 km, but also within the dynamic areas defined by RC_{46} and RC_{55}. As described in section 3.1.2, these areas vary from time step to time step and from PHT to PHT. On average, the selection areas are as follows: $A_{46} = 114.6\,\mathrm{km}^2$, $A_{55} = 24.8\,\mathrm{km}^2$, and $A_{15km} = 706.9\,\mathrm{km}^2$. Figure 4.14 shows the average number of lightning strikes per time step within RC_{46} ($LSinA46$) and RC_{55} ($LSinA55$) for PHTs of different durations. The results are similar to those shown in Figure 4.4, although the total number of lightning strikes is lower. Among the three selection areas, RC_{55} yields the lowest average lightning counts.
These results align with the findings of Changnon (1992), which indicate that lightning tends to occur in regions adjacent to hail streaks. This also supports the use of a constant selection radius, regardless of the spatial extent of the PHT.

As mentioned in section 3.1.1, the considered lightning strikes are CG only. Despite the carefully defined spatial and temporal selection of lightning strikes along radar-detected PHTs, 440 PHTs in the dataset exhibit an average of fewer than one lightning strike per track. Their spatial distribution is shown in Figure 4.8, represented as the lightning intensity category < 5%. As previously described, no specific region shows a notably high frequency

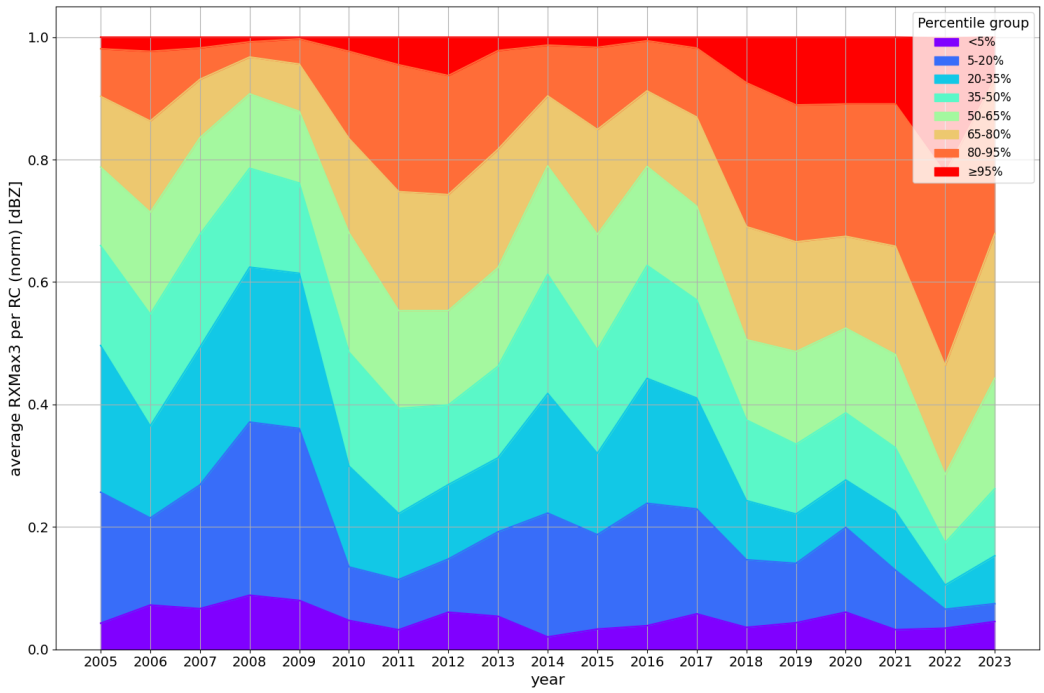

(a)

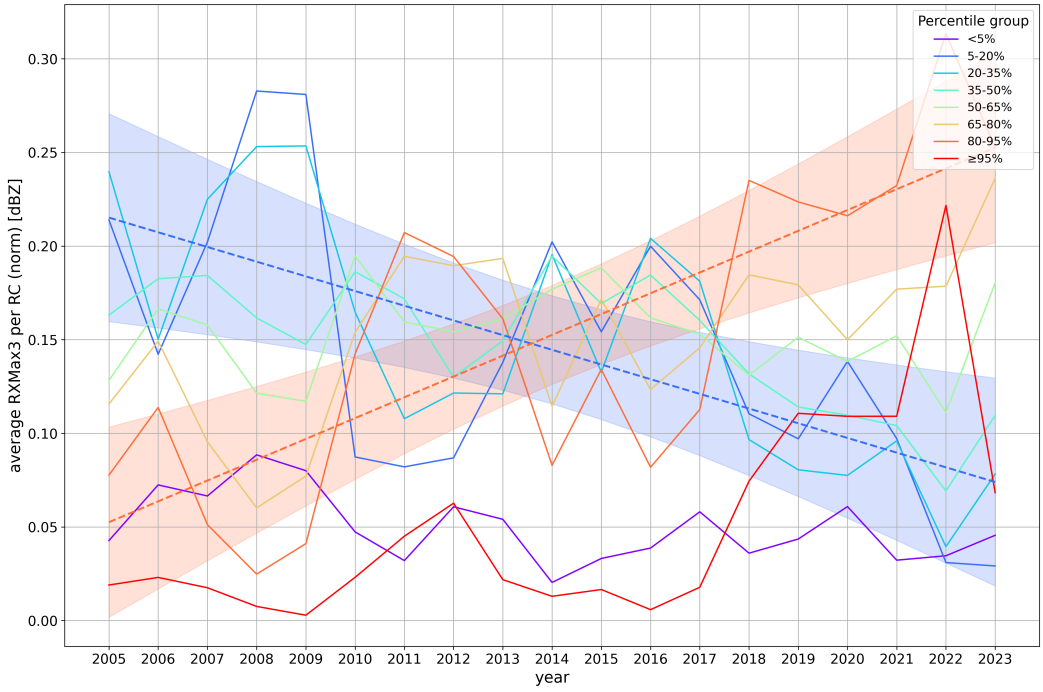

(b)

Figure 4.12: Normalized distribution of radar-detected reflectivity cores by their average number of lightning strikes per track per year. Reflectivity cores are grouped into percentile categories based on their average lightning activity and counted per year within each group. Percentile categories use 15% intervals, with the extremes (<5% and >95%) set to 5%. Results are normalized by the total number of reflectivity cores per year. (a) Cumulative plot; (b) line plot. The colorbar indicates the percentile groups, applied consistently throughout the analysis. Dashed lines show linear regressions over 2005–2023 for the 5–20% and 80–95% percentile groups. Shaded areas denote the corresponding 95% confidence intervals (CIs). The estimated trends indicate an average decrease of -0.0078 per year for the 5–20% group and an increase of 0.0111 per year for the 80–95% group.

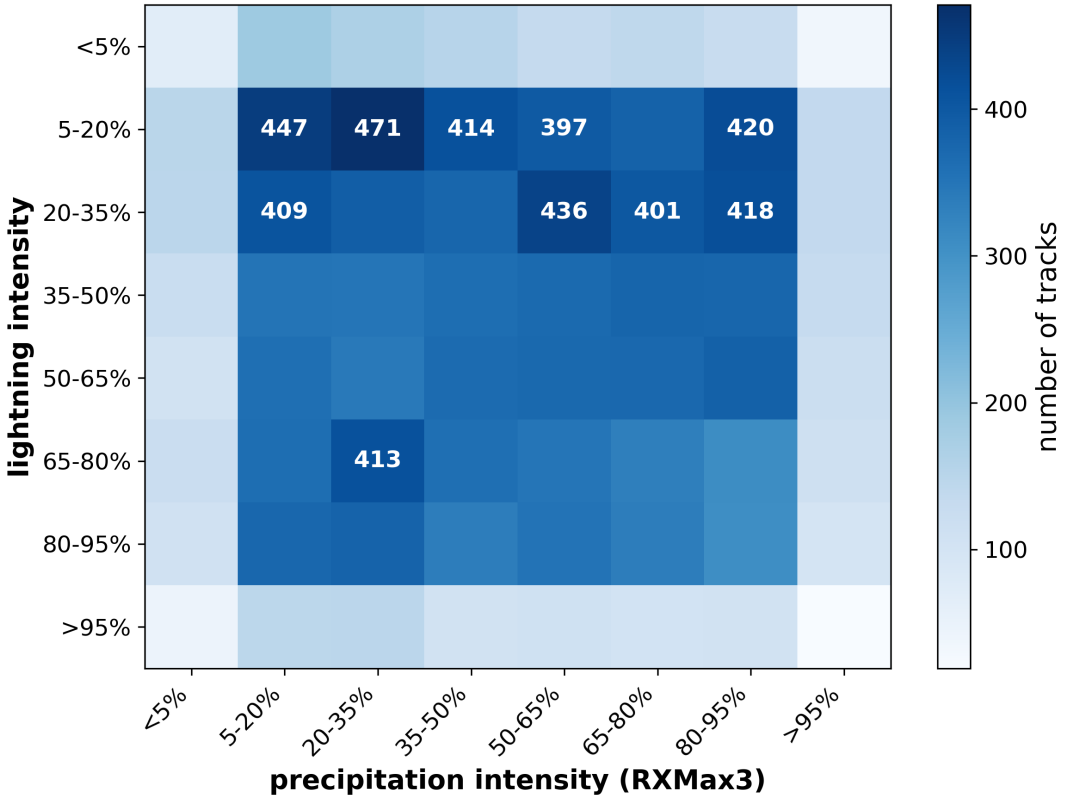

Figure 4.13: Cross-tabulation of lightning and precipitation intensity classes (based on *RXMax*3). The ten most frequent combinations are indicated by white numbers within the corresponding cells.

of such cases. Figure 4.15 displays the annual number of PHTs without lightning strikes for the fixed 15 km radius as well as for RC_{46} and RC_{55}. The RC_{46}-based selection includes a total of 2123 radar cells without any lightning strikes, whereas the RC_{55}-based selection comprises 5580 such cases. The maximum proportion of PHTs without lightning strikes was observed for the 15 km selection radius in 2005 (13.2%), for RC_{46} in 2021 (16.2%), and for RC_{55} in 2022 (37.8%). While no clear trend is observed in absolute numbers, the number of PHTs without lightning is closely related to the total number of PHTs per year, particularly in the RC-based results. The normalized values indicate an increase in the proportion of lightning-free PHTs when using the RC-based selection areas. In contrast, the analysis using the fixed 15 km radius shows no such trend and results in significantly fewer PHTs without associated lightning strikes for each year, except 2005.

However, to analyze this further, CC and IC lightning strikes were included exemplarily for the year 2016 (not shown). This addition reduced the number of PHTs without any associated lightning from 54 to 17. In general, the total number of lightning strikes associated to PHTs increased by 583.6% to 552533.

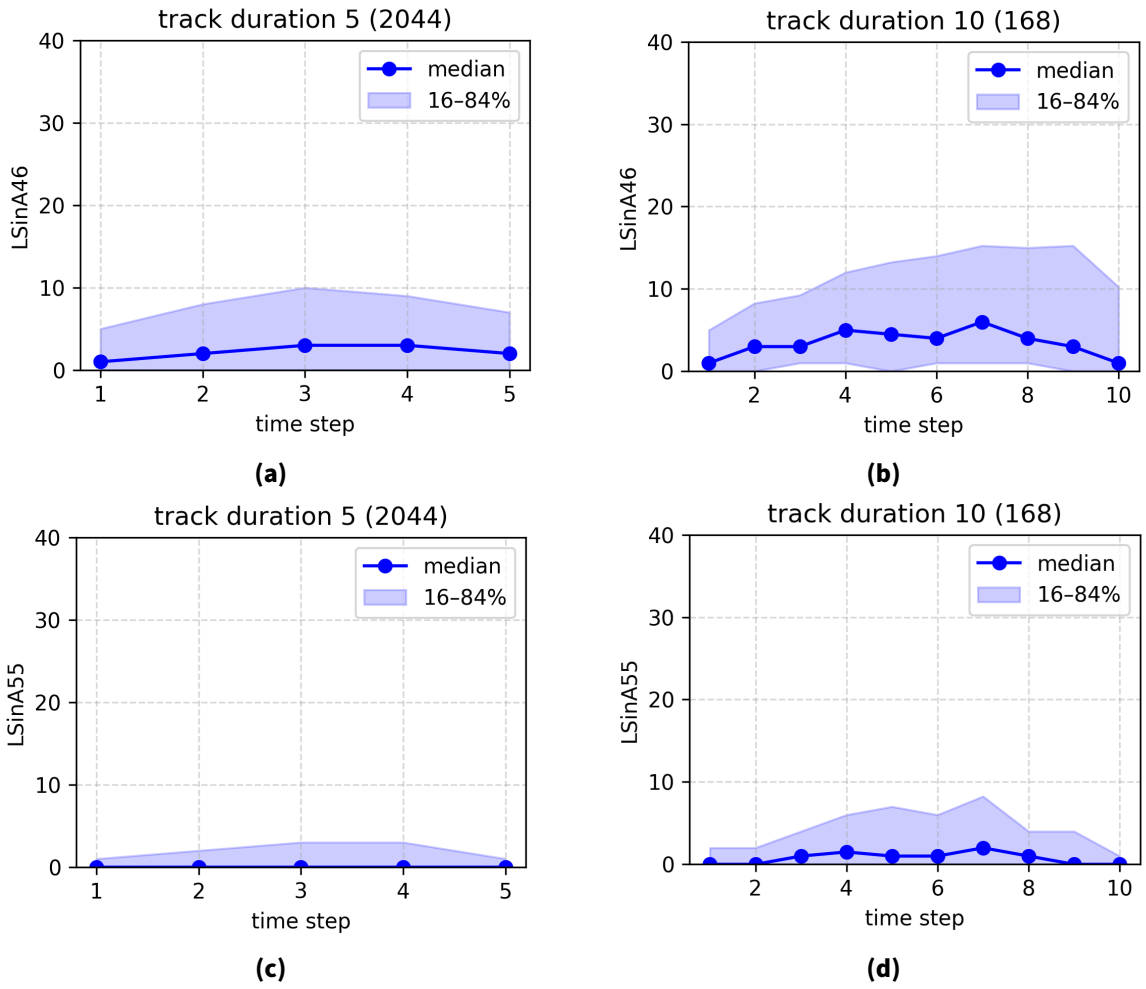

Figure 4.14: Average amount of lightning strikes per time step along radar-detected reflectivity cores (RCs) of different lifetimes and different reflectivities. (a) and (b): RC_{46}; (c) and (d): RC_{55}. Shown are two representative examples for shorter and longer tracks. The solid lines indicate the median number of lightning strikes per time step, while the shaded areas represent the 16th–84th percentile range across all RCs within each group. Numbers in parentheses denote the total number of RCs within each group.

4.2. Environmental conditions associated with PHTs

In order to explain the variability in hail and lightning occurrence, it is essential to understand the pre-convective environment. Convective parameters offer insight into the thermodynamic and dynamic conditions that affect storm development and electrification. Similarly, aerosol concentrations influence cloud microphysics and charge separation processes, which can alter lightning activity. Investigating these factors helps identify the drivers behind observed trends, improving the ability to predict severe convective storms in a changing climate.

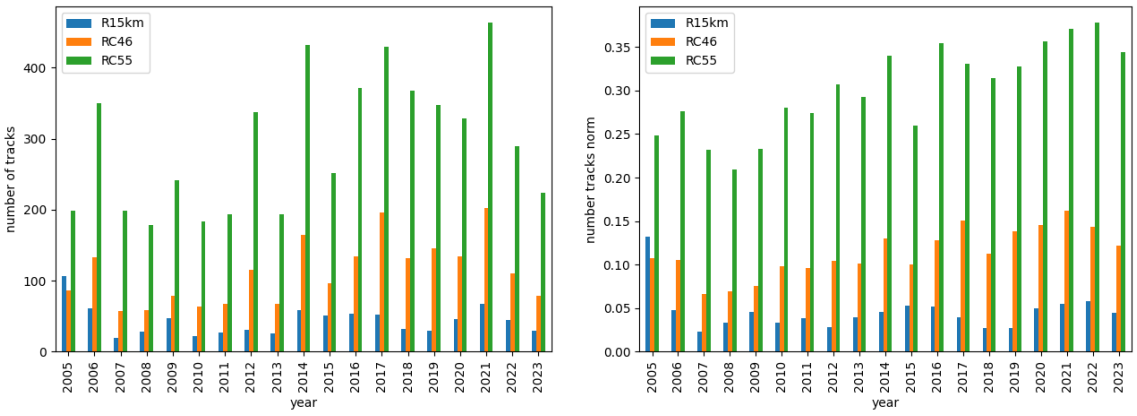

Figure 4.15: Annual distribution of radar-detected PHTs with an average lightning count below one, shown for three datasets: (i) selection within a 15 km radius, (ii) selection based on reflectivity exceeding 46 dBZ (RC_{46}), and (iii) selection based on reflectivity exceeding 55 dBZ (RC_{55}). Panel (a) shows the annual sum, while panel (b) presents the annual sum normalized by the total number of PHTs per year.

4.2.1. Convective parameters

The selection of convective parameters is based on Taszarek et al. (2020) and aims to provide a comprehensive overview of thermodynamic, moisture-related, dynamic, and combined influences on convective environments relevant to the formation of lightning and hail. For theoretical background and definitions, refer to section 2.1.2. PHTs are categorized into percentile groups according to their lightning intensity, as described above. The corresponding pre-convective conditions, represented by the selected parameters for each lightning intensity category, are shown in Figure 4.16. The parameters selected here exhibit the most distinct signals, while additional parameters are presented in Figure A.3. The parameters analyzed include storm-relative helicity (SRH) between 0 and 3 km for left movers (LM) and right movers (RM), denoted as SRH_03km_LM and SRH_03km_RM, respectively. Relative humidity (RH) is considered for two layers: 0–2 km (RH_02) and 2–5 km (RH_25). Bulk shear between 0 and 10 km is labeled as BS_010km, and precipitable water ($PRCP\_WATER$) is given in mm.

Significant differences are observed between the 5–20% (low lightning intensity) and 80–95% (high lightning intensity) percentile groups, confirmed by both the t-test and the Mann–Whitney U test. Percentage-based MU_CIN and ML_CAPE show the greatest differences in medians between the two groups (96.2% and 71.7%, respectively), whereas RH_25 exhibit the smallest differences (4.1%). Parameters such as ML_CAPE, RH_25, $ML\_WMAXSHEAR$, SRH_03km_LM, and $PRCP\_WATER$ and SRH_03km_RM increase

with lightning intensity, while *MU_CIN*, *MU_LI*, *RH*_02, and *BS*_010*km* decrease.
ML_CAPE and *RH*_25 show strong variability within each percentile group. That said, the distributions of all parameters overlap considerably with changing lightning intensity. For example, the value of 1500 J kg^{-1} *ML_CAPE* can be found near all PHTs, regardless of the related amount of lightning strikes.
However, the median value patterns correspond to expectations based on the theoretical concepts presented in subsection 2.1.2.

Looking specifically at the pre-convective environmental parameters related to PHTs over the last 18 years, there is considerable interannual variability but no consistent long-term trend (see Figure 4.17 and Figure A.4). The median of *ML_CAPE* ranges between 552.0 and 818.9 J kg^{-1}, with whisker limits extending up to 3660.1 J kg^{-1}. *MU_CIN* distributions are skewed towards values close to zero, with minimums down to −549.4 J kg^{-1}. *SRH*_03*km_RM* shows the greatest annual variation, with a 126.2% difference between the lowest median in 2012 (-166.0 m^2 s^{-2}) and the highest in 2007 (911.0 m^2 s^{-2}). The smallest differences occur for *RH*_02 (10.1%) and *MU_LI* (-18.5%). For *PRCP_WATER*, the absolute difference between the highest and lowest median is only 4.5 mm, with interquartile ranges from 6.4 mm (2007) to 10.5 mm (2015). RH tends to be higher in the lowest layer (0–2 km), with median values between 0.73 and 0.76 (see Figure A.3), compared to 0.64–0.69 in the 2–5 km layer. LM exhibits negative *SRH* medians (−60.1 to −32.8m^2 s^{-2}), RM tends to have positive median values (62.3 to 78.6 m^2 s^{-2}).
Therefore, the convective parameters do not mirror the temporal behavior of lightning strike frequency within the study period.
The analysis of convective parameters confirms their strong influence on lightning occurrence along PHTs. However, the absence of a clear long-term trend in these parameters suggests that changes in lightning occurrence over the study period are less likely driven by thermodynamic or dynamic factors.

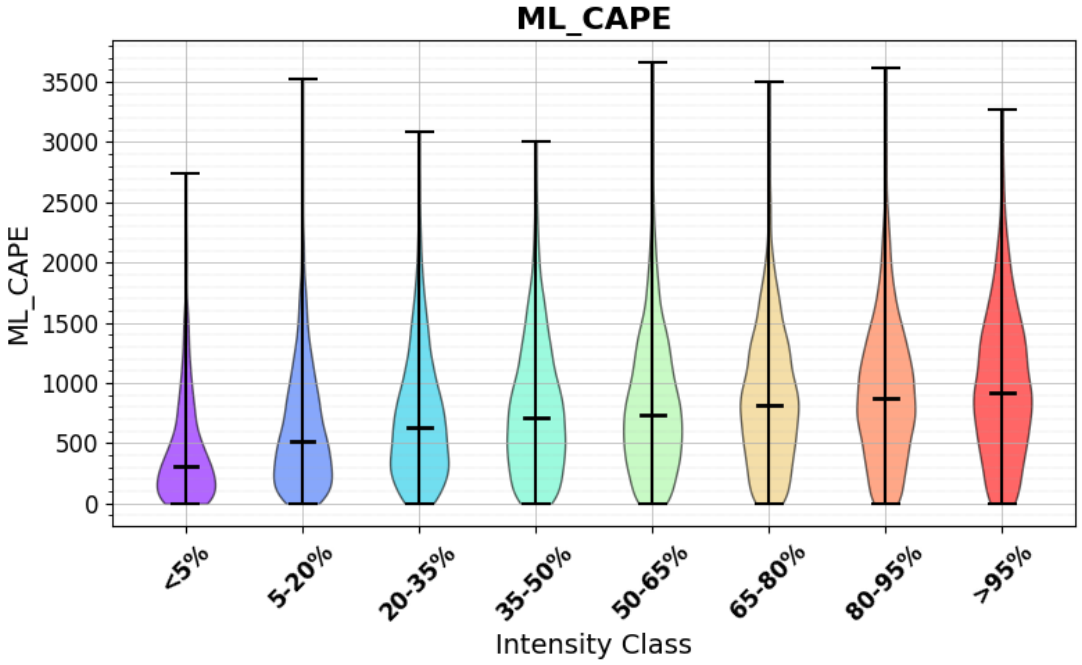

(a) mixed-layer convective available potential energy in [J kg^{-1}]

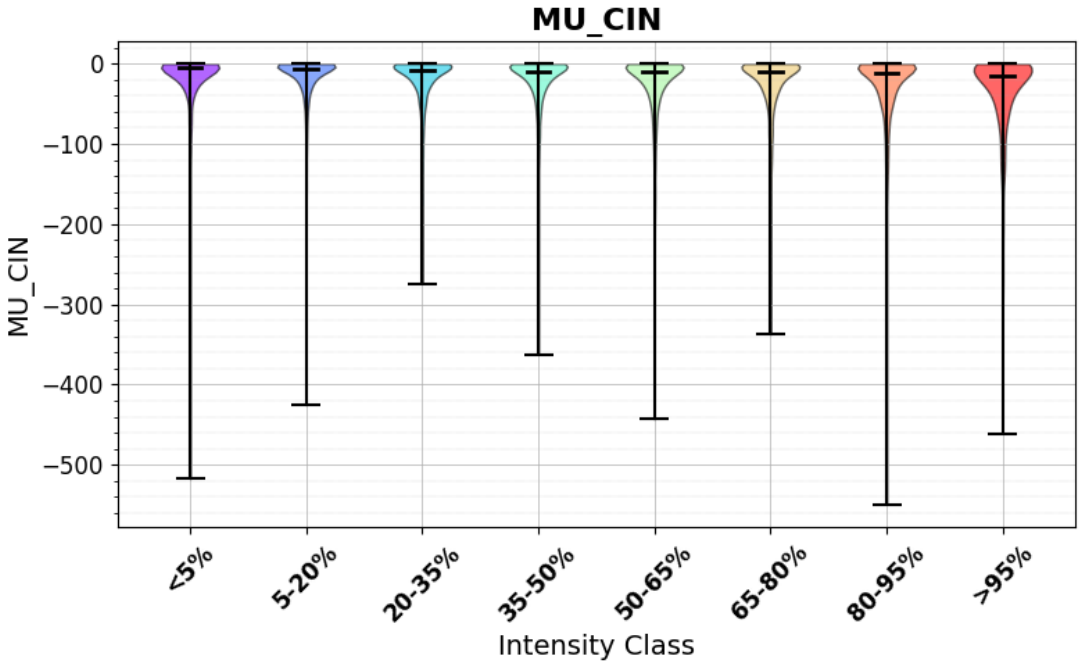

(b) most-unstable convective inhibition in [J kg^{-1}]

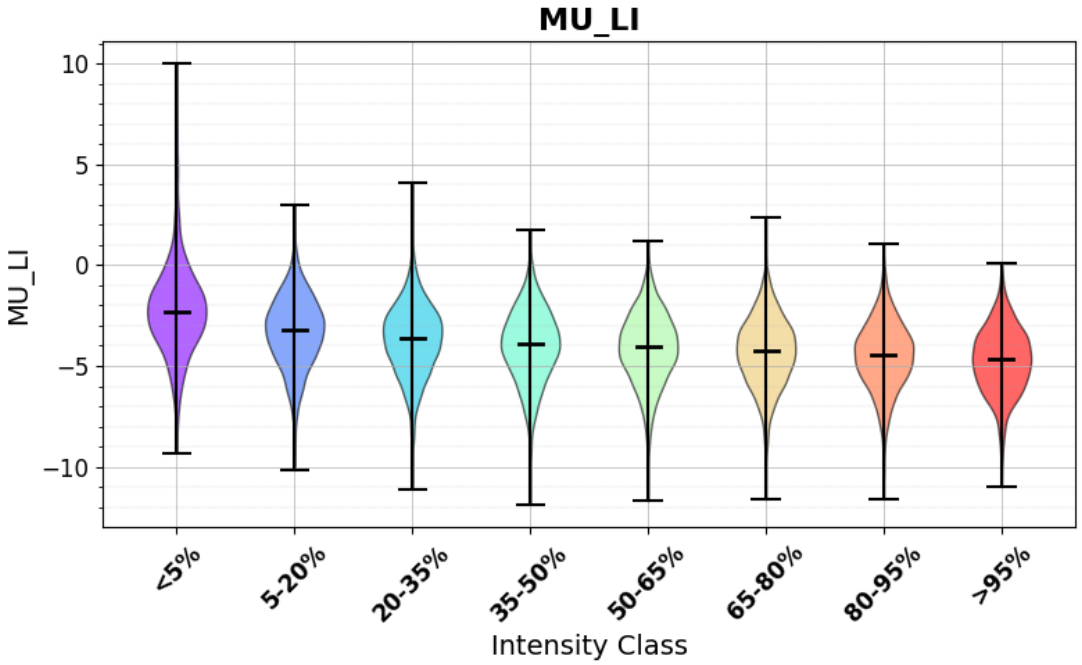

(c) most-unstable lifted index in [K]

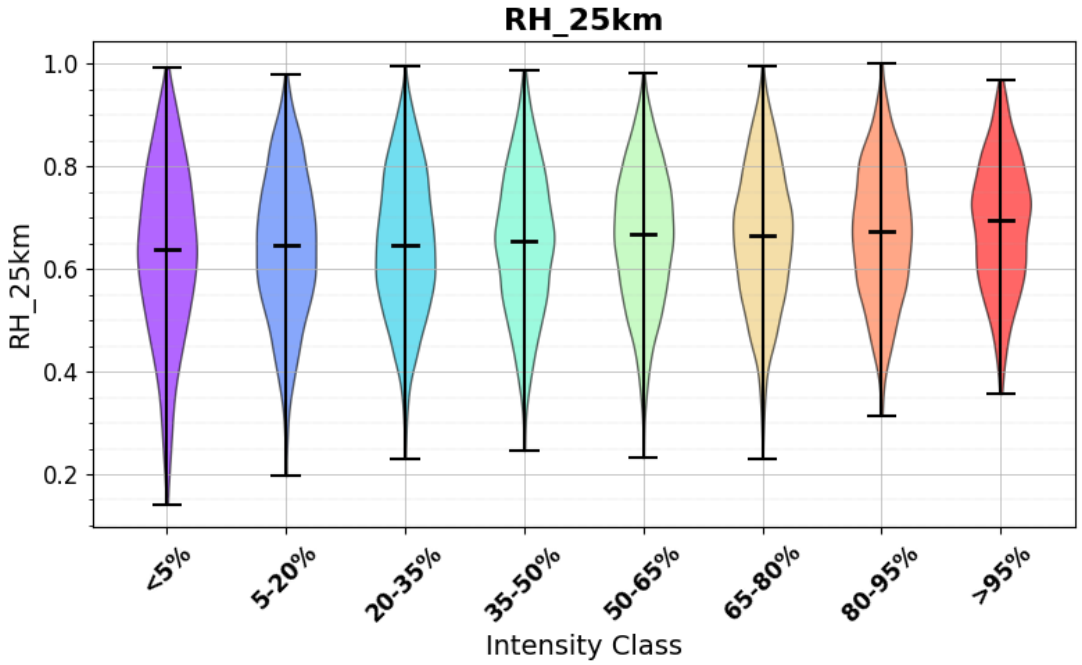

(d) relative humidity between 2 and 5 km in [ ]

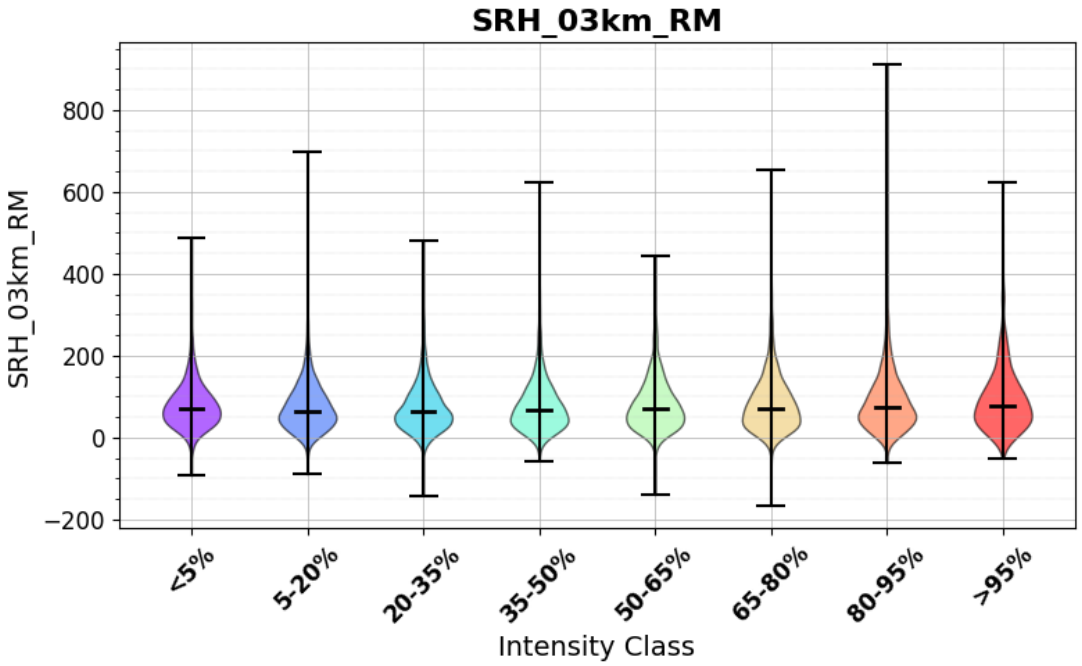

(e) storm-relative helicity between 0 and 3 km for right mover cells in $[m^2\ s^{-2}]$

Figure 4.16: Distribution of selected convective parameters by average lightning activity. Tracks are grouped into lightning intensity categories based on their average number of lightning strikes per track. The colors of the violins indicate the percentile groups, which are applied consistently throughout the analysis. Statistical tests confirm that the light-blue and orange percentile groups differ significantly.

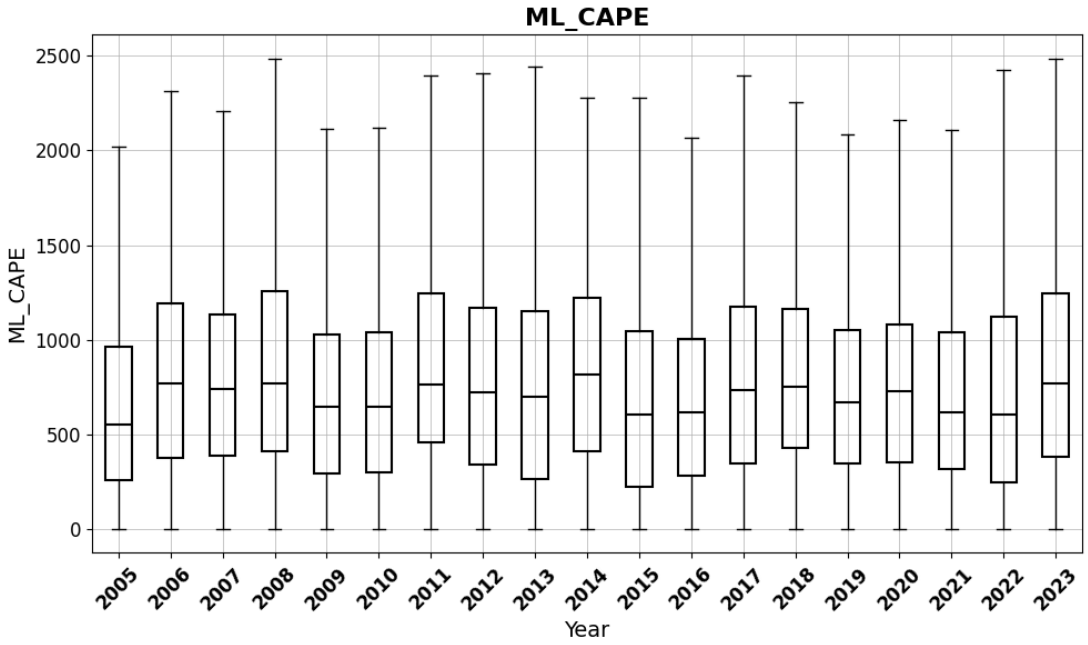

(a) mixed-layer convective available potential energy in [J kg^{-1}]

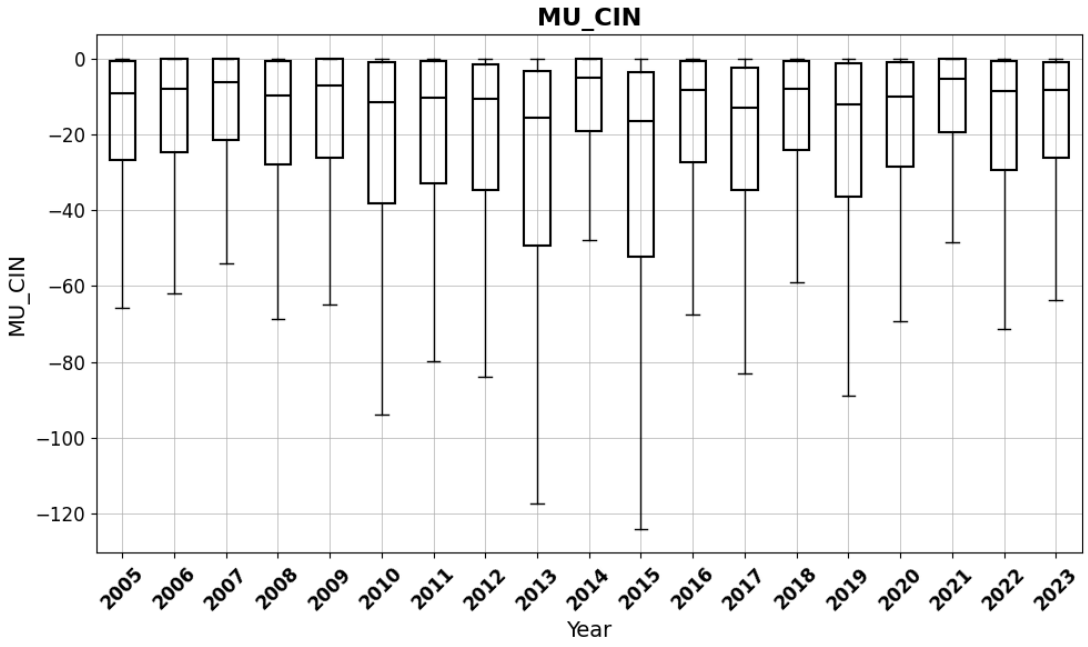

(b) most-unstable convective inhibition in [J kg^{-1}]

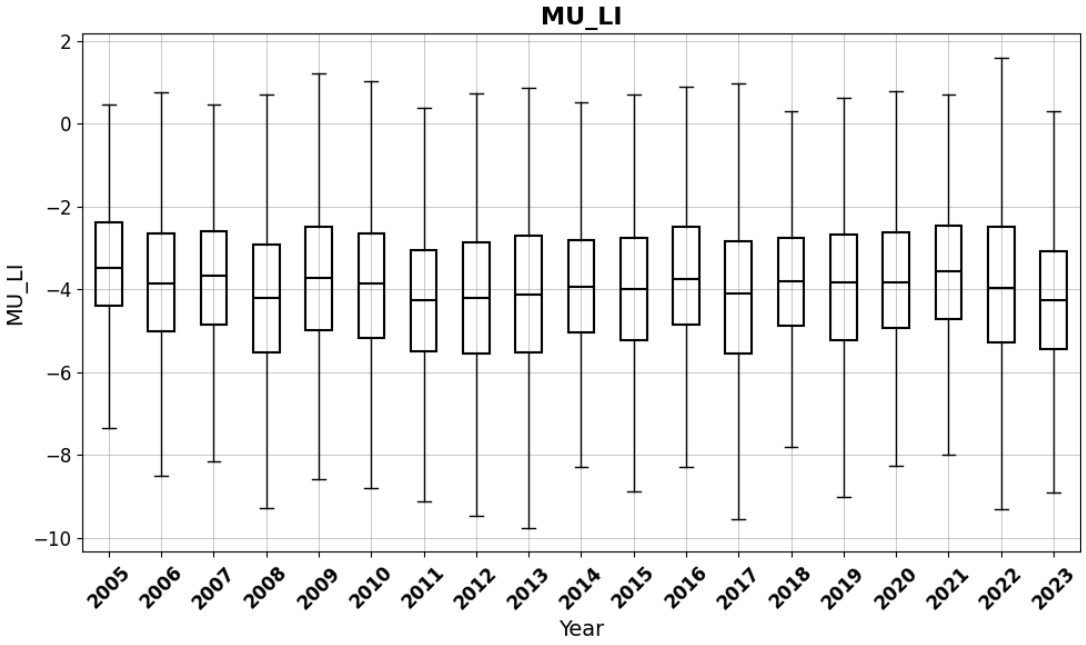

(c) most-unstable lifted index in [K]

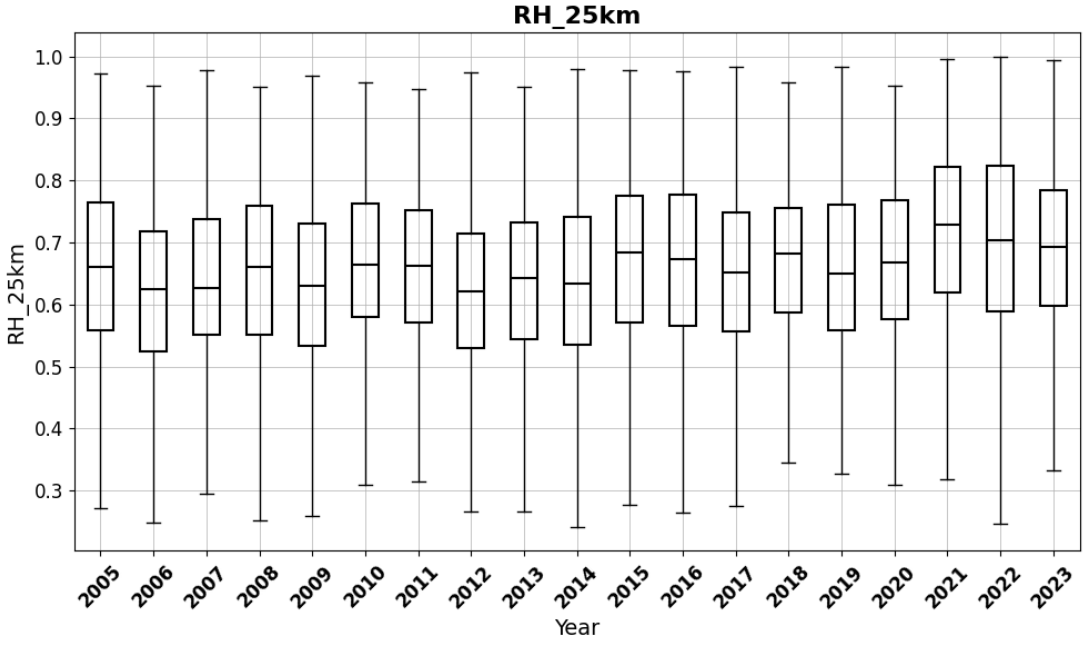

(d) relative humidity between 2 and 5 km in [ ]

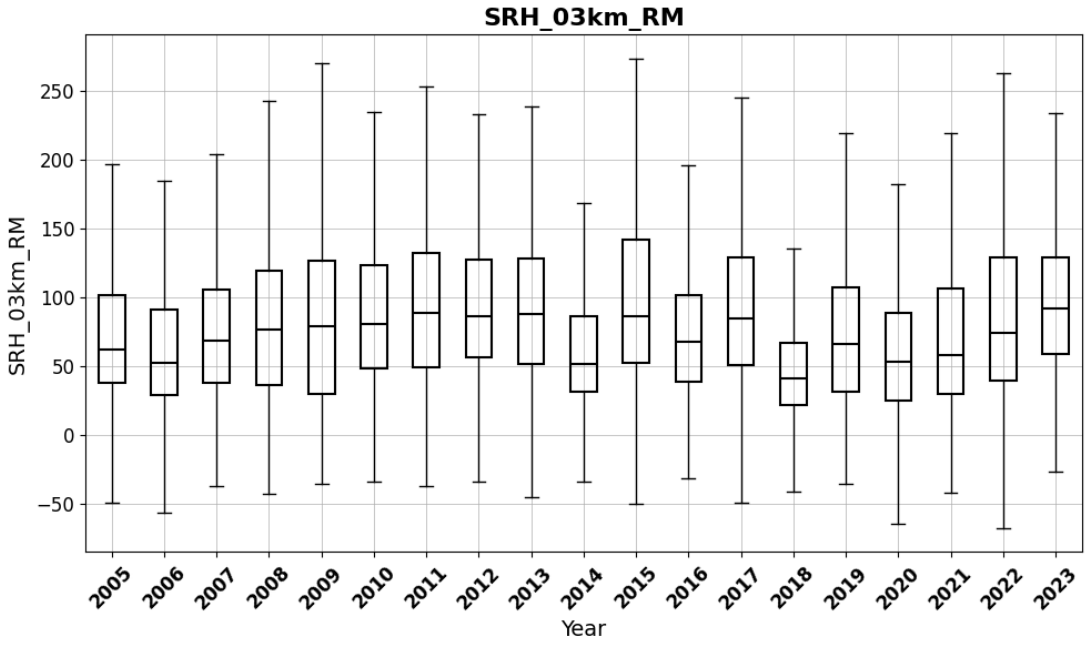

(e) storm-relative helicity between 0 and 3 km for right mover cells in $[m^2\ s^{-2}]$

Figure 4.17: Annual distribution of selected convective parameters.

4.2.2. Atmospheric Aerosols

The atmospheric aerosols are analyzed across lightning intensity classes and years to identify potential links between aerosol conditions and convective strength. As in the convective parameter analysis, PHTs are categorized by lightning intensity. Figure 4.18 shows the distribution of atmospheric aerosol parameters for each lightning intensity category. The parameters selected here exhibit the most distinct signals, while additional parameters are presented in Figure A.5. Significant differences between the 5–20% (low intensity) and 80–95% (high intensity) percentile groups are confirmed by both the t-test and the Mann–Whitney U test. Except for sea salt AOD *ssaod*550, all variables increase with lightning intensity, although to varying degrees. Dust AOD *duaod*550 shows the largest increase in medians (113.6%), while organic matter AOD *omaod*550 shows the smallest (7.6%) (Figure A.5). Sea salt AOD *ssaod*550 decreases with lightning intensity by -28.2%. Median values also increase with particle size: PM_{10} ranges from 2.33 to $3.05 \times 10^{-8}\,\mathrm{kg\,m^{-3}}$, $PM_{2.5}$ from 1.66 to $2.21 \times 10^{-8}\,\mathrm{kg\,m^{-3}}$, and PM_1 from 1.20 to $1.61 \times 10^{-8}\,\mathrm{kg\,m^{-3}}$.
However, as for the convective parameters, the distributions of all parameters overlap considerably with changing lightning intensity. For example, the value of $0.2 \times 10^{-7}\,\mathrm{kg\,m^{-3}}$ in PM can be found near all PHTs for all PM parameters, regardless of the related amount of lightning strikes.

To summarize these findings, Figure 4.19 illustrates the relationship between atmospheric aerosol parameters (excluding sulfate AOD *ssoad*550) and the average number of lightning strikes per track. To enable comparison, parameter ranges are normalized and plotted on the same axis. The normalized range is divided into 30 equally sized bins. For each bin, all track-based lightning counts falling within the corresponding normalized variable interval are extracted, and the average lightning count per track is computed. This procedure is repeated for every CAMS variable, resulting in one binned mean curve per variable. To obtain a generalized relationship across all aerosol variables, the binned mean curves from all variables were averaged. This produces a composite curve representing the overall dependency of lightning activity on the normalized aerosol magnitude. In general, parameter values increase with lightning strikes, reach a maximum, and then decrease, although the trend becomes less clear at higher values due to fewer observations. As the y-axis is normalized, the number of data points decreases towards 1, resulting in higher uncertainty in the mean, visible as fluctuations.
These results are consistent with the theory discussed in section 2.4, which suggests that the

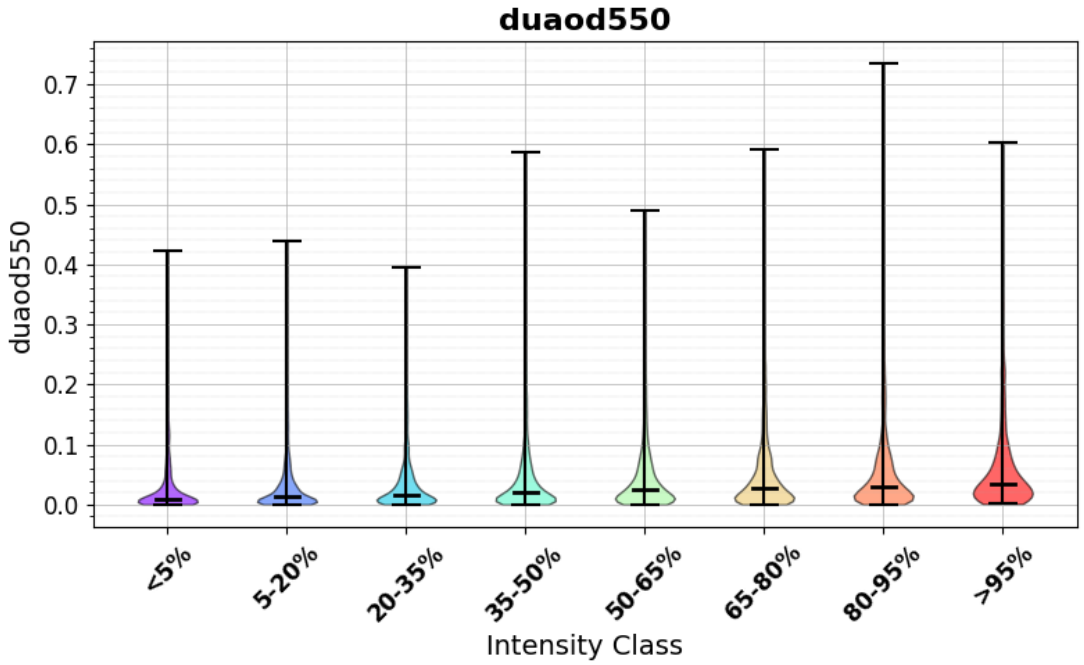

(a) dust aerosol optical depth at 550 nm in [ ]

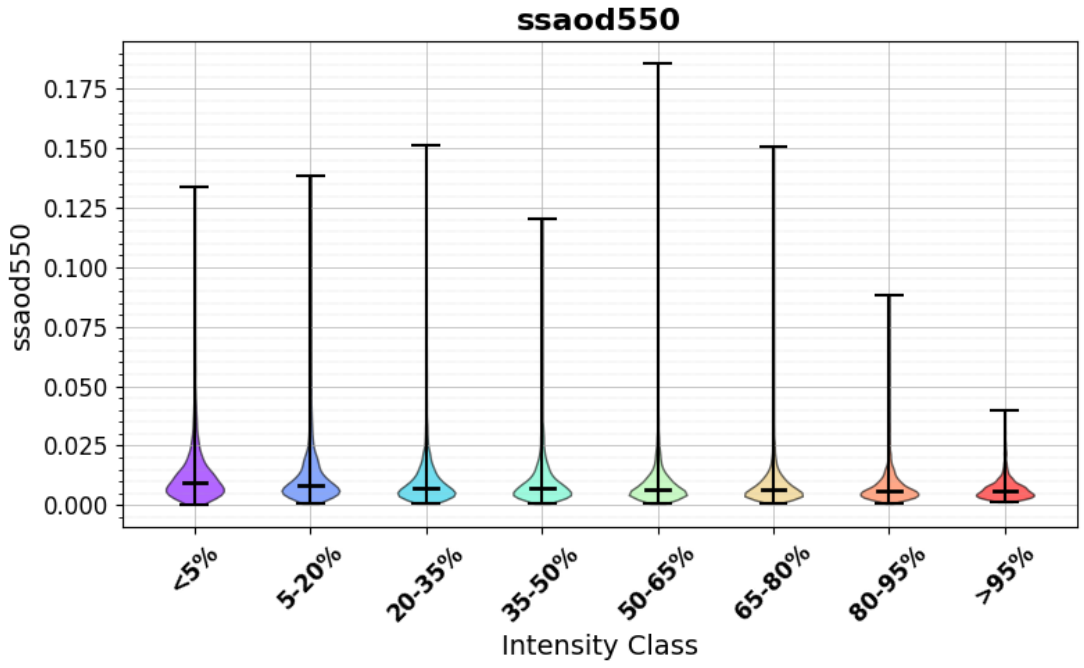

(b) sea salt aerosol optical depth at 550 nm in [ ]

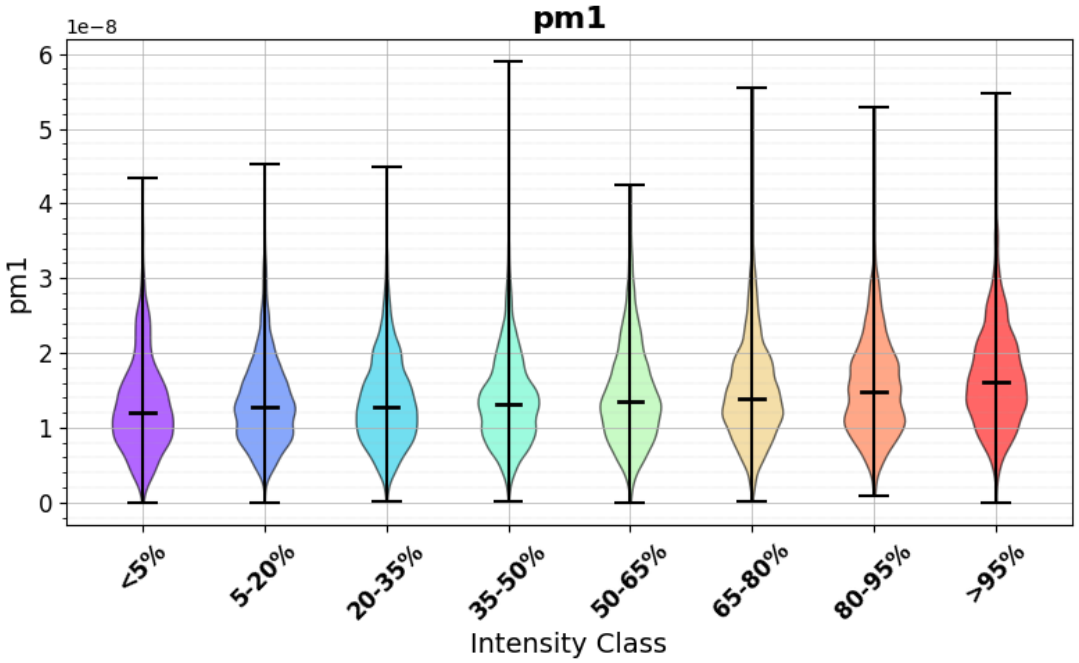

(c) particulate matter with diameter < 1 µm in [kg m^{-3}]

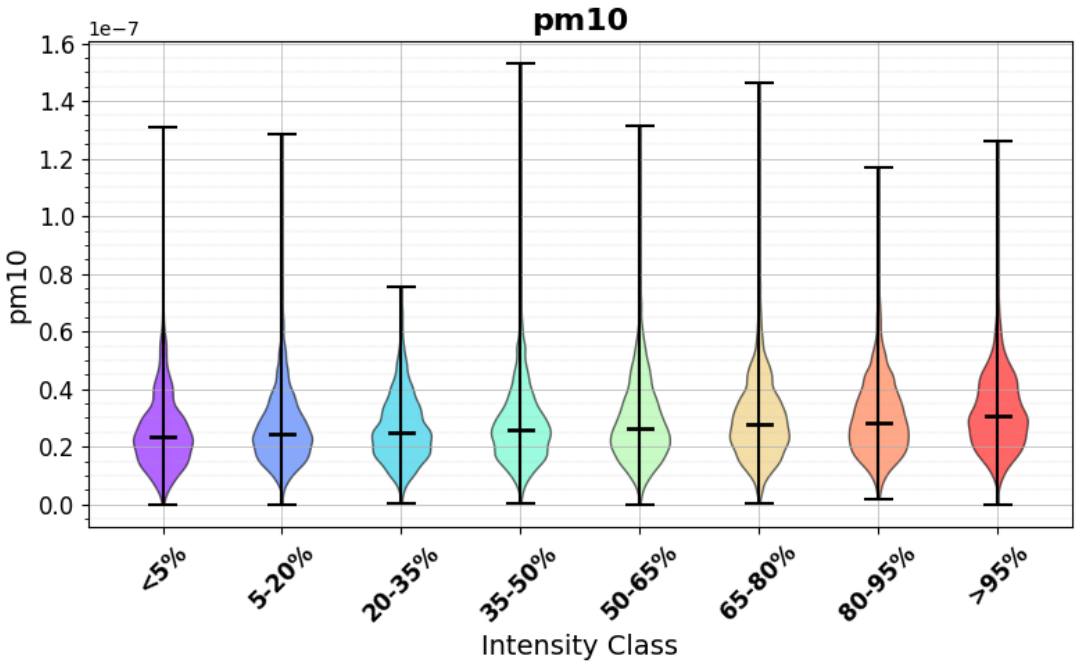

(d) particulate matter with diameter < 10 µm in [kg m^{-3}]

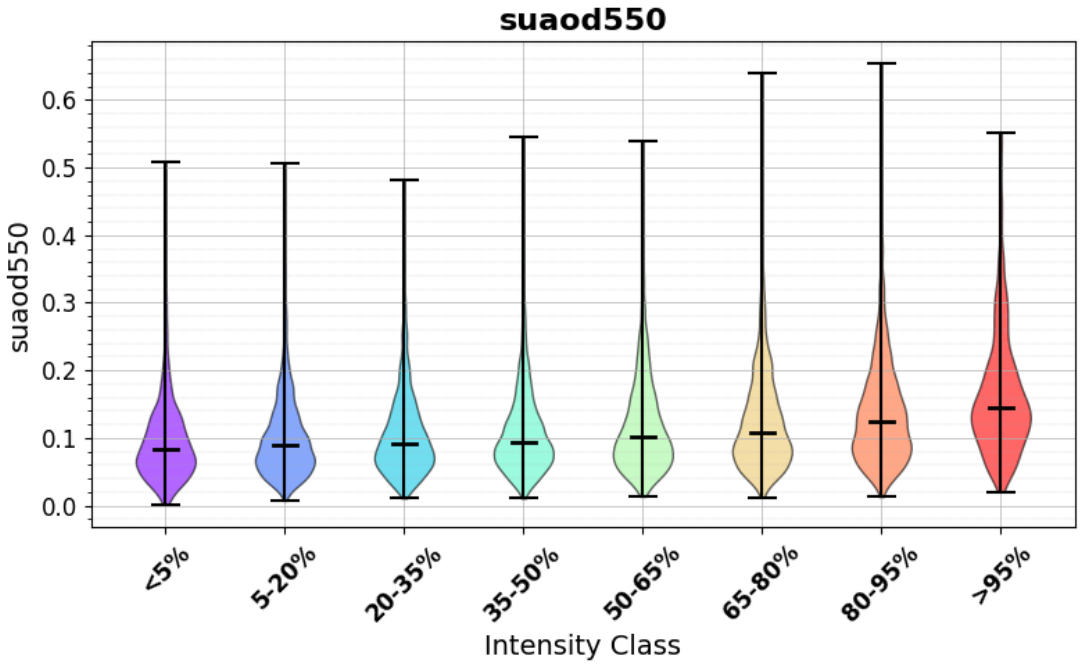

(e) sulfate aerosol optical depth at 550 nm in [ ]

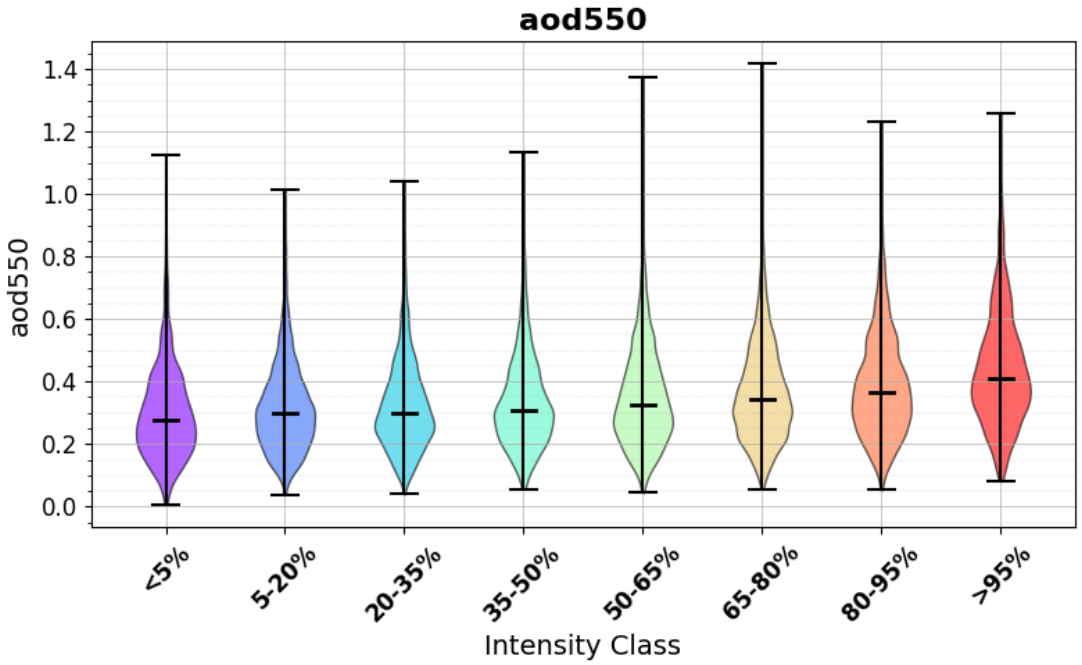

(f) total aerosol optical depth at 550 nm in [ ]

Figure 4.18: Distribution of selected aerosol parameters by average lightning activity. Tracks are grouped into lightning intensity categories based on their average number of lightning strikes per track. The colors of the violins indicate the percentile groups, which are applied consistently throughout the analysis. Statistical tests confirm that the light-blue and orange percentile groups differ significantly.

relationship between lightning occurrence and aerosol concentration is nonlinear. Excessive aerosol loading can inhibit lightning formation.

Annual distributions are shown in Figure 4.20 and Figure A.6. Overall, parameters that increase with lightning intensity exhibit a negative trend over the study period, whereas sea salt AOD *ssaod*550 shows a positive trend. Dust AOD *duaod*550 again displays the largest annual variation, with a 455.5% difference between the lowest median (2005) and the highest (2006), organic matter AOD *omaod*550 shows the smallest variation (10.8%). The three PM parameters vary similarly, with differences between 68.4% and 69.5%. For total AOD *aod*550, the lowest medians occur in 2020, 2023, and 2022, while the highest are in 2006, 2009, 2007, and 2015. Similar patterns apply to sulfate AOD *suaod*550, organic matter AOD *omaod*550, black carbon AOD *bcaod*550 and the *PM* parameters.

These results suggest an association between aerosol concentrations and CG lightning strikes in terms of both intensity and annual frequency. Further, the analysis of aerosol parameters suggests that microphysical processes, particularly those influenced by aerosol loading, play a significant role in modulating lightning occurrence along PHTs.

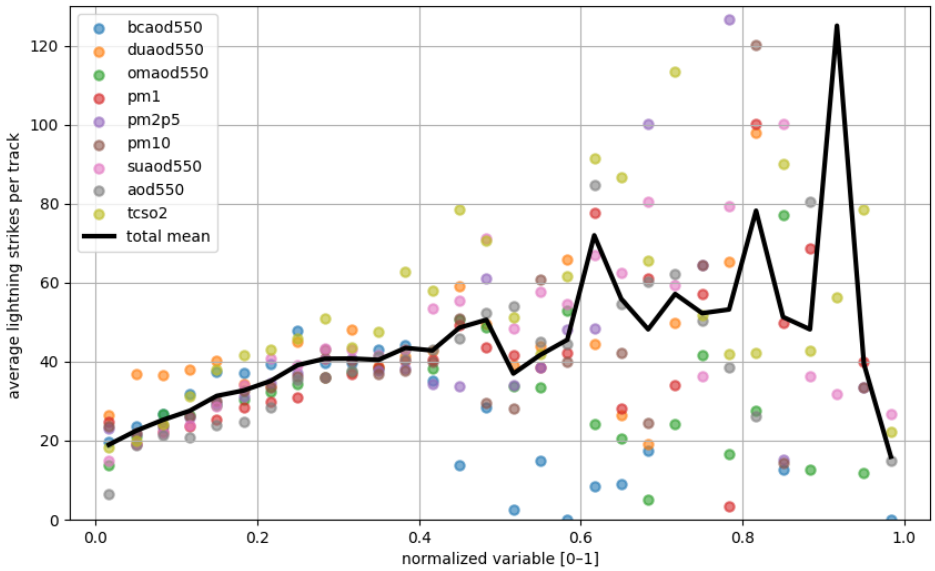

Figure 4.19: Binned average lightning activity as a function of normalized aerosol variables. Each color represents one aerosol variable, obtained by normalizing the variable to [0,1], dividing the range into 30 bins, and calculating the average lightning count per track within each bin. The bold black curve shows the average of all individual variables and represents the overall relationship between aerosol magnitude and lightning activity.

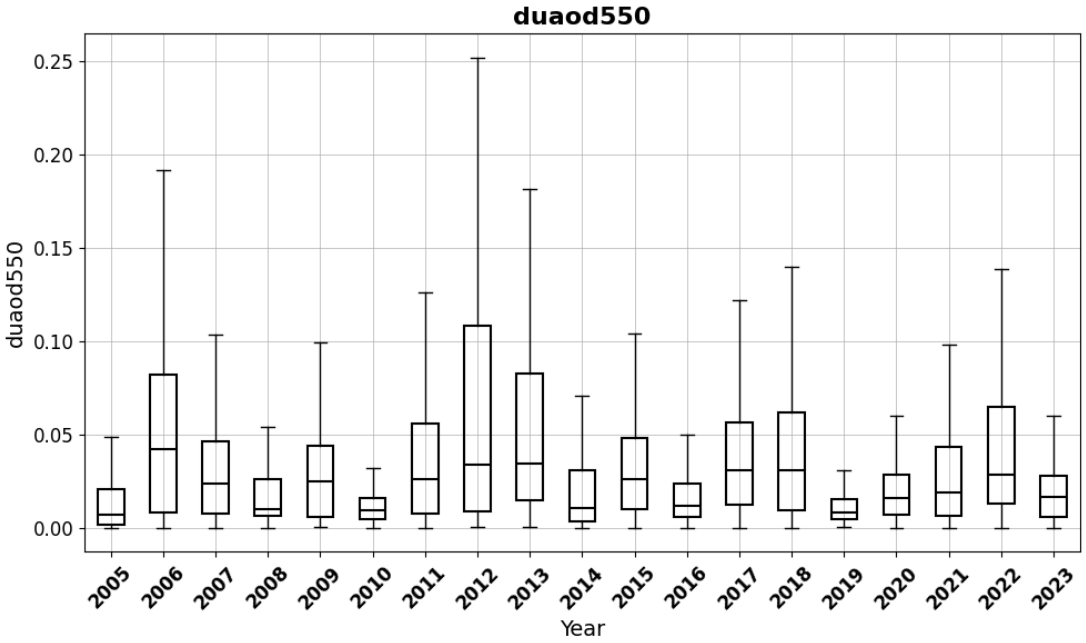

(a) dust aerosol optical depth at 550 nm in [ ]

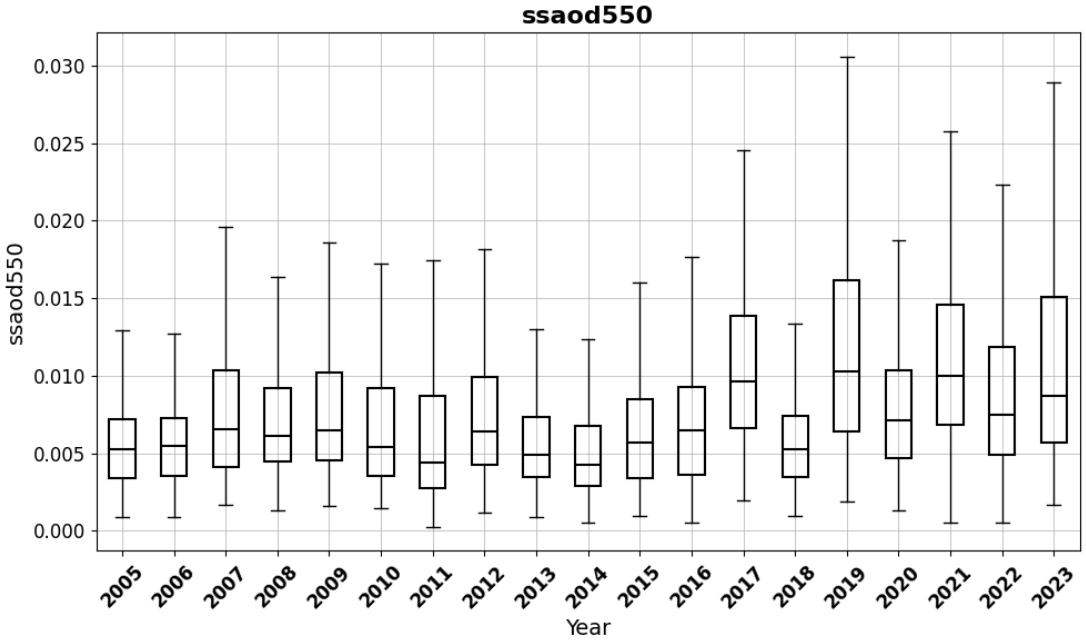

(b) sea salt aerosol optical depth at 550 nm in [ ]

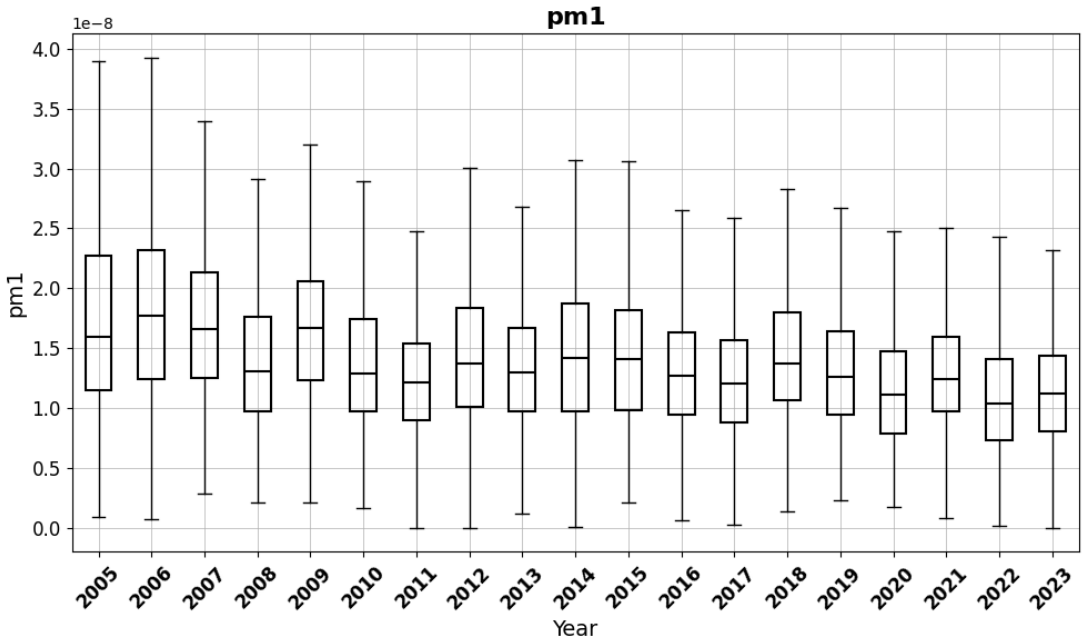

(c) particulate matter with diameter < 1 µm in [kg m^{-3}]

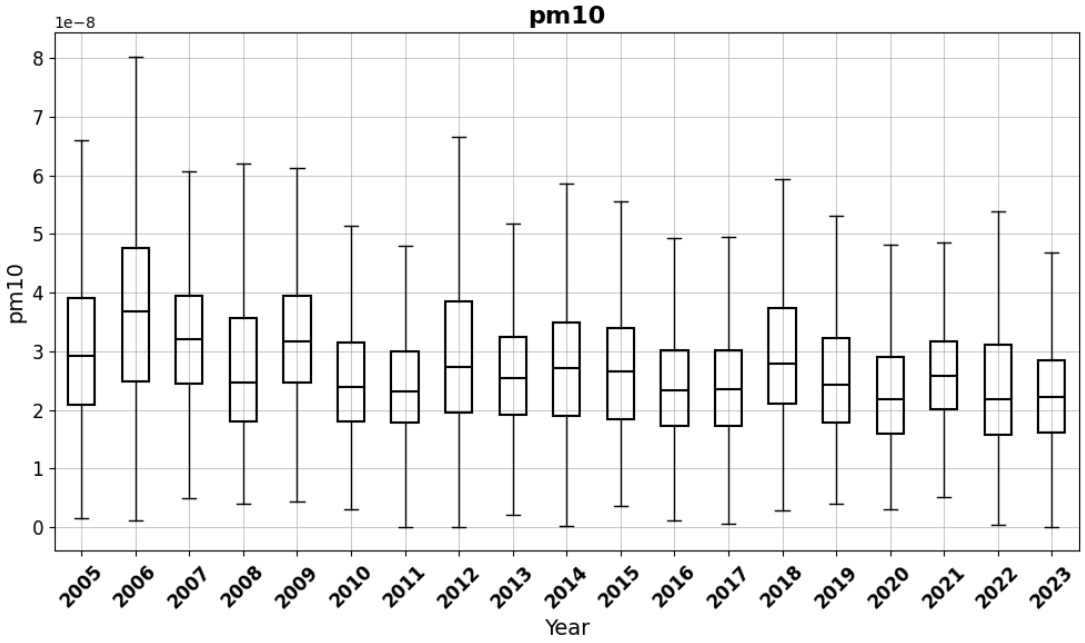

(d) particulate matter with diameter < 10 µm in [kg m^{-3}]

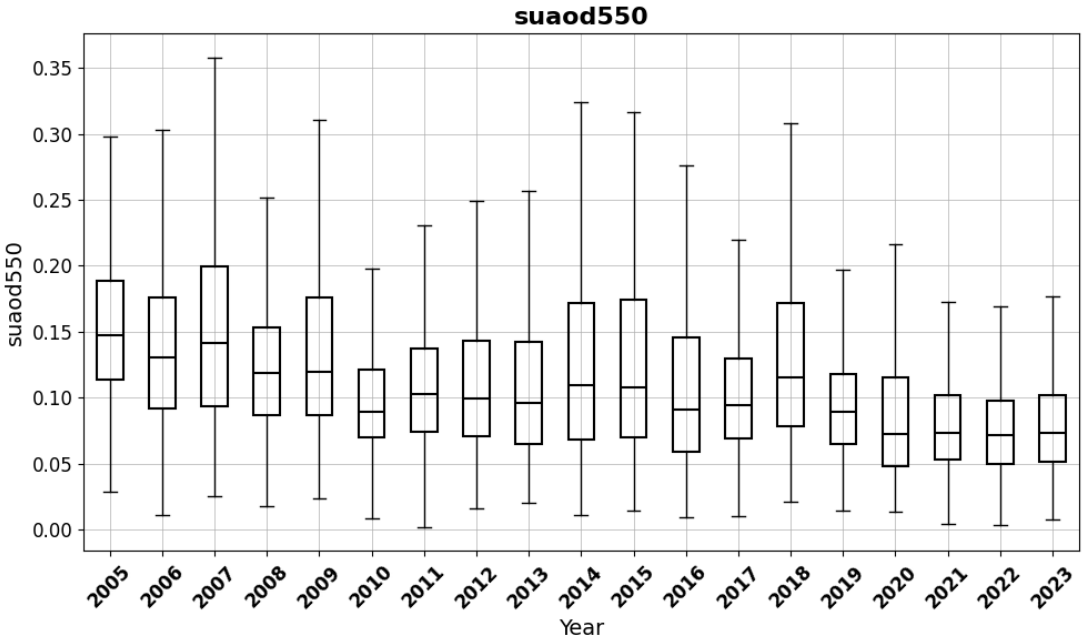

(e) sulphate aerosol optical depth at 550 nm in [ ]

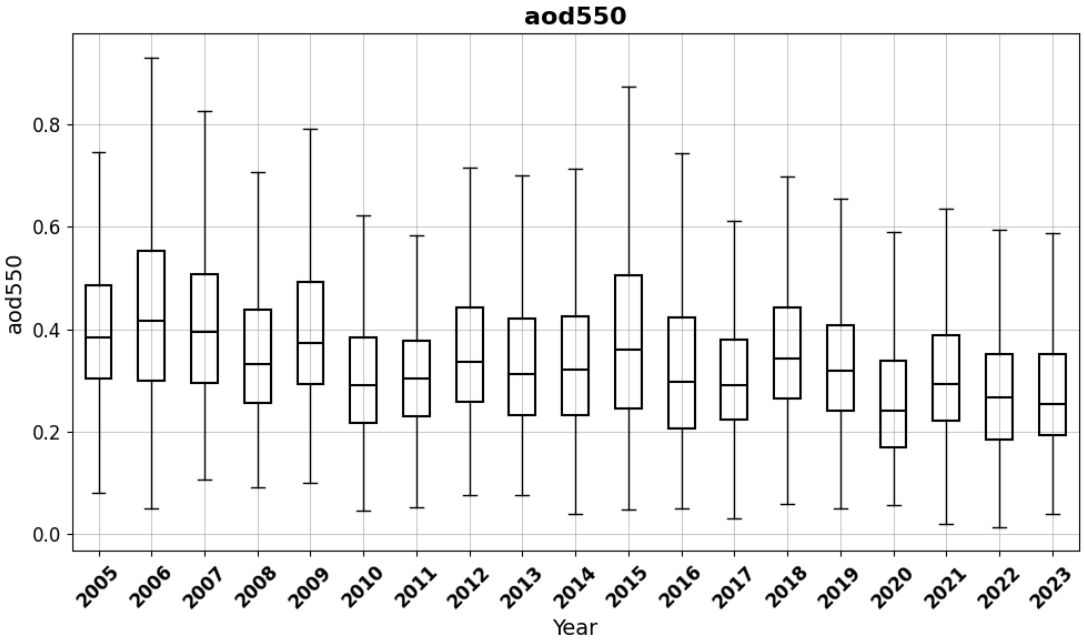

(f) total aerosol optical depth at 550 nm in [ ]

Figure 4.20: Annual distribution of selected aerosol parameters.

5. Conclusion and discussion

This thesis examined lightning characteristics along radar-detected PHTs in Germany and adjacent regions for the period April to September, 2005–2023. PHTs were derived using the TRACE3D algorithm (Handwerker, 2002; Schmidberger, 2018), and lightning strikes were analyzed within a 15 km radius and a 15 min time window around each track time step. The study assessed lightning behavior throughout PHT lifecycles of varying durations, annual variability, and differences between clustered and non-clustered tracks. Additional analyses considered extreme precipitation values ($RXMax3$) and lightning strikes within radar cells exceeding reflectivity thresholds of 46 dBZ and 55 dBZ, respectively, as well as pre-convective environmental conditions based on selected convective and atmospheric parameters (Taszarek et al., 2020; Copernicus Atmosphere Monitoring Service, 2020). The following discussion evaluates these findings in relation to the research questions.

Lightning activity varies during the lifecycle of a PHT and across different PHT durations.
The analysis indicates that longer PHTs generally exhibit higher lightning activity compared to shorter ones. This finding is consistent across both the time step analysis of PHTs of varying durations and the cluster analysis differentiating between shorter and longer PHTs. In the latter case, the average number of lightning strikes per PHT was calculated by dividing the total number of strikes for each track by its duration. This approach rules out the possibility that longer tracks simply accumulate more strikes due to a longer duration. Instead, it suggests that longer PHTs are, on average, more lightning-intensive.
Conversely, the average extreme precipitation measure, $RXMax3$, used as an indicator of storm intensity, shows minimal variation across time steps and between PHTs of different lifetimes. The wide uncertainty range for lightning strike analysis indicates substantial variability among PHTs of the same duration. This variability may arise from local storm dynamics or microphysical processes, highlighting the heterogeneous nature of lightning activity within PHTs. In contrast, the smaller uncertainty range for $RXMax3$ indicates more

consistent precipitation intensity across PHTs.
It could be expected that the onset of intense precipitation would occur later than the start of the PHT, due to differences in radar scan elevation and the descent of hailstones, which are detected at higher altitudes before reaching the surface. This hypothesis could not be confirmed in the present analysis. A likely reason is the temporal resolution of the PHTs (15 min), which may be too coarse to capture such timing differences.
It should also be noted that the radar-detected PHTs are based solely on high reflectivity values. Consequently, the start and end points of the PHTs used here correspond to the occurrence of hail, although the overall storm may persist for longer. As discussed in chapter 2, lightning and hail formation are closely related, which underpins the motivation for this analysis. However, lightning characteristics, and particularly reflectivity attribution, represented here by *RXMax*3, may differ when considering the entire storm lifecycle, before and after hail formation. Changnon (1992) reported that lightning typically occurs about 10 min before hail and, in most cases, around 7 min after hail. This limitation is partly addressed by including a 7.5 min interval before and after the hail occurrence in the analysis. Additionally, the results are consistent with the analysis of Wapler (2017) regarding lightning during the observed hail period.

Lightning activity along PHTs decreases over the period 2005–2023.
Across the entire study area and the sub-tiles, a shift is evident from lightning-intensive years at the beginning of the study period towards less intense years towards its end. The annual sum of lightning strikes decreases over time. However, as this metric depends on the number of PHTs per year, the results were normalized to remove this effect. Even after normalization, the findings reveal a declining proportion of lightning-intensive PHTs and a corresponding increase in tracks with weak lightning activity.
In contrast, the RC attribution *RXMax*3, which reflects PHT intensity, exhibits the opposite behavior. Here, the proportion of PHTs with high extreme precipitation has increased over the study period, while the proportion of weak tracks has decreased. This pattern suggests a tendency for lightning-intensive PHTs to be associated with weaker extreme precipitation and vice versa. However, detailed correlation analysis could not confirm this hypothesis. One possible explanation is that more intense thunderstorms with stronger updrafts produce more hail and lightning strikes. However, this effect might be counteracted by the opposing influence of microphysical processes, as demonstrated in this study. Consequently, no clear relationship emerges between *RXMax*3 and lightning strike frequency. Instead, it indicates that precipitation intensity is distributed relatively evenly within and across

different lightning intensity classes.
The analysis of PHTs with an average lightning strike count below one, based on different selection approaches, reveals a strong dependency on the chosen selection area and time window. Using a constant selection radius of 15 km and a 15 min time window results in the fewest PHTs without CG lightning strikes compared to approaches that rely on the footprint of RCs with varying reflectivity thresholds. Therefore, CG lightning strikes do not occur exclusively near regions of high reflectivity within a thunderstorm but are more widely distributed. This outcome supports the validity of the approach applied in this study and aligns with the findings of Changnon (1992), who reported that lightning most often occurs in areas adjacent to hail streaks.

These variations in lightning activity can be explained by convective and atmospheric aerosol parameters.
To investigate possible reasons for the observed negative trend in lightning strike occurrence along PHTs, pre-convective environmental conditions were examined using convective parameters from ERA5 and atmospheric composition parameters. Both datasets proved moderately suitable for distinguishing between lightning-intensive and less lightning-intensive PHTs, supporting the findings of Taszarek et al. (2017) and Taszarek et al. (2020). However, the significant variation across all parameters should be noted. In general, parameter values occur throughout all lightning intensity classes, which does not allow for a clear distinction between them. This may be a consequence of the methodological approach, which considers pre-convective environmental conditions while recording lightning strikes during the convective phase.
As expected, *ML_CAPE* has increased with higher lightning intensity, accompanied by an increase in *ML_WMAXSHEAR*, which is derived from CAPE. Likewise, *MU_LI* has become more negative with increasing lightning intensity, consistent with its role as an indicator of atmospheric instability. Relative humidity in the lowest layer (*RH_02*) tends to be higher than in the mid-level layer (*RH_25*), which aligns with the theoretical understanding that moisture from lower levels is lifted to support deep convection. It should be noted that Taszarek et al. (2021) reported an underestimation of CAPE values and low-level moisture, as well as an overestimation of mid-tropospheric moisture in ERA5 data compared to in-situ soundings. Additionally, ML parcel representations tend to be more accurate than MU representations (Taszarek et al., 2021).
The observed sulfate patterns are consistent with findings by Wright et al. (2025), who reported elevated concentrations along major shipping lanes. In contrast, sea salt aerosol

shows a more localized behavior, occurring primarily near coastal areas, and therefore cannot be considered representative for the entire study region.
However, when considering the annual distribution, only the atmospheric composition parameters broadly align with the negative trend in lightning strikes. The decrease of *suaod*550 from the beginning of the study period towards the end, aligns with the lightning strike decrease. Additionally, the median *aod*550 fits the general behavior of the annual lightning amount, which emphasizes the hypothesis of aerosol impacts to lightning occurrence. This suggests that the decline in lightning activity is more likely linked to microphysical processes, such as aerosol concentrations or cloud microphysics, rather than thermodynamic, dynamic, or moisture-related factors.
Overall, the results align with the general observation that most lightning activity occurs over land (Christian et al., 2003), where aerosol concentrations are higher and sea salt contributions are minimal.
As shown in sections 2.2.3 and 2.3.4 the effect of climate change on hail storms and lightning is highly uncertain, leading to contradictory hypotheses. The analysis found no trend in the number of PHTs, but an intensification, represented by *RXMax*3, in line with some of the theoretical concepts. The decrease in lightning occurrence generally aligns with the cloud microphysics-based modeling approach of Finney et al. (2018).

Ultimately, the overall conclusion is that hailstorms in Germany have become more intense in recent years, as indicated by increasing radar reflectivity. However, this intensification is not reflected in lightning occurrence, where negative trends in microphysical processes, particularly aerosol concentrations, appear to dominate.

It should be noted that the radar-detected PHTs used in this analysis are subject to limitations arising from the temporal and spatial coverage of the underlying radar data, as well as the tracking algorithm. Similar applies to the reanalysis data. Consequently, the results cannot represent reality with complete accuracy, and the hail tracks should be regarded as potential rather than definitive hail tracks.
It should be acknowledged that the 18-year study period may be relatively short for establishing robust long-term trends. In addition, the annual sample size within each percentile group could introduce uncertainty and potential bias, which should be considered when interpreting the results.
Furthermore, for reasons of data homogeneity, only CG lightning strikes were considered in this study. The analysis could be extended to include CC and IC strikes over the entire study period, rather than being limited to a short time frame as in this thesis. As described in section 2.3.2, CG strikes represent only a fraction of total lightning activity, excluding CC

and IC may underestimate storm electrification. Therefore, such an extension would very likely reduce the number of lightning-free PHTs and provide a more complete representation of storm electrification. In addition, it would enable a more comprehensive analysis of lightning behavior and offer deeper insights into the differences between strikes that reach the ground and those that remain within the cloud.

Further work is needed to improve hail tracking in the northern part of the study area, particularly in maritime regions such as the Baltic Sea and North Sea. In this thesis, these regions were excluded due to the non-physical high number of PHTs without associated lightning.

Future studies should broaden the study area to increase sample size and investigate regional differences, for example between Germany and Europe as a whole, or between Europe and the United States. These studies could identify whether observed trends are region-specific or reflect broader atmospheric changes. Moreover, increasing the temporal resolution of PHTs and environmental parameters would allow for more precise results. This improvement would likely make the PHTs more realistic and enable a clearer assignment of lightning strikes and environmental conditions to individual PHTs.

Finally, the findings of this study, especially regarding environmental conditions as potential drivers of the negative trend in lightning strike occurrence, are not yet conclusive and require further investigation.

In summary, this thesis offers new insights into the relationship between PHTs and lightning activity. It highlights the role of environmental and microphysical factors in storm electrification. These findings contribute to a deeper understanding of severe convective storms in Central Europe and provide a valuable foundation for enhancing forecasting methods and risk assessments. Further research is needed to refine hail tracking and expand the analysis to include all lightning types. However, the results presented here underscore the potential of integrating radar and lightning data to advance severe weather monitoring. This work contributes to the foundation of future studies that aim to understand the complex interactions between atmospheric dynamics, aerosols, and convective processes in a changing climate.

Bibliography

Allen, J. T. (2018). *Climate Change and Severe Thunderstorms*. DOI: 10.1093/acrefore/9780190228620.013.62.

Allen, J. T., I. M. Giammanco, M. R. Kumjian, H. Jurgen Punge, Q. Zhang, P. Groenemeijer, M. Kunz, and K. Ortega (2020). "Understanding Hail in the Earth System". *Reviews of Geophysics* 58.1, e2019RG000665. DOI: https://doi.org/10.1029/2019RG000665.

American Meteorological Society (2022). *Lightning - Glossary of Meteorology*. URL: https://glossary.ametsoc.org/wiki/Lightning (visited on 06/26/2025).

– (2024). *Convective available potential energy - Glossary of Meteorology*. URL: https://glossary.ametsoc.org/wiki/Convective_available_potential_energy (visited on 06/19/2025).

– (2025). *precipitable water - Glossary of Meteorology*. URL: https://glossary.ametsoc.org/wiki/Precipitable_water (visited on 11/11/2025).

Augenstein, M., S. Mohr, and M. Kunz (2024). "Influence of the North Atlantic Oscillation on annual spatio-temporal lightning clusters in western and central Europe". *EGUsphere* 2024, 1–30. DOI: 10.5194/egusphere-2024-2804.

Augenstein, M. (2025). "Variabilität, Trends und serielles Clustering schwerer Gewitterereignisse im Bezug zu großräumigen atmosphärischen Bedingungen". German. PhD Thesis. Karlsruher Institut für Technologie (KIT). DOI: 10.5445/IR/1000179408.

Bartels, H., E. Weigl, S. Klink, O. Kohler, T. Reich, W. Rosenow, P. Lang, C. Podlasly, T. Winterrath, and G. Adrian (2005). *Projekt RADVOR-OP: Radargestützte, zeitnahe Niederschlagsvorhersage für den operationellen Einsatz (Niederschlag-Nowcasting-System) ; zusammenfassender Abschlussbericht für die Projektlaufzeit von 2002 bis 2005*. DWD, Abt. Hydrometeorologie.

Bartels, H., E. Weigl, T. Reich, P. Lang, A. Wagner, O. Kohler, and N. Gerlach (2004). "Projekt RADOLAN-Routineverfahren zur Online-Aneichung der Radarniederschlagsdaten mit Hilfe von automatischen Bodenniederschlagsstationen (Ombrometer): zusammenfassender Abschlussbericht für die Projektlaufzeit von 1997 bis 2004".

Battaglioli, F., P. Groenemeijer, T. Púčik, M. Taszarek, U. Ulbrich, and H. Rust (2023). "Modeled Multidecadal Trends of Lightning and (Very) Large Hail in Europe and North America (1950–2021)". *Journal of Applied Meteorology and Climatology* 62.11. Place: Boston MA, USA Publisher: American Meteorological Society, 1627–1653. DOI: 10.1175/JAMC-D-22-0195.1.

Birant, D. and A. Kut (2007). "ST-DBSCAN: An algorithm for clustering spatial–temporal data". *Data & Knowledge Engineering* 60.1, 208–221. ISSN: 0169-023X. DOI: https://doi.org/10.1016/j.datak.2006.01.013.

Blair, S. F., J. M. Laflin, D. E. Cavanaugh, K. J. Sanders, S. R. Currens, J. I. Pullin, D. T. Cooper, D. R. Deroche, J. W. Leighton, R. V. Fritchie, M. J. M. II, B. T. Goudeau, S. J. Kreller, J. J. Bosco, C. M. Kelly, and H. M. Mallinson (2017). "High-Resolution Hail Observations: Implications for NWS Warning Operations". *Weather and Forecasting* 32.3. Place: Boston MA, USA Publisher: American Meteorological Society, 1101–1119. DOI: 10.1175/WAF-D-16-0203.1.

Bolton, D. (1980). "The Computation of Equivalent Potential Temperature". *Monthly Weather Review* 108.7, 1046–1053. DOI: 10.1175/1520-0493(1980)108<1046:TCOEPT>2.0.CO;2.

Bozzo, A., S. Remy, A. Benedetti, J. Flemming, P. Bechtold, M. Rodwell, and J.-J. Morcrette (2017). *Implementation of a CAMS-based aerosol climatology in the IFS*. Issue: 801 Publication Title: ECMWF Technical Memoranda. DOI: 10.21957/84ya94mls.

Brooks, H. E. (2013). "Severe thunderstorms and climate change". 123, 129–138. ISSN: 0169-8095. DOI: https://doi.org/10.1016/j.atmosres.2012.04.002.

Changnon, S. A. (1992). "Temporal and Spatial Relations between Hail and Lightning". *Journal of Applied Meteorology and Climatology* 31.6. Place: Boston MA, USA Publisher: American Meteorological Society, 587–604. DOI: 10.1175/1520-0450(1992)031<0587:TASRBH>2.0.CO;2.

Christian, H., R. Blakeslee, D. Boccippio, W. Boeck, D. Buechler, K. Driscoll, S. Goodman, J. Hall, W. Koshak, and D. Mach (2003). "Global Frequency and Distribution of Lightning as Observed from Space by the Optical Transient Detector". *Journal of Geophysical Research: Atmospheres* 108. DOI: 10.1029/2002JD002347.

Clark, S. K., D. S. Ward, and N. M. Mahowald (2017). "Parameterization-based uncertainty in future lightning flash density". *Geophysical Research Letters* 44.6, 2893–2901. DOI: https://doi.org/10.1002/2017GL073017.

Copernicus Atmosphere Monitoring Service (2020). *CAMS global reanalysis (EAC4)*. DOI: 10.24381/d58bbf47. (Visited on 08/13/2025).

Copernicus Climate Change Service (2023). *ERA5 hourly data on single levels from 1940 to present*. DOI: 10.24381/cds.adbb2d47. (Visited on 07/30/2025).

Czernecki, B., M. Taszarek, and P. Szuster (2025). *thunder: Computation and Visualisation of Atmospheric Convective Parameters*. URL: https://github.com/bczernecki/thunder.

Dayeh, M. A., A. Farahat, H. Ismail-Aldayeh, and A. Abuelgasim (2021). "Effects of aerosols on lightning activity over the Arabian Peninsula". *Atmospheric Research* 261, 105723. ISSN: 0169-8095. DOI: https://doi.org/10.1016/j.atmosres.2021.105723.

DWD (Jan. 2025). *RADOLAN/RADVOR: Beschreibung des Kompositformats Version 2.6*. Tech. rep. Deutscher Wetterdienst.

Ester, M., H.-P. Kriegel, J. Sander, and X. Xu (Aug. 4, 1996). "A density-based algorithm for discovering clusters in large spatial databases with noise". In: *Proceedings of the Second International Conference on Knowledge Discovery and Data Mining*. KDD'96. Portland, Oregon: AAAI Press, 226–231.

Fan, J., Y. Zhang, Z. Li, H. Yan, T. Prabhakaran, D. Rosenfeld, and A. Khain (2025). "Unveiling Aerosol Impacts on Deep Convective Clouds: Scientific Concept, Modeling, Observational Analysis, and Future Direction". *Journal of Geophysical Research: Atmospheres* 130.15, e2024JD041931. DOI: https://doi.org/10.1029/2024JD041931.

Feingold, G., L. Remer, J. Ramaprasad, and Y. Kaufman (Oct. 2001). "Analysis of smoke impact on clouds in Brazilian biomass burning regions: An extension of Twomey's approach". *Journal of Geophysical Research: Atmospheres* 106.D19, 22907–22922. ISSN: 2169-897X. DOI: 10.1029/2001JD000732.

Finney, D. L., R. M. Doherty, O. Wild, D. S. Stevenson, I. A. MacKenzie, and A. M. Blyth (2018). "A projected decrease in lightning under climate change". *Nature Climate Change* 8.3, 210–213. DOI: 10.1038/s41558-018-0072-6.

Fischer, J., J. M. L. Dahl, B. E. Coffer, J. L. Houser, P. M. Markowski, M. D. Parker, C. C. Weiss, and A. Schueth (2024). "Supercell Tornadogenesis: Recent Progress in Our State of Understanding". *Bulletin of the American Meteorological Society* 105.7. Place: Boston MA, USA Publisher: American Meteorological Society, E1084–E1097. DOI: 10.1175/BAMS-D-23-0031.1.

Franzblau, E. and C. J. Popp (1989). "Nitrogen oxides produced from lightning". *Journal of Geophysical Research: Atmospheres* 94.D8, 11089–11104. DOI: https://doi.org/10.1029/JD094iD08p11089.

Galway, J. G. (1956). "The Lifted Index as a Predictor of Latent Instability". *Bulletin of the American Meteorological Society* 37.10. Place: Boston MA, USA Publisher: American Meteorological Society, 528–529. DOI: 10.1175/1520-0477-37.10.528.

Gesamtverband Deutscher Versicherer (2025). *GDV-Blitzbilanz: Alle 2,5 Minuten ein Blitzschaden*. URL: https://www.gdv.de/gdv/medien/medieninformationen/gdv-blitzbilanz-alle-2-5-minuten-ein-blitzschaden-189098 (visited on 06/27/2025).

Guha, A., Y. Liu, E. Williams, C. Schumann, and H. Hunt (2021). "Lightning Detection and Warning". In: *Lightning: Science, Engineering, and Economic Implications for Developing Countries*. Ed. by C. Gomes. Singapore: Springer Singapore, 1–36. ISBN: 978-981-16-3440-6. DOI: 10.1007/978-981-16-3440-6_2.

Handwerker, J. (2002). "Cell tracking with TRACE3D—a new algorithm". *Atmospheric Research* 61.1, 15–34. ISSN: 0169-8095. DOI: https://doi.org/10.1016/S0169-8095(01)00100-4.

Helmert, K., P. Tracksdorf, J. Steinert, M. Werner, M. Frech, T. Hengstebeck, M. Mott, S. Schumann, and T. Mammen (Sept. 5, 2014). "DWDs new radar network and post-processing algorithm chain". *8th Europ. Conf. on Radar in Meteorology and Hydrology*.

Hersbach, H., B. Bell, P. Berrisford, G. Biavati, A. Horányi, J. Muñoz Sabater, J. Nicolas, C. Peubey, R. Radu, I. Rozum, D. Schepers, A. Simmons, C. Soci, D. Dee, and J.-N. Thépaut (2023). "ERA5 hourly data on single levels from 1940 to present." *Copernicus Climate Change Service (C3S) Climate Data Store (CDS)*. DOI: 10.24381/cds.adbb2d47. (Visited on 07/30/2025).

Hersbach, H., B. Bell, P. Berrisford, S. Hirahara, A. Horányi, J. Muñoz-Sabater, J. Nicolas, C. Peubey, R. Radu, D. Schepers, A. Simmons, C. Soci, S. Abdalla, X. Abellan, G. Balsamo, P. Bechtold, G. Biavati, J. Bidlot, M. Bonavita, G. De Chiara, P. Dahlgren, D. Dee, M. Diamantakis, R. Dragani, J. Flemming, R. Forbes, M. Fuentes, A. Geer, L. Haimberger, S. Healy, R. J. Hogan, E. Hólm, M. Janisková, S. Keeley, P. Laloyaux, P. Lopez, C. Lupu, G. Radnoti, P. de Rosnay, I. Rozum, F. Vamborg, S. Villaume, and J.-N. Thépaut (2020). "The ERA5 global reanalysis". *Quarterly Journal of the Royal Meteorological Society* 146.730, 1999–2049. DOI: https://doi.org/10.1002/qj.3803.

Hoose, C. and O. Möhler (2012). "Heterogeneous ice nucleation on atmospheric aerosols: a review of results from laboratory experiments". *Atmospheric Chemistry and Physics* 12.20, 9817–9854. DOI: 10.5194/acp-12-9817-2012.

Houze, R. A. (1993). *Cloud Dynamics*. Academic Press. ISBN: 978-0-12-356881-6.

Inness, A., M. Ades, A. Agustí-Panareda, J. Barré, A. Benedictow, A.-M. Blechschmidt, J. J. Dominguez, R. Engelen, H. Eskes, J. Flemming, V. Huijnen, L. Jones, Z. Kipling, S. Massart, M. Parrington, V.-H. Peuch, M. Razinger, S. Remy, M. Schulz, and M. Suttie (2019). "The CAMS reanalysis of atmospheric composition". *Atmospheric Chemistry and Physics* 19.6, 3515–3556. DOI: 10.5194/acp-19-3515-2019.

IPCC (2023a). "Water Cycle Changes". In: *Climate Change 2021 – The Physical Science Basis: Working Group I Contribution to the Sixth Assessment Report of the Intergovernmental Panel on Climate Change*. Cambridge University Press, 1055–1210.

– (2023b). “Weather and Climate Extreme Events in a Changing Climate”. In: *Climate Change 2021 – The Physical Science Basis: Working Group I Contribution to the Sixth Assessment Report of the Intergovernmental Panel on Climate Change*. Cambridge University Press, 1513–1766.

Jiang, J. H., H. Su, L. Huang, Y. Wang, S. Massie, B. Zhao, A. Omar, and Z. Wang (Sept. 2018). “Contrasting effects on deep convective clouds by different types of aerosols”. *Nature Communications* 9.1, 3874. ISSN: 2041-1723. DOI: 10.1038/s41467-018-06280-4.

Johns, R. H. and C. A. Doswell (1992). “Severe Local Storms Forecasting”. *Weather and Forecasting* 7.4. Place: Boston MA, USA Publisher: American Meteorological Society, 588–612. DOI: 10.1175/1520-0434(1992)007<0588:SLSF>2.0.CO;2.

Kopp, J., A. Hering, U. Germann, and O. Martius (2024). “Verification of weather-radar-based hail metrics with crowdsourced observations from Switzerland”. *Atmospheric Measurement Techniques* 17.14, 4529–4552. DOI: 10.5194/amt-17-4529-2024.

Koren, I., Y. J. Kaufman, L. A. Remer, and J. V. Martins (2004). “Measurement of the Effect of Amazon Smoke on Inhibition of Cloud Formation”. *Science* 303.5662, 1342–1345. DOI: 10.1126/science.1089424.

Koren, I., Y. J. Kaufman, D. Rosenfeld, L. A. Remer, and Y. Rudich (2005). “Aerosol invigoration and restructuring of Atlantic convective clouds”. *Geophysical Research Letters* 32.14. DOI: https://doi.org/10.1029/2005GL023187.

Krehbiel, P. R. (1986). “The electrical structure of thunderstorms.” In: *Studies in geophysics: The Earth’s electrical environment*. Ed. by E. Krider and R. Roble. Washington: National Academy Press, 90–113.

Kunz, M. (2007). “The skill of convective parameters and indices to predict isolated and severe thunderstorms”. *Natural Hazards and Earth System Sciences* 7.2, 327–342. DOI: 10.5194/nhess-7-327-2007.

Kunz, M. and P. I. S. Kugel (2015). “Detection of hail signatures from single-polarization C-band radar reflectivity”. *Atmospheric Research* 153, 565–577. ISSN: 0169-8095. DOI: https://doi.org/10.1016/j.atmosres.2014.09.010.

Lamb, D. and J. Verlinde (2011). *Physics and Chemistry of Clouds*. Cambridge, United Kingdom: Cambridge University Press. ISBN: 978-1-139-18572-1.

Mahoney, K. (2020). “Extreme Hail Storms and Climate Change: Foretelling the Future in Tiny, Turbulent Crystal Balls?” *Bulletin of the American Meteorological Society* 101.1. Place: Boston MA, USA Publisher: American Meteorological Society, S17–S22. DOI: 10.1175/BAMS-D-19-0233.1.

Mann, H. B. and D. R. Whitney (1947). "On a test of whether one of two random variables is stochastically larger than the other". *The annals of mathematical statistics*. Publisher: JSTOR, 50–60.

Markowski, P. and Y. Richardson (2010). *Mesoscale Meteorology in Midlatitudes*. 1st ed. ISBN: 978-0-470-74213-6 978-0-470-68210-4. Wiley. DOI: 10.1002/9780470682104.

Mason, B. (1971). *The Physics of Clouds*. Oxford classic texts in the physical sciences. Clarendon Press. ISBN: 978-0-19-851603-3.

Munich Re (2025). *Hail, tornadoes, flash floods: Losses from thunderstorms on the rise*. URL: https://www.munichre.com/en/risks/natural-disasters/thunderstorms-hail-tornados.html (visited on 06/27/2025).

Murillo, E. M., C. R. Homeyer, and J. T. Allen (2021). "A 23-Year Severe Hail Climatology Using GridRad MESH Observations". *Monthly Weather Review* 149.4. Place: Boston MA, USA Publisher: American Meteorological Society, 945–958. DOI: 10.1175/MWR-D-20-0178.1.

Peterson, M. (2023). "Interactions Between Lightning and Ship Traffic". *Earth and Space Science* 10.11, e2023EA002926. DOI: https://doi.org/10.1029/2023EA002926.

Poelman, D. R. and W. Schulz (2020). "Comparing lightning observations of the ground-based European lightning location system EUCLID and the space-based Lightning Imaging Sensor (LIS) on the International Space Station (ISS)". *Atmospheric Measurement Techniques* 13.6, 2965–2977. DOI: 10.5194/amt-13-2965-2020.

Poelman, D. R., W. Schulz, G. Diendorfer, and M. Bernardi (2016). "The European lightning location system EUCLID – Part 2: Observations". *Natural Hazards and Earth System Sciences* 16.2, 607–616. DOI: 10.5194/nhess-16-607-2016.

Pucik, T., P. Groenemeijer, and I. Tsonevsky (2021). *Vertical wind shear and convective storms*. Issue: 879 Publication Title: ECMWF Technical Memoranda. DOI: 10.21957/z0b3t5mrv.

Punge, H. J. and M. Kunz (2016). "Hail observations and hailstorm characteristics in Europe: A review". *Atmospheric Research* 176-177, 159–184. ISSN: 0169-8095. DOI: https://doi.org/10.1016/j.atmosres.2016.02.012.

Puskeiler, M., M. Kunz, and M. Schmidberger (2016). "Hail statistics for Germany derived from single-polarization radar data". *Atmospheric Research* 178-179, 459–470. ISSN: 0169-8095. DOI: https://doi.org/10.1016/j.atmosres.2016.04.014.

Radke, L. F., J. A. Coakley, and M. D. King (1989). "Direct and Remote Sensing Observations of the Effects of Ships on Clouds". *Science* 246.4934, 1146–1149. DOI: 10.1126/science.246.4934.1146.

Radke, L. F. and P. V. Hobbs (1976). "Cloud Condensation Nuclei on the Atlantic Seaboard of the United States". *Science* 193.4257, 999–1002. DOI: 10.1126/science.193.4257.999.

Rädler, A. T., P. H. Groenemeijer, E. Faust, R. Sausen, and T. Púčik (2019). "Frequency of severe thunderstorms across Europe expected to increase in the 21st century due to rising instability". *npj Climate and Atmospheric Science* 2.1, 30. ISSN: 2397-3722. DOI: 10.1038/s41612-019-0083-7.

Rakov, V. A. (2021). "Lightning, the Science". In: *Lightning: Science, Engineering, and Economic Implications for Developing Countries*. Ed. by C. Gomes. Singapore: Springer Singapore, 1–36. ISBN: 978-981-16-3440-6. DOI: 10.1007/978-981-16-3440-6_1.

Raupach, T. H., O. Martius, J. T. Allen, M. Kunz, S. Lasher-Trapp, S. Mohr, K. L. Rasmussen, R. J. Trapp, and Q. Zhang (2021). "The effects of climate change on hailstorms". en. *Nature Reviews Earth & Environment* 2.3. Publisher: Nature Publishing Group, 213–226. ISSN: 2662-138X. DOI: 10.1038/s43017-020-00133-9.

Romps, D. M., J. T. Seeley, D. Vollaro, and J. Molinari (2014). "Projected increase in lightning strikes in the United States due to global warming". *Science* 346.6211, 851–854. DOI: 10.1126/science.1259100.

Rosenfeld, D., M. O. Andreae, A. Asmi, M. Chin, G. de Leeuw, D. P. Donovan, R. Kahn, S. Kinne, N. Kivekäs, M. Kulmala, W. Lau, K. S. Schmidt, T. Suni, T. Wagner, M. Wild, and J. Quaas (2014). "Global observations of aerosol-cloud-precipitation-climate interactions". *Reviews of Geophysics* 52.4, 750–808. DOI: https://doi.org/10.1002/2013RG000441.

Ross, T. I. D. and S. Lasher-Trapp (2025). "Investigating the Relative Roles of INPs and CCN in a Simulated Thunderstorm Using a New Immersion Freezing Algorithm". *Journal of Geophysical Research: Atmospheres* 130.10, e2024JD042592. DOI: https://doi.org/10.1029/2024JD042592.

Schmid, T., V. Gebhart, and D. N. Bresch (2025). "Improved Real-Time Hail Damage Estimates Leveraging Dense Crowdsourced Observations". *Meteorological Applications* 32.3, e70059. DOI: https://doi.org/10.1002/met.70059.

Schmidberger, M. (2018). "Hagelgefährdung und Hagelrisiko in Deutschland basierend auf einer Kombination von Radardaten und Versicherungsdaten". ISBN: 978-3-7315-0846-5 ISSN: 0179-5619 Series: Wissenschaftliche Berichte des Instituts für Meteorologie und Klimaforschung des Karlsruher Instituts für Technologie Volume: 78. PhD Thesis. Karlsruher Institut für Technologie (KIT). DOI: 10.5445/KSP/1000086012.

Schulz, W., G. Diendorfer, S. Pedeboy, and D. R. Poelman (2016). "The European lightning location system EUCLID – Part 1: Performance analysis and validation". *Natural Hazards and Earth System Sciences* 16.2, 595–605. DOI: 10.5194/nhess-16-595-2016.

Seinfeld, J. H. and S. N. Pandis (2016). *Atmospheric Chemistry and Physics: From Air Pollution to Climate Change*. New York, United States: John Wiley & Sons, Incorporated. ISBN: 978-1-119-22116-6.

Student (1908). "The Probable Error of a Mean". *Biometrika* 6.1. Publisher: [Oxford University Press, Biometrika Trust], 1–25. ISSN: 00063444, 14643510.

Taszarek, M., J. T. Allen, T. Púčik, K. A. Hoogewind, and H. E. Brooks (2020). "Severe Convective Storms across Europe and the United States. Part II: ERA5 Environments Associated with Lightning, Large Hail, Severe Wind, and Tornadoes". *Journal of Climate* 33.23. Place: Boston MA, USA Publisher: American Meteorological Society, 10263–10286. DOI: 10.1175/JCLI-D-20-0346.1.

Taszarek, M., H. E. Brooks, and B. Czernecki (2017). "Sounding-Derived Parameters Associated with Convective Hazards in Europe". *Monthly Weather Review* 145.4. Place: Boston MA, USA Publisher: American Meteorological Society, 1511–1528. DOI: 10.1175/MWR-D-16-0384.1.

Taszarek, M., N. Pilguj, J. Allen, V. Gensini, H. Brooks, and P. Szuster (2021). "Comparison of Convective Parameters Derived from ERA5 and MERRA-2 with Rawinsonde Data over Europe and North America". *Journal of Climate* 34. DOI: 10.1175/JCLI-D-20-0484.1.

Trapp, R. J. (2013). *Mesoscale-Convective Processes in the Atmosphere*. Cambridge University Press.

Twomey, S. (1974). "Pollution and the planetary albedo". *Atmospheric Environment (1967)* 8.12, 1251–1256. ISSN: 0004-6981. DOI: https://doi.org/10.1016/0004-6981(74)90004-3.

Veraverbeke, S., B. M. Rogers, M. L. Goulden, R. R. Jandt, C. E. Miller, E. B. Wiggins, and J. T. Randerson (2017). "Lightning as a major driver of recent large fire years in North American boreal forests". *Nature Climate Change* 7.7, 529–534. ISSN: 1758-6798. DOI: 10.1038/nclimate3329.

Waldteufel, P. and H. Corbin (1979). "On the Analysis of Single-Doppler Radar Data". *Journal of Applied Meteorology and Climatology* 18.4. Place: Boston MA, USA Publisher: American Meteorological Society, 532–542. DOI: 10.1175/1520-0450(1979)018<0532:OTAOSD>2.0.CO;2.

Wang, Q., Z. Li, J. Guo, C. Zhao, and M. Cribb (2018). "The climate impact of aerosols on the lightning flash rate: is it detectable from long-term measurements?" *Atmospheric Chemistry and Physics* 18.17, 12797–12816. DOI: 10.5194/acp-18-12797-2018.

Wapler, K. (2017). "The life-cycle of hailstorms: Lightning, radar reflectivity and rotation characteristics". *Atmospheric Research* 193, 60–72. ISSN: 0169-8095. DOI: https://doi.org/10.1016/j.atmosres.2017.04.009. URL: https://www.sciencedirect.com/science/article/pii/S0169809516306020.

Westcott, N. E. (1995). "Summertime Cloud-to-Ground Lightning Activity around Major Midwestern Urban Areas". *Journal of Applied Meteorology and Climatology* 34.7. Place:

Boston MA, USA Publisher: American Meteorological Society, 1633–1642. DOI: 10.1175/1520-0450-34.7.1633.

Whaley, C., M. Etten-Bohm, C. Schumacher, A. Akingunola, V. Arora, J. Cole, M. Lazare, D. Plummer, K. von Salzen, and B. Winter (2024). "A new lightning scheme in the Canadian Atmospheric Model (CanAM5.1): implementation, evaluation, and projections of lightning and fire in future climates". *Geoscientific Model Development* 17.18, 7141–7155. DOI: 10.5194/gmd-17-7141-2024.

Wilhelm, J. (2022). "Einfluss atmosphärischer Umgebungsbedingungen auf den Lebenszyklus konvektiver Zellen in der Echtzeit-Vorhersage". ISBN: 978-3-7315-1182-3 ISSN: 0179-5619 Series: Wissenschaftliche Berichte des Instituts für Meteorologie und Klimaforschung des Karlsruher Instituts für Technologie Volume: 85. PhD Thesis. Karlsruher Institut für Technologie (KIT). DOI: 10.5445/KSP/1000145542.

Witt, A., M. D. Eilts, G. J. Stumpf, J. T. Johnson, E. D. W. Mitchell, and K. W. Thomas (1998). "An Enhanced Hail Detection Algorithm for the WSR-88D". *Weather and Forecasting* 13.2. Place: Boston MA, USA Publisher: American Meteorological Society, 286–303. DOI: 10.1175/1520-0434(1998)013<0286:AEHDAF>2.0.CO;2.

Wright, C. J., J. A. Thornton, L. Jaeglé, Y. Cao, Y. Zhu, J. Liu, R. Jones Ii, R. Holzworth, D. Rosenfeld, R. Wood, P. Blossey, and D. Kim (2025). "Lightning declines over shipping lanes following regulation of fuel sulfur emissions". *Atmospheric Chemistry and Physics* 25.5, 2937–2946. DOI: 10.5194/acp-25-2937-2025.

A. Appendix

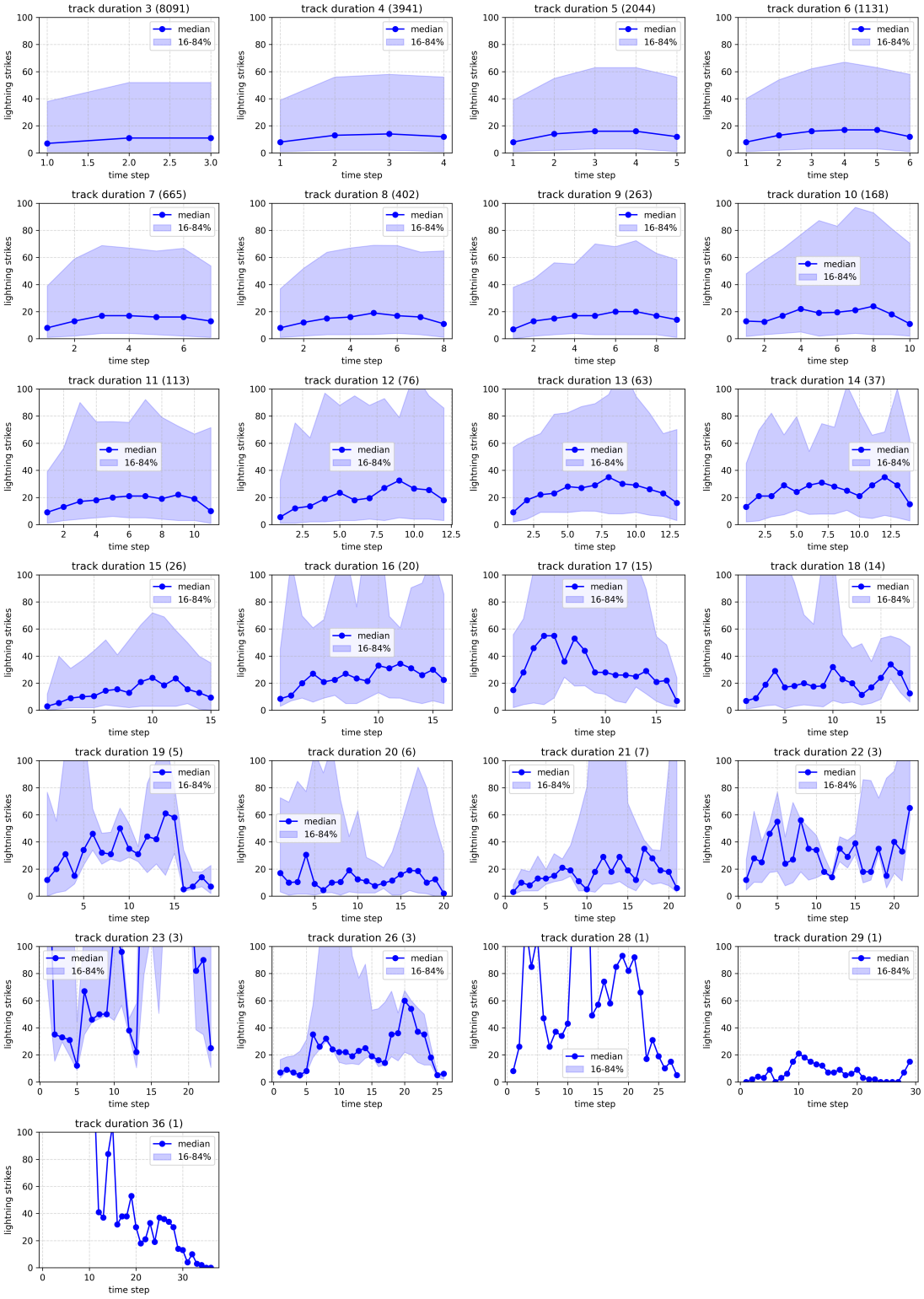

Figure A.1: Average number of lightning strikes per time step along radar-detected hail tracks of different lifetimes. The solid lines indicate the mean number of lightning strikes per time step, while the shaded areas represent the 16th-84th percentile range across all tracks within each group. Numbers in parentheses denote the total number of hail tracks within each group.

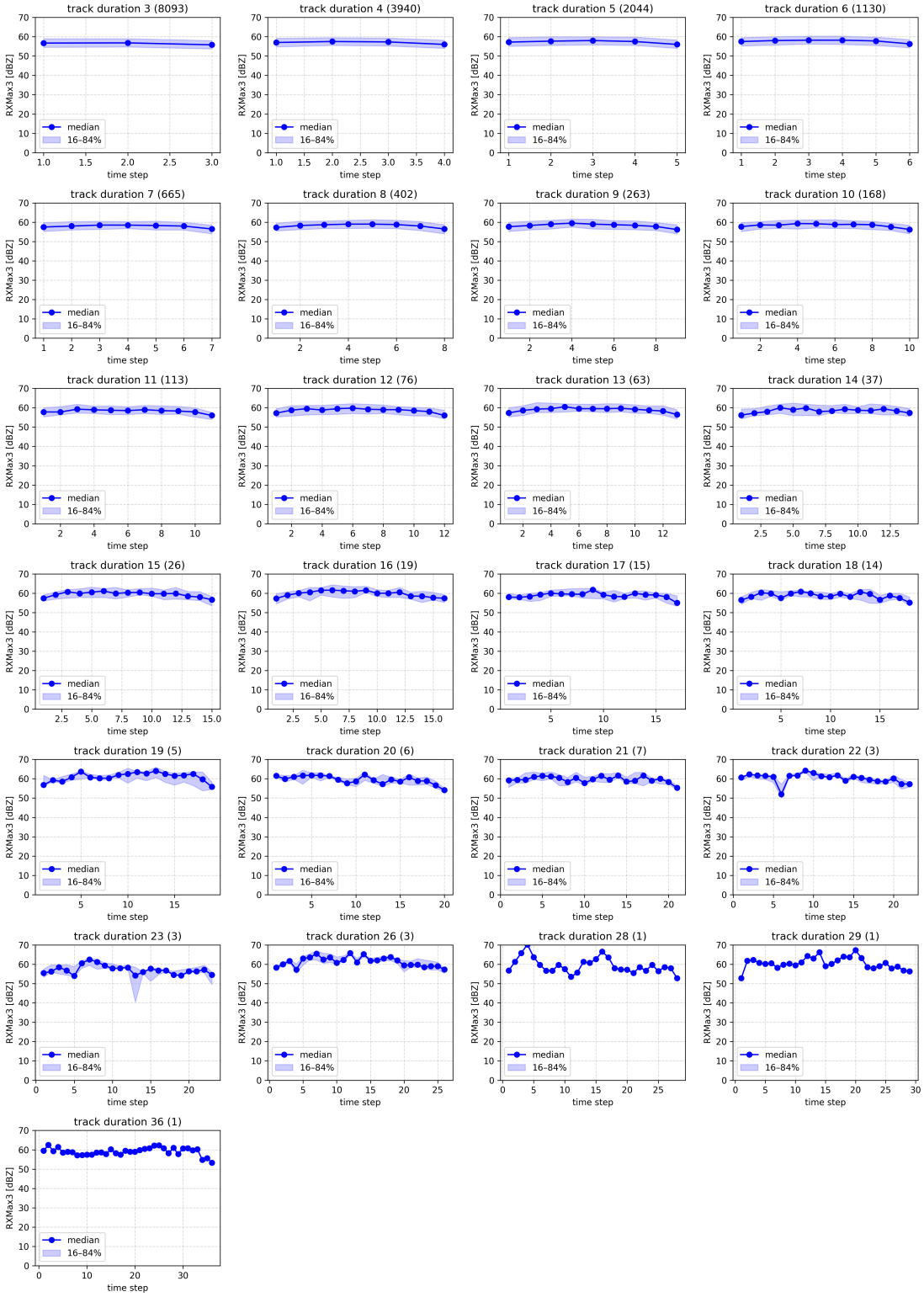

Figure A.2: Average amount of $RXMax3$ per time step along radar-detected reflectivity cores (RCs) of different lifetimes. The solid lines indicate the mean of $RXMax3$ per time step, while the shaded areas represent the 16th-84th percentile range across all tracks within each group. Numbers in parentheses denote the total number of hail tracks within each group.

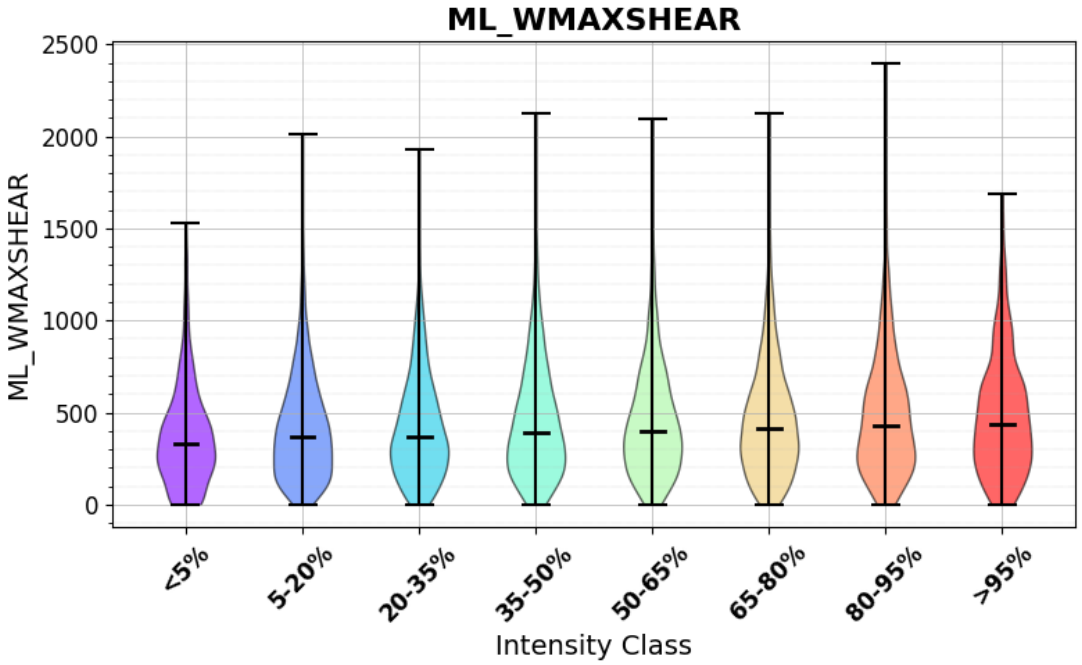

(a) combination of maximum vertical velocity and wind shear for mixed-layer air parcel in [$m^2\ s^{-2}$]

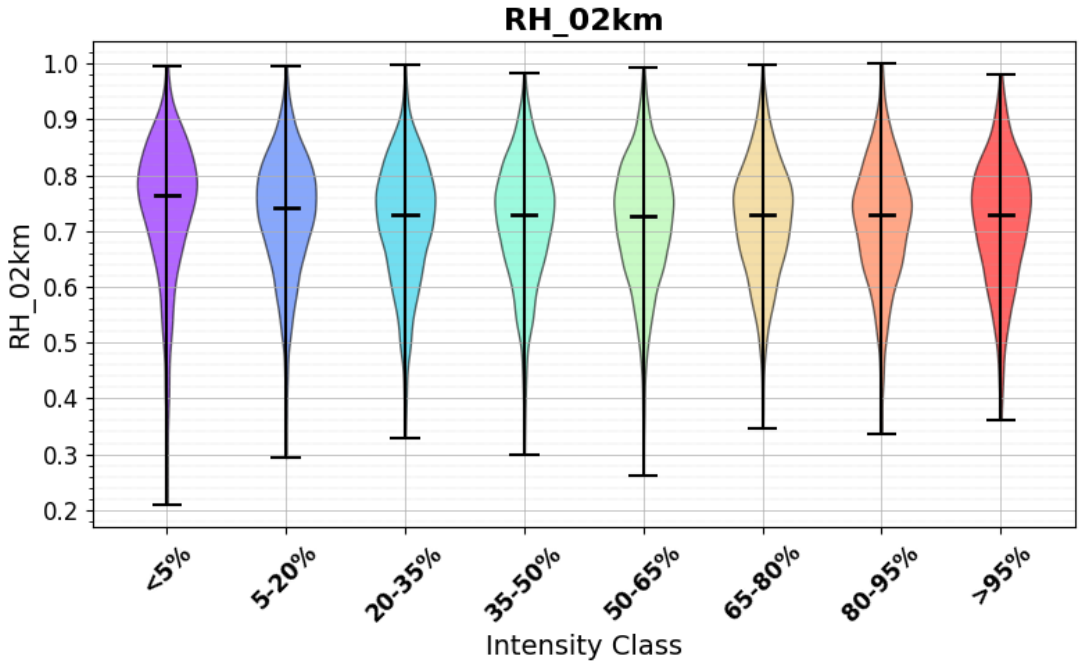

(b) relative humidity between 2 and 5 km in [ ]

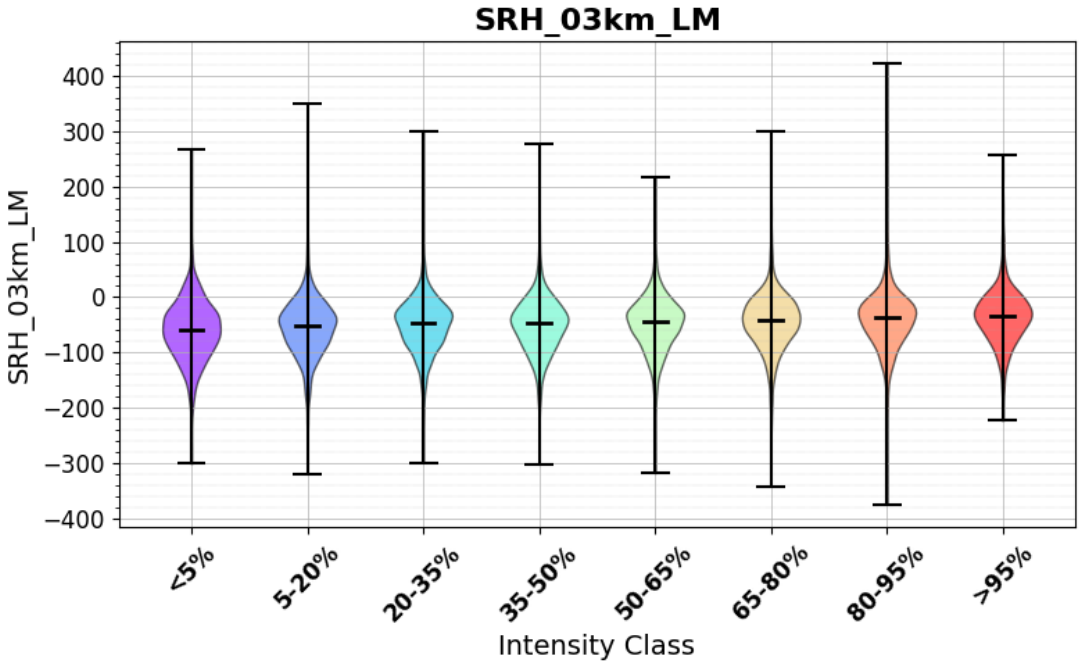

(c) storm-relative helicity between 0 and 3 km for left mover cells in [$m^2\,s^{-2}$]

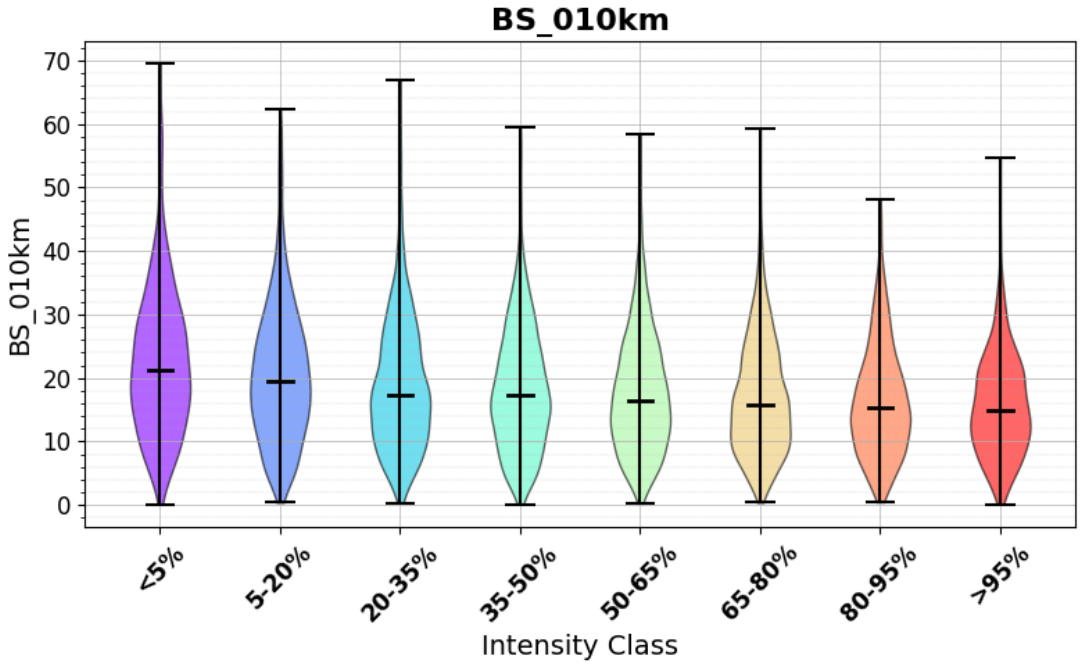

(d) bulk shear between 0 and 10 km in [$m\,s^{-1}$]

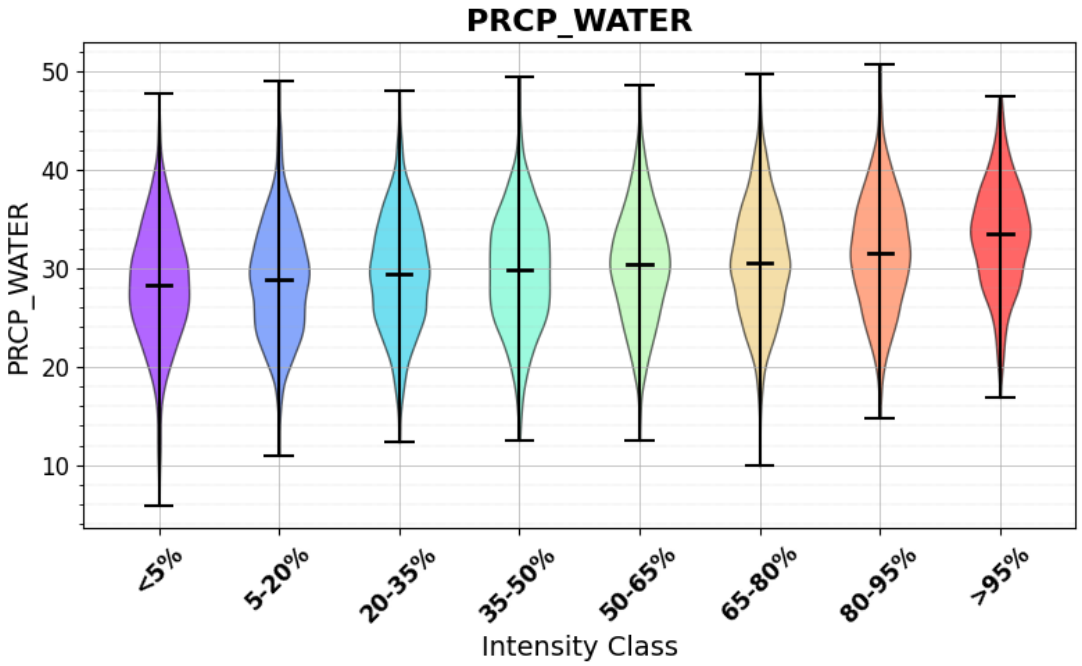

(e) precipitable water in [mm]

Figure A.3: Distribution of selected convective parameters by average lightning activity. Tracks are grouped into lightning intensity categories based on their average number of lightning strikes per track. The colors of the violins indicate the percentile groups, which are applied consistently throughout the analysis. Statistical tests confirm that the light-blue and orange percentile groups differ significantly.

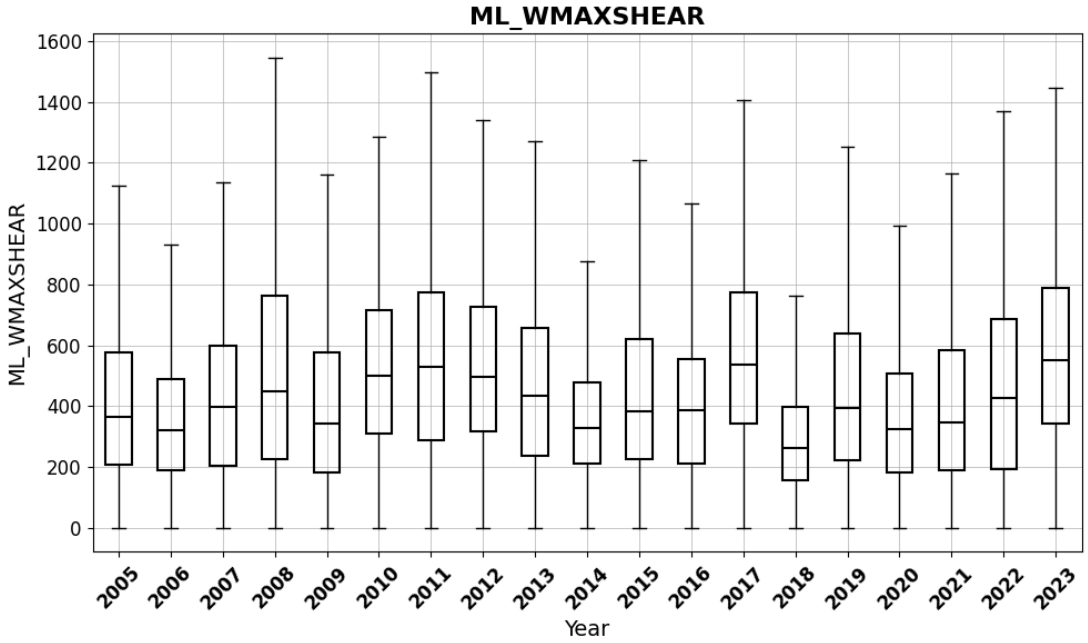

(a) combination of maximum vertical velocity and wind shear for mixed-layer air parcel in [$m^2\ s^{-2}$]

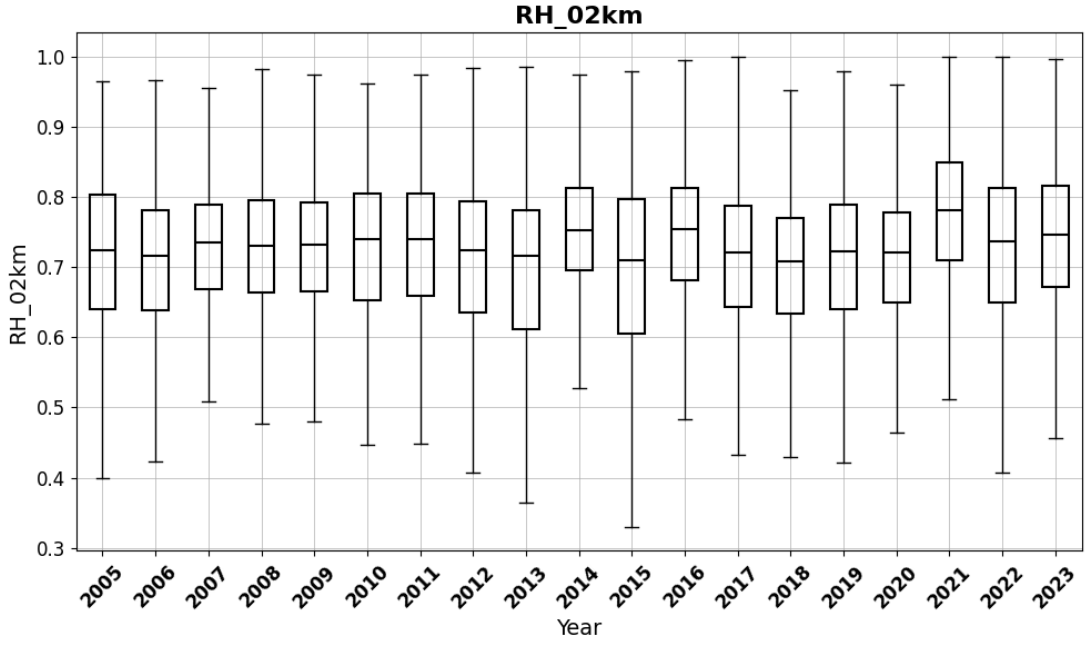

(b) relative humidity between 2 and 5 km in [ ]

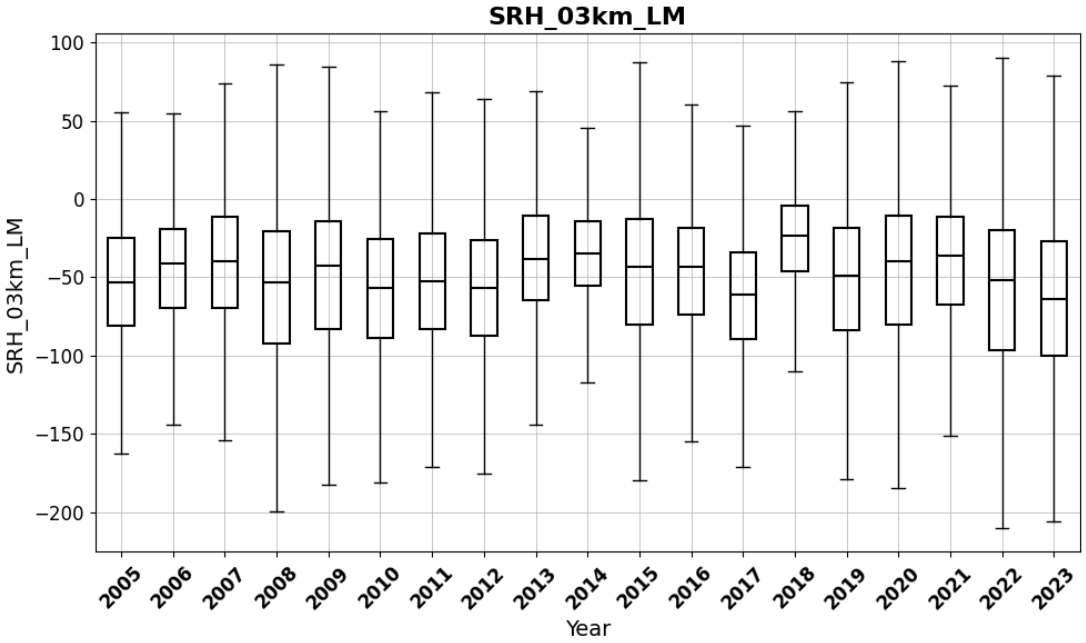

(c) storm-relative helicity between 0 and 3 km for left mover cells in $[m^2\ s^{-2}]$

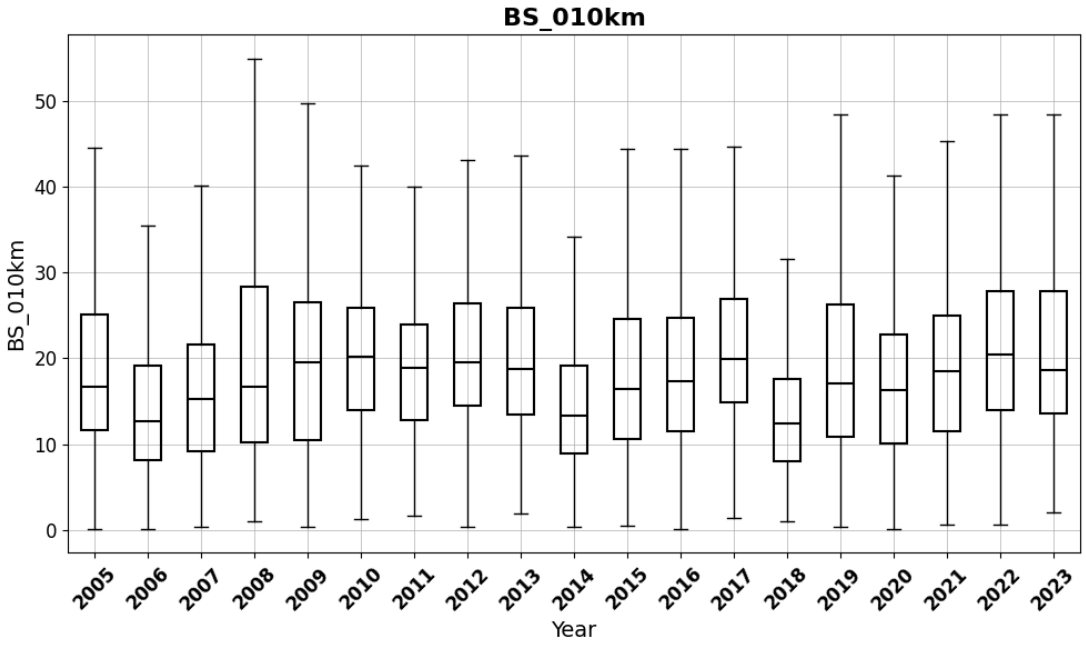

(d) bulk shear between 0 and 10 km in $[m\ s^{-1}]$

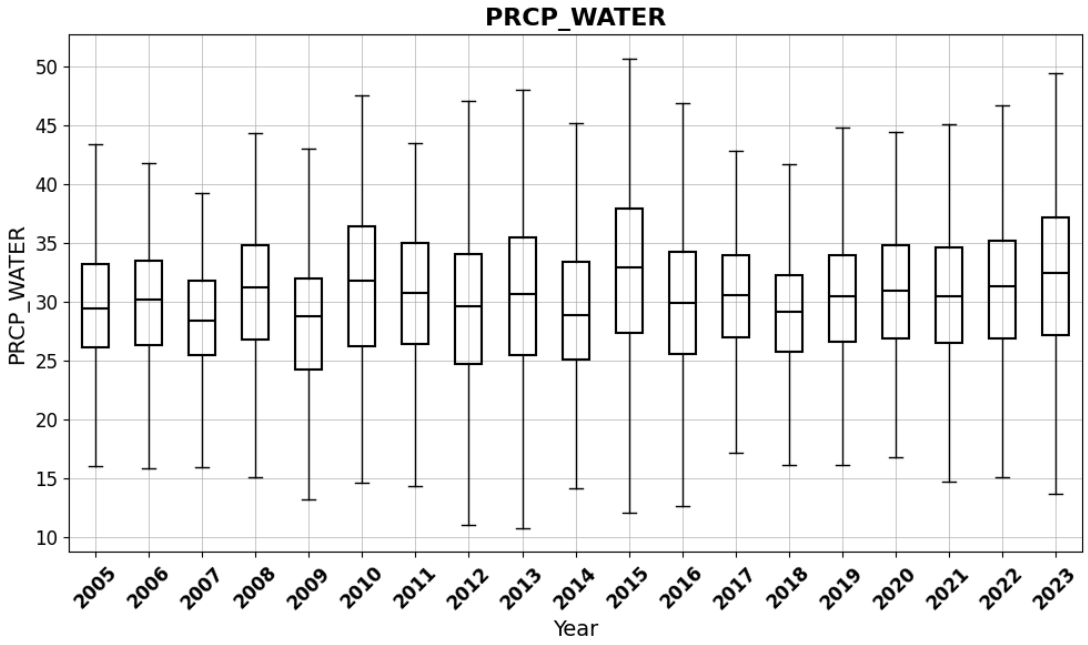

(e) precipitable water in [mm]

Figure A.4: Annual distribution of selected convective parameters.

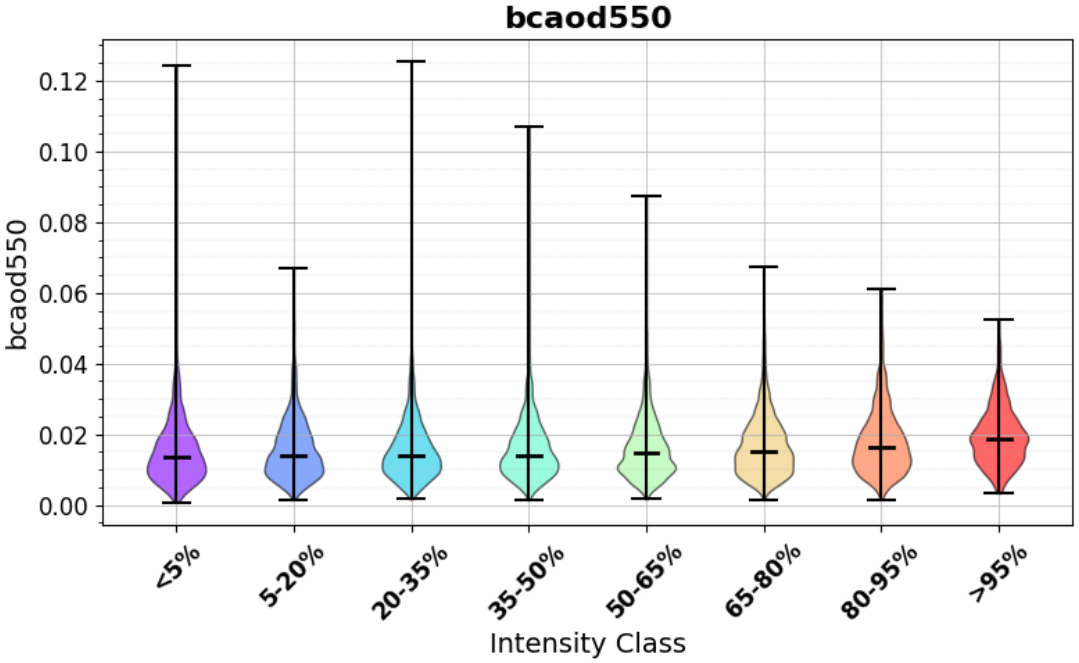

(a) black carbon aerosol optical depth at 550 nm in [ ]

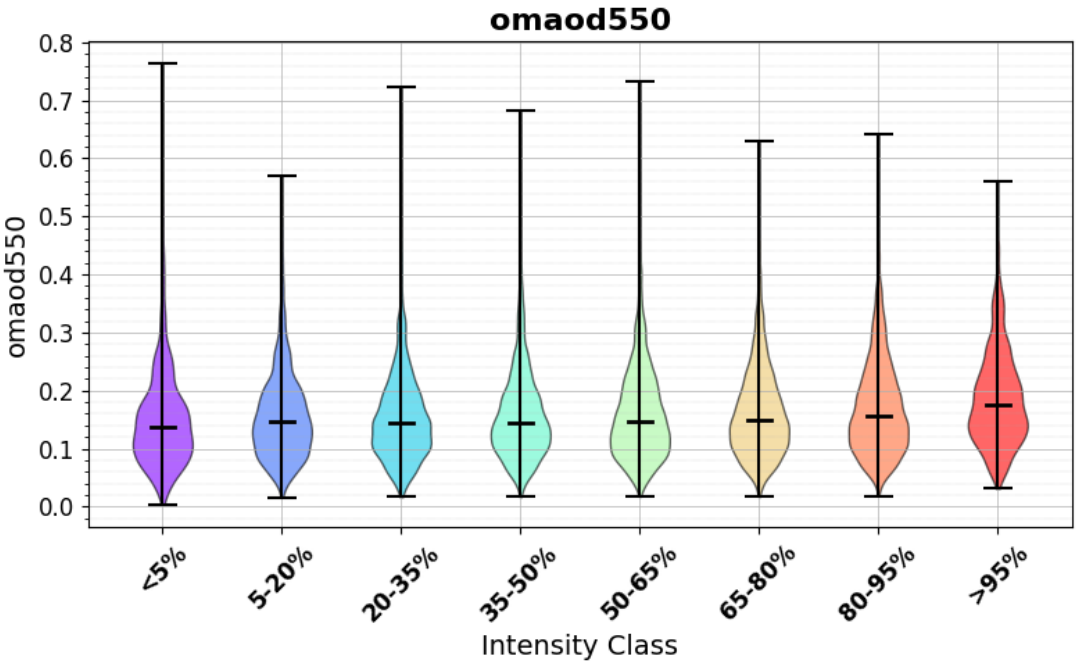

(b) organic matter aerosol optical depth at 550 nm in [ ]

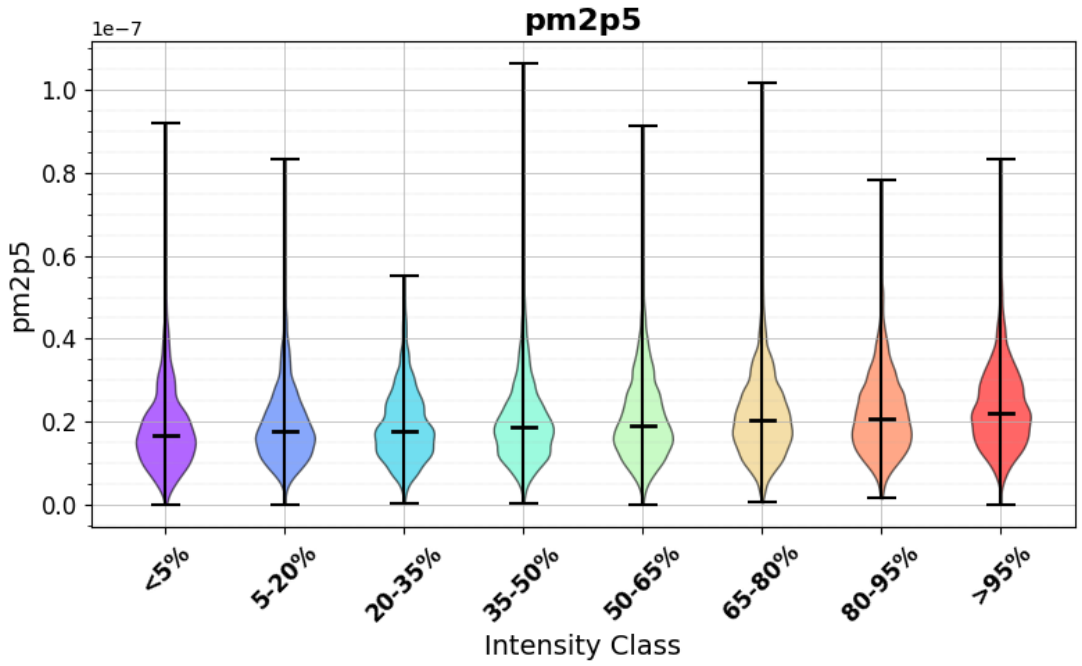

(c) particulate matter with diameter < 2.5 µm in [kg m^{-3}]

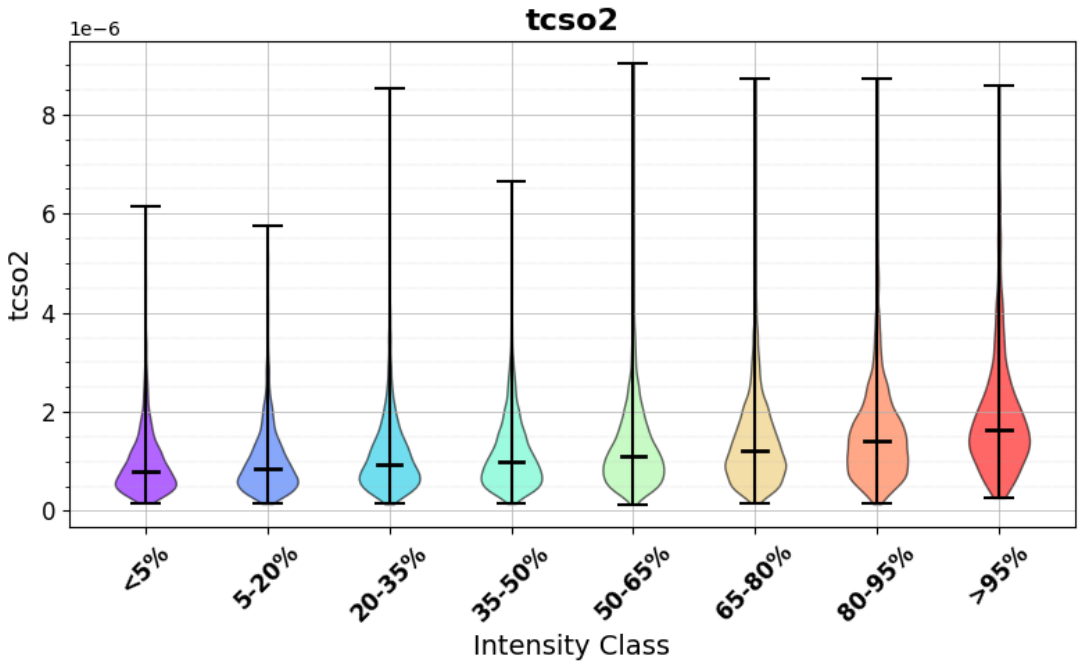

(d) total column sulfur dioxide in kg m^{-2}

Figure A.5: Distribution of selected atmospheric aerosol parameters by average lightning activity. Tracks are grouped into lightning intensity categories based on their average number of lightning strikes per track. The colors of the violins indicate the percentile groups, which are applied consistently throughout the analysis. Statistical tests confirm that the light-blue and orange percentile groups differ significantly.

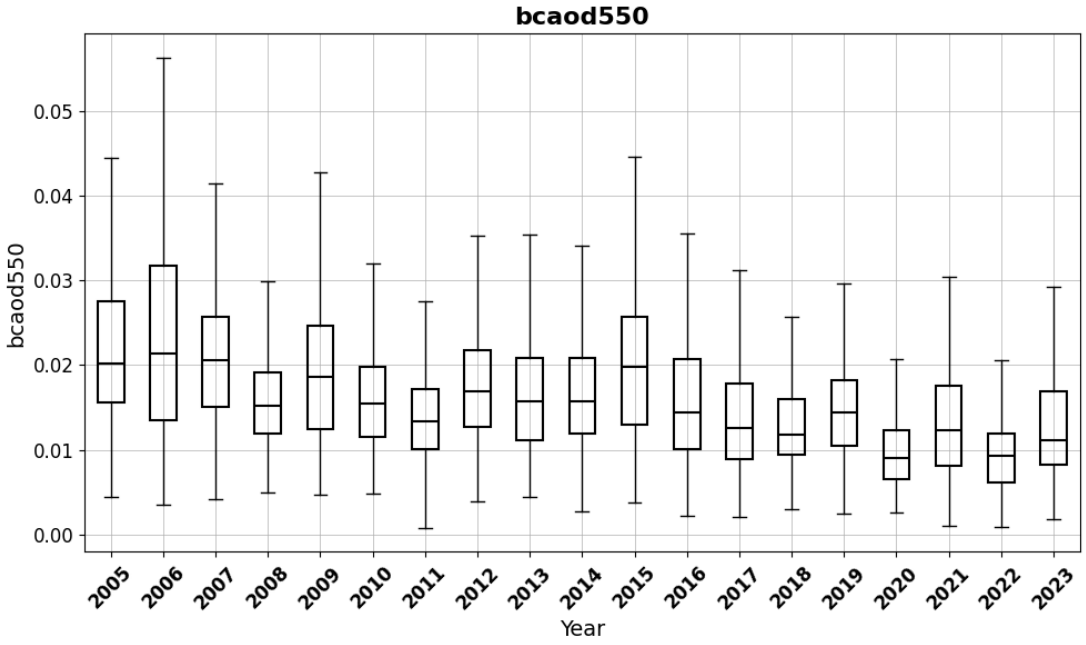

(a) black carbon aerosol optical depth at 550 nm in [ ]

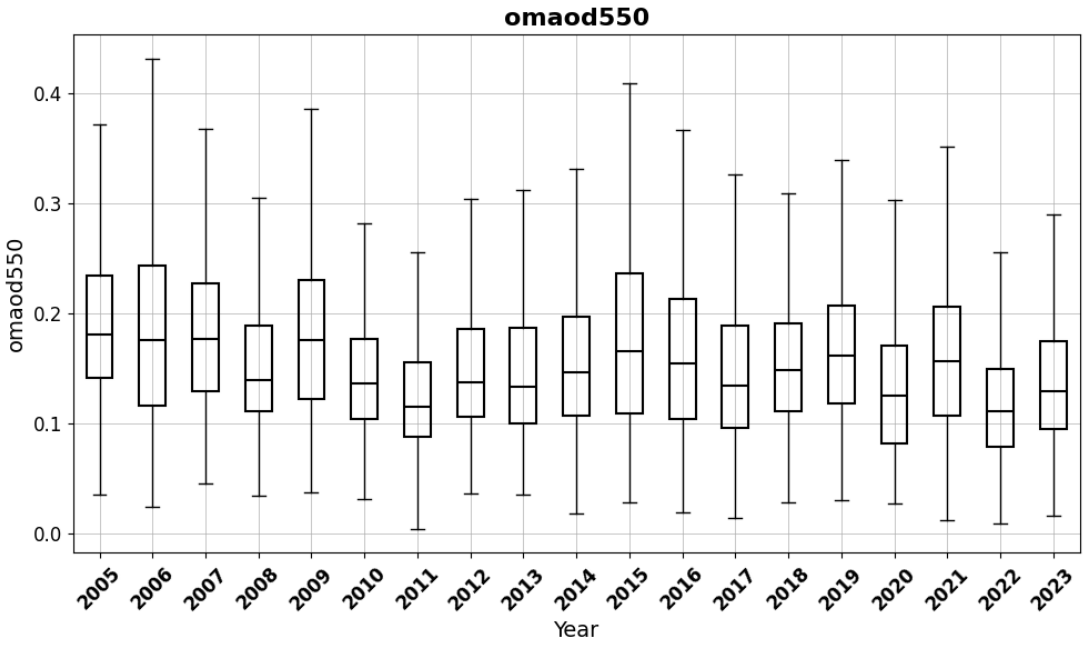

(b) organic matter aerosol optical depth at 550 nm in [ ]

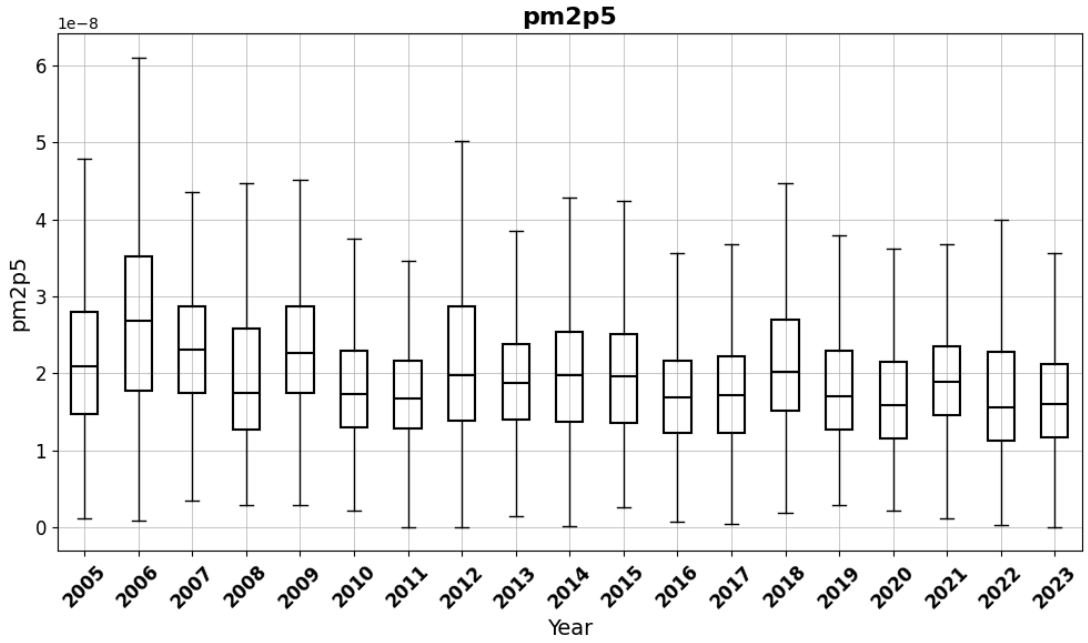

(c) particulate matter with diameter < 2.5 µm in [kg m^{-3}]

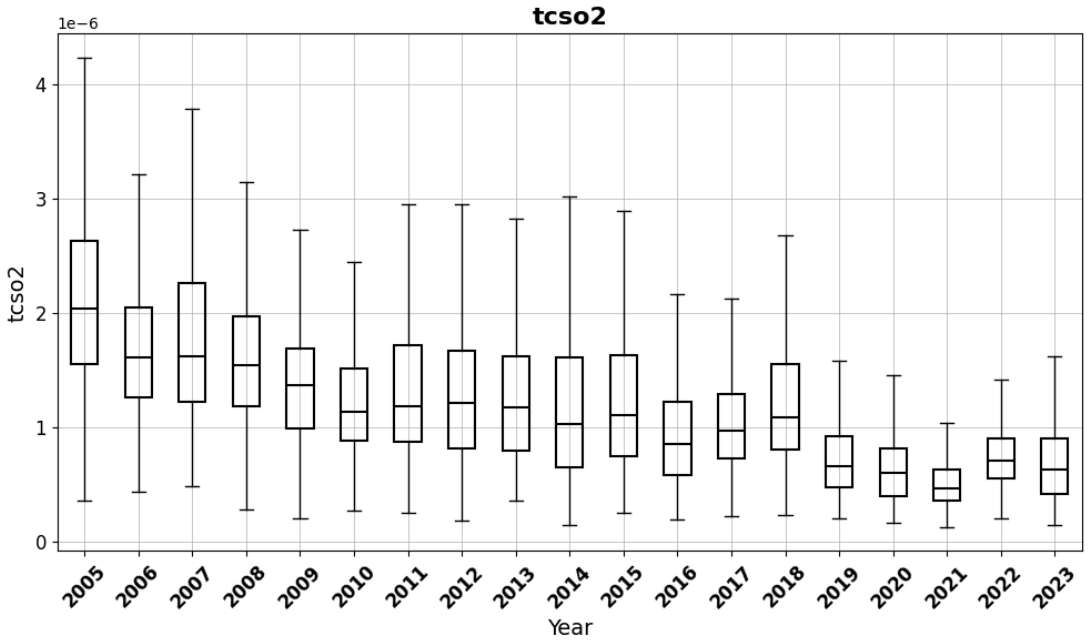

(d) total column sulfur dioxide in kg m^{-2}

Figure A.6: Annual distribution of selected atmospheric aerosol parameters.

Acknowledgements

First of all, I would like to thank Jannick Fischer von zur Gathen, for your support throughout the entire year, the helpful discussions and meetings, and for your contribution to the overall improvement of my work.

Also thanks to Markus Augenstein, for your insightful guidance, practical tips, and encouraging words.

Special thanks go to Michael Kunz for your valuable input and constructive feedback throughout the year.

I also want to thank Andreas Fink for your valuable feedback on the presentation and for your role as co-supervisor.

I would like to extend my special thanks to the entire working group for the warm welcome, the valuable discussions, and the feedback on the presentations and drafts of the thesis.

I am also deeply thankful to my closest ones for your constant love and support. Without you, I would not have reached this point.

Last but not least, a short note to my younger self: We made it! Keep going, keep pushing, and let them!

Lightning characteristics along radar-detected hail tracks (Master's Thesis)

I declare that I have developed and written the enclosed thesis completely by myself. I have not used any other than the aids that I have mentioned. I have marked all parts of the thesis that I have included from referenced literature, either in their original wording or paraphrasing their contents. I have followed the by-laws to implement scientific integrity at KIT.

Karlsruhe, 17. December 2025

. . . . . .

(Marie Lange)